Springer Tracts in Mechanical Engineering

Patrizia Trovalusci *Editor*

Materials with Internal Structure

Multiscale and Multifield Modeling and Simulation

Springer

Springer Tracts in Mechanical Engineering

About this Series

Springer Tracts in Mechanical Engineering (STME) publishes the latest developments in Mechanical Engineering - quickly, informally and with high quality. The intent is to cover all the main branches of mechanical engineering, both theoretical and applied, including:

- Engineering Design
- Machinery and Machine Elements
- Mechanical structures and stress analysis
- Automotive Engineering
- Engine Technology
- Aerospace Technology and Astronautics
- Nanotechnology and Microengineering
- Control, Robotics, Mechatronics
- MEMS
- Theoretical and Applied Mechanics
- Dynamical Systems, Control
- Fluids mechanics
- Engineering Thermodynamics, Heat and Mass Transfer
- Manufacturing
- Precision engineering, Instrumentation, Measurement
- Materials Engineering
- Tribology and surface technology

Within the scopes of the series are monographs, professional books or graduate textbooks, edited volumes as well as outstanding PhD theses and books purposely devoted to support education in mechanical engineering at graduate and post-graduate levels.

More information about this series at http://www.springer.com/series/11693

Patrizia Trovalusci
Editor

Materials with Internal Structure

Multiscale and Multifield Modeling and Simulation

Springer

Editor
Patrizia Trovalusci
Department of Structural and Geotechnical Engineering
Sapienza University of Rome
Rome, Italy

ISSN 2195-9862 ISSN 2195-9870 (electronic)
Springer Tracts in Mechanical Engineering
ISBN 978-3-319-21493-1 ISBN 978-3-319-21494-8 (eBook)
DOI 10.1007/978-3-319-21494-8

Library of Congress Control Number: 2015953503

Springer Cham Heidelberg New York Dordrecht London

Printed on acid-free paper

Springer International Publishing AG Switzerland is part of Springer Science+Business Media (www.springer.com)

Preface

A material can be defined as complex because of the presence of heterogeneous and discontinuous internal structure, which can be detected at different (meso, micro/nano, atomic, electronic) length scales, and because of its non-linear constitutive behaviours, such as plasticity, damage, fracture, growth. Based on their internal structure the materials can be classified as particulate or fibre–reinforced composites, polycrystals with interfaces, materials with voids or defects, etc.

The possibility of designing and/or testing materials with internal structure, addressing the wider technological applications in engineering, is closely related to the ability of deriving their constitutive relationships taking into account the internal structure: shape, spatial distribution, orientation and size of the constituents, which may presents several orders of magnitude starting from the submicron scale up to larger meso and macro scales. A basic issue of the mechanics of such structured materials, from modern nanoscience to structural engineering, is then to deduce properties and relations at a given macro-scale by bridging information at proper underlying micro-levels using multiscale approaches, balancing accuracy of the description with computational burden.

This volume presents a series of papers by expert researchers specialized in various fields of continuum and computational mechanics, as well as material science. The focus is on principles and strategies for multiscale modelling and simulation of complex heterogeneous materials, with periodic or random microstructure, subjected to various types of mechanical, thermal, chemical loadings and environmental effects. A wide overview of complex behaviour of materials is provided.

Among the various approaches, attention is particularly addressed to non–local field descriptions, which are characterized by the presence of internal lengths and spatial dispersion in wave propagations. These descriptions allow us to circumvent physical inadequacies and the well known theoretical/computational problems of the classical local models, related to the ill–posedness of field equations and the consequent loss of objectivity of the numerical solutions as dependent on the discretization. In such a framework, various kinds of advanced continuum models are presented which, provided by constitutive characterization for the internal and external actions, constitute a very powerful frame for the gross mechanical

description of complex material behaviours, without the restrictions of classical coarse–graining multiscale approaches.

Entering in some details, the chapters deals with:

- homogenization methods aimed at deducing the overall properties of polycristalline aggregates in the elastic–plastic and elastic–visco–plastic regime;
- phase–field approaches proposed to describe both brittle and cohesive fracture phenomena;
- effective material properties of nanostructures material derived accounting for surface/interface properties;
- simulation the fatigue crack nucleation process in polycrystals through effective microstructural parameters for plastic flow;
- development of second order homogenization methods, including second gradient and gradient Cosserat, for granular material descriptions basing on generalized macrohomogeneity conditions of Hill's type;
- stochastic continuum thermomechanics involving tensor random fields for the representation of spatially varying material properties;
- design of composite materials basing on structural stochasticity with reference to elastic–plastic and damping behaviour;
- guidelines for deriving scale–dependent continuum formulations starting from discrete material descriptions and basing on the virtual power equivalence.

Several recent books are published on a similar topic, which is of central interest in the community of material science and structural engineering. This volume in particular will be an opportunity, offered by researchers active in different fields (continuum mechanics, computational mechanics, experimental mechanics), to provide a forum for the presentation of fundamental, theoretical, experimental and practical aspects of mechanical modelling of materials with complex microstructures and complex behaviour oriented at bridging the gap between mechanical engineering and material science. The book is addressed to an advanced, but not strictly specialized, audience stimulating a general understanding of interactions among different approaches and conceptions. This should be useful for having a general overview of the matter which can inspire new research directions.

Acknowledgements

The editor would like to thank Dr. Antonino Favata for help in checking and assembling the text.

Rome, Italy Patrizia Trovalusci

Contents

Scale Transition Rules Applied to Crystal Plasticity

Georges Cailletaud and Florent Coudon

Abstract Homogenization methods adapted to polycrystalline aggregates are discussed. The description of the transition rule using the self-consistent scheme and based on the assumption of time-independent plasticity are first detailed. A few alternative propositions that simplify the general rate form of the relation given by Hill are also presented, with their limitations. A second part recalls several key ideas used to transfer the problem to time-dependent behavior. A final part is devoted to the comparison of several mean-field models and CPFEM simulations in the case of an equiaxed polycrystalline aggregate with an uniform or heterogeneous local elastic behavior. A significant effect of non-uniform elastic properties is exhibited on the macroscopic behavior, specifically on the apparent yield stress, and also on stress and strain fields.

1 Introduction

In this chapter, polycrystals relate to aggregates, natural or man-made, composed of randomly oriented and distributed grains, seen as single crystals. Depending on microstructure characteristics, different strategies are developed to deduce the overall mechanical behavior of these materials. (1) If no local information is available at the grain scale, Level 1's strategy consists in using a thermodynamical framework to derive evolution rules of a series of state variables that will represent the behavior of the material element, considered as a "black box." The local phenomena are averaged, and the material parameters have to be calibrated from macroscopic experimental tests. As a consequence, the domain of validity of the macroscopic models is usually restricted to the loading zone used for the calibration. (2) The opposite solution consists in an explicit representation of the 3D geometry of the aggregates. This can be made either by taking experimental geometries, or by generating synthetic aggregates using tessellation algorithms. In this so-called Level 3 approach, the constitutive equations are then solved at the grain scale, for

G. Cailletaud (✉) • F. Coudon
Centre des Matériaux, Mines ParisTech, 10 rue Henri Desbruères, 91003 Evry, France
e-mail: georges.cailletaud@mines-paristech.fr; florent.coudon@mines-paristech.fr

P. Trovalusci (ed.), *Materials with Internal Structure*, Springer Tracts in Mechanical Engineering, DOI 10.1007/978-3-319-21494-8_1

instance by finite element method (FEM). Each Gauss point is assigned a crystal plasticity (CP) behavior and a given crystallographic orientation. The purpose of such an approach is to capture the heterogeneities of the local stress and strain fields, and to have an access to local mechanisms responsible for deformation and damage development. The weakness of the method is that the characterization of the real 3D microstructure is a very difficult task, and that crystal plasticity finite element method (CPFEM) is time-consuming. (3) This is why the present chapter deals with an intermediate level of modelling (Level 2) where the stress equilibrium is solved at the macroscopical scale and the constitutive equations are expressed at the grain scale. Homogenization methods adapted to polycrystalline aggregates are now well studied, specifically using the self-consistent scheme proposed by Kröner [18], and Hill [15]. The approach considers "grains" as inclusions embedded in a HEM, the properties of which are searched as a weighted average of each grain contribution. For linear elastic behavior, the inclusion problem was solved by Eshelby [13]. For ellipsoidal shapes, the problem can be solved by introducing an analytical expression of the "stress-free" strain coming from the heterogeneity, which is uniform within the inclusion. A long-standing problem was the extension of this method to elastoplasticity, particularly due to the nonlinear form of constitutive equations. The question comes to the definition of interactions between grains: How the plastic accommodation and even more the viscoplastic accommodation could be introduced in models to obtain a realistic response? To solve the problem, a first step consists in approximating the local mechanical behavior of each phase by a linear relation between local stress and strain. The solution is then obtained by applying the self-consistent (SC) approach to build the effective tensors. Most of the recent homogenization theories have been developed for composite materials, where only two phases (matrix and fibers) come into play. In such a case, the Mori–Tanaka scheme [30], defines fibers/particles as inclusions embedded in the matrix, with predefined properties. In theory, the development of mean-field theories could be applied for both Mori–Tanaka and SC schemes, changing the definition of local tensors to crystal plasticity. In practice, the presence of numerous phases within polycrystalline aggregates may be a first drag to implement complex interaction theories used for composite materials: CPU times would be widely increased. Otherwise, the heterogeneous elastic response, varying locally with respect to crystallographic orientations, appears to have a significant impact on the effective yield stress and local scattered EVP responses [40]. The purpose of this paper is to briefly summarize the main theories in the field of homogenization methods and to highlight first and second order effects on the local level. After this introduction, the next part is devoted to time-independent plastic behavior, and the last one to the elasto-viscoplastic case.

2 Time-Independent Elastic–Plastic Behavior

In the landmark contributions due to Budiansky and Wu [5] and Kröner [18], a first approach of the polycrystal behavior (called the KBW model in this paper) assumes that the HEM is linear elastic, so that the Eshelby solution can be directly applied. The solution of the inclusion problem that is initially used for non-uniform elasticity can be extended to elastoplasticity by considering plastic strain as an initial "eigenstrain" that will produce intergranular residual stresses. In the case of isotropic materials, the local stress $\underset{\sim}{\boldsymbol{\sigma}}^{\mathrm{g}}$ of the grain g is then expressed as:

$$\underset{\sim}{\boldsymbol{\sigma}}^{\mathrm{g}} = \underset{\sim}{\boldsymbol{\Sigma}} + 2\mu(1-\beta)(\underset{\sim}{\boldsymbol{E}}^{p} - \underset{\sim}{\boldsymbol{\varepsilon}}^{\mathrm{g}p}) \tag{1}$$

where μ is the shear modulus and β only depends on Poisson's ratio ν of the HEM. The KBW model has been widely used due to its easy implementation and the reasonable CPU time needed to solve mechanical problems, not that far from purely macroscopic models [49]. However, the model overestimates the effective stress of the polycrystal, and finally, for large deformations, it almost reaches Taylor's upper bound that originates from an assumption of uniform plastic strain [44]. The exaggerated value of the internal stresses have been explained by the presence of an elastic accommodation rule [47]. To account for both elastic and plastic accommodation of grains, Hill proposed a rate formulation, introducing a local tangent tensor $\underset{\approx}{\boldsymbol{L}}^{g}$ which links local stress and strain rates [15]:

$$\dot{\underset{\sim}{\boldsymbol{\sigma}}}^{\mathrm{g}} = \underset{\approx}{\boldsymbol{L}}^{g} : \dot{\underset{\sim}{\boldsymbol{\varepsilon}}}^{\mathrm{g}} \tag{2}$$

The linear form of the relation gives the opportunity to define an additional "stress-free" strain rate, uniform within the inclusion for ellipsoidal shapes. The effective mechanical behavior is assumed to have the same linear form as the local ones, linked by an effective tangent tensor $\underset{\approx}{\boldsymbol{L}}^{eff}$. In this context, the concentration rule is also expressed under rate form:

$$\dot{\underset{\sim}{\boldsymbol{\sigma}}}^{\mathrm{g}} = \dot{\underset{\sim}{\boldsymbol{\Sigma}}} + \underset{\approx}{\boldsymbol{L}}^{eff} : (\underset{\approx}{\boldsymbol{S}}^{-1} - \underset{\approx}{\boldsymbol{I}}) : (\dot{\underset{\sim}{\boldsymbol{E}}} - \dot{\underset{\sim}{\boldsymbol{\varepsilon}}}^{\mathrm{g}}) \tag{3}$$

where the Eshelby tensor $\underset{\approx}{\boldsymbol{S}}$ now depends on the effective elastic–plastic tangent tensor. A difficulty of the method comes from the implicit form of the approach: The expression of local stress rates uses the effective tangent tensor, which depends itself from the local tensor $\underset{\approx}{\boldsymbol{L}}^{g}$. For a given load increment, an iterative procedure has to be achieved, in order to get converged local stress rates. Note that, in the ideal case of time-independent plasticity, Schmid's law commonly used into crystal plasticity models induces multiple slip, so that the stress state goes on a vertex of the yield surface (see, e.g., [6]). It is also well known that the unicity of the solution concerning the set of active slip system has to be enforced by an additional condition

[4] or through a regularization procedure, for instance by means of a viscoplastic formulation [32] or a regularized Schmid law (RSL). This local treatment of the constitutive equations may lead to an overestimation of the effective stress for large plastic strain [46]. Otherwise, the Hill self-consistent scheme has been simplified by Berveiller and Zaoui [3] in the case of isotropic elastic–plastic local tangent tensors. The decomposition of the tensors into an hydrostatic and a deviatoric part and the assumption of a zero trace of the local and overall plastic strains simplify the Hill concentration equation:

$$\dot{\underset{\sim}{\sigma}}^{\mathrm{g}} = \dot{\underset{\sim}{\Sigma}} + (1-\beta)\frac{2\mu\mu^L}{\mu\beta + \mu^L(1-\beta)}(\dot{\underset{\sim}{E}}^p - \dot{\underset{\sim}{\varepsilon}}^{\mathrm{gp}}) \tag{4}$$

where μ^L represents the elastic–plastic shear modulus of the HEM. The expression can be integrated, so that the scale transition rule has an explicit formulation, so-called the secant self-consistent approach:

$$\begin{gathered}\underset{\sim}{\sigma}^{\mathrm{g}} = \underset{\sim}{\Sigma} + 2\mu\alpha(1-\beta)(\underset{\sim}{E}^p - \underset{\sim}{\varepsilon}^{\mathrm{g}p}) \\ \alpha = \frac{15(1-\nu)\mu^*(7-5\nu^*)}{(7-5\nu)(2\mu(4-5\nu^*)+\mu^*(7-5\nu^*))}\end{gathered} \tag{5}$$

where μ^*, ν^* are respectively the secant elastoplastic shear modulus and Poisson's ratio. For monotonic uniaxial loadings, the following approximation of α is commonly used:

$$\frac{1}{\alpha} = 1 + \frac{3}{2}\mu\frac{||\underset{\sim}{E}^p||}{J(\underset{\sim}{\Sigma})} \tag{6}$$

where $||\underset{\sim}{E}^p||$ is the equivalent cumulated plastic strain and $J(\underset{\sim}{\Sigma})$ represents the overall von Mises equivalent stress. The model ends with a concentration relation close to KBWs but, in practice, the value of α quickly decreases from unity to a few percent during plastic flow. The secant approach was recently used and modified to simulate the mechanical behavior of refractory mortarless masonry [36]. However, the domain of applications is restricted due to the assumptions on material (isotropic) and loadings (monotonic unidirectional). To extend the secant procedure to cyclic loads, the model must be able to discriminate between loading and unloading regimes, and to have a memory of the recent strain path. A pragmatic solution consists in describing nonlinear plastic accommodation by means of intergranular "kinematic like" variables, as proposed by the so-called "β -model" [7]. In this approach, KBW's form is recovered, but the shear modulus dependent term acts on a saturating variable set, $\underset{\sim}{\boldsymbol{\beta}}$ and $\underset{\sim}{\boldsymbol{\beta}}^g$, instead of global and local plastic strains [8]:

$$\underset{\sim}{\sigma}^{\mathrm{g}} = \underset{\sim}{\Sigma} + 2\mu(1-\beta)(\underset{\sim}{\boldsymbol{\beta}} - \underset{\sim}{\boldsymbol{\beta}}^g) \tag{7}$$

The set of internal variables at the grain scale β^g involves parameters directly linked to the mechanical behavior of grains and the geometry of phases. They can be seen as "scale transition" parameters, and can be calibrated by means of FECP simulations in order to fulfill the self-consistency condition. The global plastic accommodation variable β is calculated according to:

$$\underset{\sim}{\boldsymbol{\beta}} = \sum_g f^g \underset{\sim}{\boldsymbol{\beta}}^{\boldsymbol{g}} = \langle \underset{\sim}{\boldsymbol{\beta}}^g \rangle \tag{8}$$

The model can be seen as a phenomenological self-consistent model, where the scale transition variables offer a large choice to define inter-phase plastic contributions, introducing various terms observed for a given materials [9]. In particular, a first extension of the initial model to an anisotropic inelastic behavior has been proposed in [39], which generalizes the scale transition rule to:

$$\underset{\sim}{\boldsymbol{\sigma}}^{\mathrm{g}} = \underset{\sim}{\boldsymbol{\Sigma}} + \underset{\approx}{\boldsymbol{C}}^{\boldsymbol{eff}} : (\underset{\approx}{\boldsymbol{I}} - \underset{\approx}{\boldsymbol{S}}) : (\underset{\sim}{\boldsymbol{\beta}} - \underset{\sim}{\boldsymbol{\beta}}^g) \tag{9}$$

Both Eshelby's and the effective elasticity tensor are introduced into the anisotropic form of the β-rule, known a priori at the beginning of the computation. The stiffness of the mechanical response is adjusted by introducing a fourth order anisotropic tensor to track the "neighbourhood" hardening effect as, for example in [38]:

$$\dot{\underset{\sim}{\boldsymbol{\beta}}}^g = \dot{\underset{\sim}{\boldsymbol{\varepsilon}}}^{\mathrm{gp}} - \underset{\approx}{\boldsymbol{D}} : \underset{\sim}{\boldsymbol{\beta}}^g || \dot{\underset{\sim}{\boldsymbol{\varepsilon}}}^{\mathrm{gp}} || \tag{10}$$

The model was compared with a "full-field" simulation of a directionally solidified polycrystalline aggregate, using a grain distribution obtained by a Voronoï tessellation (more details in [39]). Results on the overall inelastic response show a good agreement between the two approaches for one-dimensional tensile loadings in axial and transverse directions, and for shear tests. This version of the β rule is constructed with an assumption of uniform isotropic elasticity in the aggregate, so that $\underset{\approx}{\boldsymbol{C}}^{\boldsymbol{eff}} = \underset{\approx}{\boldsymbol{C}}^{\boldsymbol{g}}$. For two-phase polymers, an extension of the β rule has been proposed in [2], in order to introduce different elastic behaviors for the matrix and particles. The same scheme can be applied to polycrystals. For that purpose, the incremental approach due to Hill is first considered in its general anisotropic form, introducing an additive decomposition of the strain rate between elastic and plastic parts. For a random distribution of grains with a cubic symmetry, the macroscopic elastic tensor is isotropic, and Eshelby's tensor as well. The resulting expression is then:

$$\dot{\underset{\sim}{\boldsymbol{\sigma}}}^{\mathrm{g}} = [\underset{\approx}{\boldsymbol{S}} + \underset{\approx}{\boldsymbol{L}}^* : \underset{\approx}{\boldsymbol{C}}^{g-1}]^{-1} : \dot{\underset{\sim}{\boldsymbol{\Sigma}}} + [\underset{\approx}{\boldsymbol{S}} + \underset{\approx}{\boldsymbol{L}}^* : \underset{\approx}{\boldsymbol{C}}^{g-1}]^{-1} : \underset{\approx}{\boldsymbol{L}}^* : (\dot{\underset{\sim}{\boldsymbol{E}}} - \dot{\underset{\sim}{\boldsymbol{\varepsilon}}}^{\mathrm{g}}) \tag{11}$$

where $\underset{\approx}{\boldsymbol{L}}^* = \underset{\approx}{\boldsymbol{L}}^{eff} : (\underset{\approx}{\boldsymbol{I}} - \underset{\approx}{\boldsymbol{S}})$ represents the elastic–plastic accommodation tensor. It is then assumed that the local elastic behavior of each phase does not depend on plastic activity of the other phases. The shape chosen for the accommodation tensor $\underset{\approx}{\boldsymbol{L}}^*$ can then be deduced from an elastic estimation, so that $\underset{\approx}{\boldsymbol{L}}^*_E = \underset{\approx}{\boldsymbol{C}}^{eff} : (\underset{\approx}{\boldsymbol{I}} - \underset{\approx}{\boldsymbol{S}})$ in the first term of Eq. (11). For the second term, the plastic contribution of $\underset{\approx}{\boldsymbol{L}}^*$ is represented by means of the internal variable β^g. Doing so, an integration of the incremental transition rule can be achieved, and an explicit form of the transition rule is retrieved:

$$\underset{\sim}{\boldsymbol{\sigma}}^{\mathrm{g}} = [\underset{\approx}{\boldsymbol{S}} + \underset{\approx}{\boldsymbol{L}}^*_E : \underset{\approx}{\boldsymbol{C}}^{\mathrm{g}-1}]^{-1} : [\underset{\sim}{\boldsymbol{\Sigma}} + \underset{\approx}{\boldsymbol{L}}^*_E : (\underset{\sim}{\boldsymbol{\beta}} - \underset{\sim}{\boldsymbol{\beta}}^g)] \tag{12}$$

Applying self-consistency provides relations for the effective elasticity tensor, the global plastic strain and accommodation variables:

$$\begin{aligned} \underset{\approx}{\boldsymbol{C}}^{eff} &= \left\langle \underset{\approx}{\boldsymbol{A}}^g_E : \underset{\approx}{\boldsymbol{C}}^g \right\rangle \\ \underset{\sim}{\dot{\boldsymbol{E}}}^p &= \left\langle \underset{\approx}{\boldsymbol{A}}^g_E : \underset{\sim}{\dot{\boldsymbol{\varepsilon}}}^{\mathrm{gp}} \right\rangle \\ \underset{\sim}{\boldsymbol{\beta}} &= \left\langle \underset{\approx}{\boldsymbol{A}}^g_E : \underset{\approx}{\boldsymbol{L}}^*_E \right\rangle \left\langle \underset{\approx}{\boldsymbol{A}}^g_E : \underset{\approx}{\boldsymbol{L}}^*_E : \underset{\sim}{\boldsymbol{\beta}}^g \right\rangle \end{aligned} \tag{13}$$

where $\underset{\approx}{\boldsymbol{A}}^g_E = [\underset{\approx}{\boldsymbol{I}} - \underset{\approx}{\boldsymbol{S}} : (\underset{\approx}{\boldsymbol{I}} - \underset{\approx}{\boldsymbol{C}}^{eff\,-1} : \underset{\approx}{\boldsymbol{C}}^g)]^{-1}$ represents the elastic localization tensor. There is still an implicit form for the effective elasticity tensor, induced by the expression of $\underset{\approx}{\boldsymbol{A}}^g$. Nevertheless, unlike the case of Hill model, it is sufficient to calculate this tensor once: At the initialization step of the model, an iterative procedure with a first value of $\underset{\approx}{\boldsymbol{C}}^{eff}$ equal to Voigt's bound is used (e.g., in [25]).

3 Homogenization Methods Applied to EVP Behavior

The time-dependent case has been initially addressed as a pure viscoplastic behavior. In this context, the first studies were made with the assumption of a "rigid viscoplastic" behavior, which consists in neglecting the (supposed small) elastic part of the total strain. The existence of a stress dissipative potential $u(\underset{\sim}{\boldsymbol{\sigma}}^{\mathrm{g}})$ is commonly assumed and the strain rate writes:

$$\underset{\sim}{\dot{\boldsymbol{\varepsilon}}}^{\mathrm{g}} = \frac{\delta u(\underset{\sim}{\boldsymbol{\sigma}}^{\mathrm{g}})}{\delta \underset{\sim}{\boldsymbol{\sigma}}^{\mathrm{g}}} \tag{14}$$

The Hill incremental procedure was extended to the study of steady creep of face centered cubic polycrystals (FCC) by Hutchinson [16], considering a power law to represent viscosity effects. The linearization procedure consists in defining secant moduli as follows:

$$\underset{\sim}{\dot{\boldsymbol{\varepsilon}}}^{\mathrm{g}} = \underset{\sim}{\dot{\boldsymbol{\varepsilon}}}^{\mathrm{gvp}} = \underset{\approx}{\boldsymbol{M}}^{g}_{sec} : \underset{\sim}{\boldsymbol{\sigma}}^{\mathrm{g}} \tag{15}$$

$$\underset{\approx}{\boldsymbol{M}}^{g}_{sec} = \frac{1}{n}\frac{\delta^2 u(\underset{\sim}{\boldsymbol{\sigma}}^{\mathrm{g}})}{\delta^2 \underset{\sim}{\boldsymbol{\sigma}}^{\mathrm{g}}} \tag{16}$$

where n is the exponent ratio of the power law and $\underset{\approx}{\boldsymbol{M}}^{g}$ is a fourth rank tensor called the "creep compliances tensor." The limitation of the model is observed when the mechanical behavior tends to time-independent behavior. The response reaches the upper bound of Hashin–Strickman [14] (more restrictive than Taylor's one). A softest model was developed by Molinari [29], introducing a Taylor decomposition of the local behavior at an applied stress $\underset{\sim}{\boldsymbol{\sigma}}^{0}$ according to:

$$\begin{aligned} \underset{\sim}{\dot{\boldsymbol{\varepsilon}}}^{\mathrm{g}} &= \underset{\approx}{\boldsymbol{M}}^{g} : \underset{\sim}{\boldsymbol{\sigma}}^{\mathrm{g}} + \underset{\sim}{\dot{\boldsymbol{\varepsilon}}}^{\mathrm{g0}} \\ \underset{\approx}{\boldsymbol{M}}^{g}_{tg} &= n\underset{\approx}{\boldsymbol{M}}^{g}_{sec} \\ \underset{\sim}{\dot{\boldsymbol{\varepsilon}}}^{\mathrm{g0}} &= g(\underset{\sim}{\boldsymbol{\sigma}}^{0}, ..) - \underset{\approx}{\boldsymbol{M}}^{g}_{tg}(\underset{\sim}{\boldsymbol{\sigma}}^{0}) : \underset{\sim}{\boldsymbol{\sigma}}^{0} \end{aligned} \tag{17}$$

where $\underset{\sim}{\dot{\boldsymbol{\varepsilon}}}^{\mathrm{g}}0$ represents a prestrain which is "stress free," such as asked to solve the inclusion problem. Applying the SC scheme, the authors supposed the same power law on the effective mechanical behavior, so that the overall moduli are "tangent" on each increment to the overall response. The tangent formulation has been implemented for finite strain by Lebensohn and Tomé [20] as the so-called VPSC method [21]. The self-consistent method applied to the homogenization of elasto-viscoplastic materials has still pending questions. The problem has been highlighted by Suquet [41], who showed that the homogenization of a set of incompressible Maxwell linear viscoelastic phases does not generally provide a Maxwell type behavior. Since that time, numerous mean-field models have been proposed to solve the elasto-viscoplastic case, but with divergent results. Indeed, a "simple" elasto-viscoplastic tangent tensor cannot be defined any more due to the simultaneous occurrence of time derivatives at different orders of stress and strain:

$$\underset{\sim}{\dot{\boldsymbol{\varepsilon}}}^{\mathrm{g}} = \underset{\approx}{\boldsymbol{S}}^{g} : \underset{\sim}{\dot{\boldsymbol{\sigma}}}^{\mathrm{g}} + g(\underset{\sim}{\boldsymbol{\sigma}}^{\mathrm{g}}, ..) \tag{18}$$

First, authors decided to keep Kröner's elastic definition of the "stress-free" strain. A first attempt was performed by Weng [45] for steady creep of polycrystalline aggregates. The approximation was justified by a physical analysis: During steady creep tests, plastic strain for a time increment depends only on stress/strain at this

time, so that the viscoplastic strain rate can be assumed as "stress-free" in the sense of Eshelby. In practice, the method consists in replacing plastic strain by viscoplastic strain in KBW's expression, written in terms of rate. Similarly, Nemat-Nasser [31] attempted to extend time-dependent behavior to the large strain formalism. As pointed out by Zaoui [26], the definition of a "stress free" strain or strain rate is not rigorously possible. Due to the nonlinear form of the equations at local scale, the inclusion problem can be solved only after a linearization stage of the local behavior. In fact, the interaction defined by Weng's model does not differ from KBW's result, which reveals an elastic type interaction. To prevent the hypothesis of a similar tangent formulation for the effective behavior, the homogenization procedure was modified in order to generate an "affine" model [27, 48]. The procedure provides intermediate results compared to the stiff secant and the soft tangent linearization responses. Otherwise, a second-order Taylor decomposition of the stress dissipative potential was introduced for polycrystalline aggregates by Liu and Ponte Castaneda [23], which allows to estimate the intraphase heterogeneity. The variational approach proposed by Ponte-Castaneda [34] is used, so that a linear comparison homogeneous media (LCHM) is defined through a first order linearization method [35] with an effective stress potential:

$$U_T(\underset{\sim}{\boldsymbol{\Sigma}}) = \frac{1}{2}\underset{\sim}{\boldsymbol{\Sigma}} : \underset{\approx}{\boldsymbol{M}}^{eff} : \underset{\sim}{\boldsymbol{\Sigma}} + \underset{\sim}{\dot{\boldsymbol{\varepsilon}}}^{g}0^{eff} : \underset{\sim}{\boldsymbol{\Sigma}} + \frac{1}{2}p \tag{19}$$

where p represents an effective energy under zero applied stress. This approach gives the opportunity to estimate per-phase average field fluctuations:

$$\langle \underset{\sim}{\boldsymbol{\sigma}} \otimes \underset{\sim}{\boldsymbol{\sigma}} \rangle^g = \frac{2}{f^g}\frac{\delta U_T(\underset{\sim}{\boldsymbol{\Sigma}})}{\delta \underset{\approx}{\boldsymbol{M}}^g} \tag{20}$$

Thus, the basic concept consists in introducing field fluctuations in the concentration relation by means of new linearization tensors [22].Now, the combination of previous homogenization methods with elastic effects is discussed. A first proposition is to consider polycrystals with an incompressible elastic behavior, having in mind that the coupling between elastic and viscoplastic contributions is taken into account [17]. The idea was extended to compressible elastic materials and multi-axial loadings [1] and applied to FCC polycrystals [10]. In parallel, other contributions proposed to build the strain field by means of two asymptotic solutions, a purely elastic and a viscoplastic one, and to introduce additional terms to deal with coupling effects [33]. Both the use of specific Kunin projectors and the definition of a "translated field" produces a new rule for strain rate localization. The method was initially proposed with a symmetric construction of elastic and plastic solutions [33]. A second version, starting from the viscoplastic solution, leads to a simpler scale transition rule [37]:

$$\underset{\sim}{\dot{\boldsymbol{\sigma}}}^{g} = \underset{\approx}{\boldsymbol{C}}^g : \underset{\approx}{\boldsymbol{A}}^g_E : \underset{\approx}{\boldsymbol{S}} : \underset{\sim}{\dot{\boldsymbol{\Sigma}}} + \underset{\approx}{\boldsymbol{C}}^g : \underset{\approx}{\boldsymbol{A}}^g_E : (\underset{\approx}{\boldsymbol{S}} - \underset{\approx}{\boldsymbol{I}}) : (\underset{\sim}{\dot{\boldsymbol{\varepsilon}}}^{\mathrm{gvp}} - \underset{\approx}{\boldsymbol{A}}^b_B : \underset{\sim}{\dot{\boldsymbol{E}}}^{vp}) \tag{21}$$

where $\underset{\approx}{\boldsymbol{A}}^{b}_{B} = [\underset{\approx}{\boldsymbol{I}} - \underset{\approx}{\boldsymbol{S}} : (\underset{\approx}{\boldsymbol{I}} - \underset{\approx}{\boldsymbol{B}}^{eff\,-1}_{sec} : \underset{\approx}{\boldsymbol{B}}^{g}_{sec})]^{-1}$ and $\underset{\approx}{\boldsymbol{B}}^{g}_{sec} = \underset{\approx}{\boldsymbol{M}}^{g\ -1}_{sec}$. The "translated field" method was recently extended using the affine linearization (instead of the secant one) for the viscoplastic solution part in [24]. For others authors, the dual occurrence of the stress at different time derivatives generates a dependence of the effective behavior to the loading path: The approach is called "hereditary". Even if the local behavior can be turned into a fictitious thermo-elastic one, the effective constitutive equations must be completed by a long memory effect [42]. A solution was proposed in [48] based on both the affine linearization of the viscoplastic strain rates and the convolution product of Stieljes, so that a thermo-elastic type equation is found:

$$\underset{\sim}{\dot{\boldsymbol{\varepsilon}}}(t) = [\underset{\approx}{\boldsymbol{s}}_{\tau} \otimes \underset{\sim}{\dot{\boldsymbol{\sigma}}}](\tau, t) + \underset{\sim}{\dot{\boldsymbol{\varepsilon}}}^{0}(\tau, t) \tag{22}$$

$$\underset{\approx}{\boldsymbol{s}}_{\tau} = \underset{\approx}{\boldsymbol{S}} + \underset{\approx}{\boldsymbol{M}}(\tau)t \tag{23}$$

where the operator $[\underset{\approx}{\boldsymbol{s}}_{\tau} \otimes \underset{\sim}{\dot{\boldsymbol{\sigma}}}](\tau, t) = \dfrac{d}{dt}[\int_0^t \underset{\approx}{\boldsymbol{s}}_{\tau}(\tau, t-u) : \underset{\sim}{\boldsymbol{\sigma}}(u)du]$ preserves from time dependency. By means of a Laplace–Carson, or z transform, a fictitious inclusion problem can be solved in the sense of Eshelby [27]. However, this approach generates complex and time-consuming calculations, particularly during the inverse transform from Laplace–Carson space to time [11]. A pure numerical approach has been proposed to avoid the dual dependence in time and space of the problem [11]. For a given (small) time increment, a linear relation between a stress increment and the total strain increment, called "incrementally affine" by authors, can be defined as:

$$\Delta\underset{\sim}{\boldsymbol{\sigma}}^{g} = \underset{\approx}{\boldsymbol{C}}^{g,alg}(t_{n+1}) : (\Delta\underset{\sim}{\boldsymbol{\varepsilon}}^{g} - \Delta\underset{\sim}{\boldsymbol{\varepsilon}}^{g,alg}) \tag{24}$$

Following this way, an inclusion problem can be solved, for each increment. To reduce the sensitivity to the time increment of both $\underset{\approx}{\boldsymbol{C}}^{g,alg}(t_n + 1)$ and $\Delta\underset{\sim}{\boldsymbol{\varepsilon}}^{g,alg}$, a regularization procedure has been introduced and tested for a two-phase polymer with J_2 elasto-viscoplasticity. The time discretization was also applied to the second order linearization method in [19, 43], coupling the dissipative potential with a free-energy function for reversible phenomena. Otherwise, the general "incrementally affine" linearization method was extended to second order estimations in [12] to account for local field fluctuations.

4 Effect of a Heterogeneous Elasticity on Both Local and Global Responses of Non-textured Polycrystalline Aggregates

This section is focused on the impact of a heterogeneous elastic behavior into the mechanical response of FCC equiaxed polycrystals. As seen before, several models assume a uniform elasticity within the polycrystalline aggregate for the sake of simplicity. However, in the case of FCC materials with a cubic local elasticity, it is well known that the elastic behavior of a given grain is directly linked to its crystallographic orientation. Although an isotropic effective elasticity tensor can be calculated which is similar in the isotropic case, the local stresses and, by consequence, the onset of the plasticity remain different. To better understand this phenomena, an equiaxed polycrystal composed of 200 grains generated by Voronoï tessellation is considered. This aggregate involves periodic relations on the geometry, mesh, and boundary conditions. At the local scale, two types of elasticity are investigated: Isotropic (IE) or cubic (CE) symmetry of the elasticity tensor. For the plastic activity of grains, a single crystal model with cubic symmetry developed by Meric and Cailletaud [28] is used with a nonlinear isotropic hardening and no kinematic hardening. The equations of the model are recalled for a given slip system s of the 12 octahedral ones:

$$\dot{\gamma}^s = \left\langle \frac{|\tau^s| - \tau^c - r^s}{K} \right\rangle^n sign(\tau^s) = \dot{v}^s sign(\tau^s) \tag{25}$$

$$r^s = Q \sum_r H^{rs}(1 - e^{-bv^r}) \tag{26}$$

$$\underset{\sim}{\dot{\boldsymbol{\varepsilon}}}^{\mathrm{gp}} = \sum_s \underset{\sim}{\boldsymbol{m}}^s \dot{\gamma}^s \tag{27}$$

where τ^s is the resolved shear stress, τ^c is the critical resolved shear stress, and $\underset{\sim}{\boldsymbol{m}}^s$ is the orientation tensor. The value of material parameters is presented in Table 1. Results are presented for a tensile test in direction 1. The macroscopical strain rate $\dot{E}_{11}$ is $10^{-4}\,\mathrm{s}^{-1}$ and the final value of E_{11} is 0.02. Six calculations using the same polycrystalline aggregate with different sets of random crystallographic orientations assigned to the 200 grains have been done. Figure 1 shows, for one of these realizations, the equivalent von Mises stress field for the two kinds of elasticity

Table 1 Value of the material parameters of the single crystal model with two forms of the elasticity tensor: isotropic and cubic

E (MPa)	ν	C_{1111} (MPa)	C_{1122} (MPa)	C_{1212} (MPa)
100,000	0.3	90,300	45,150	63,200
τ^c (MPa)	K (MPa)	n	Q	b
200	2000	4	100	10

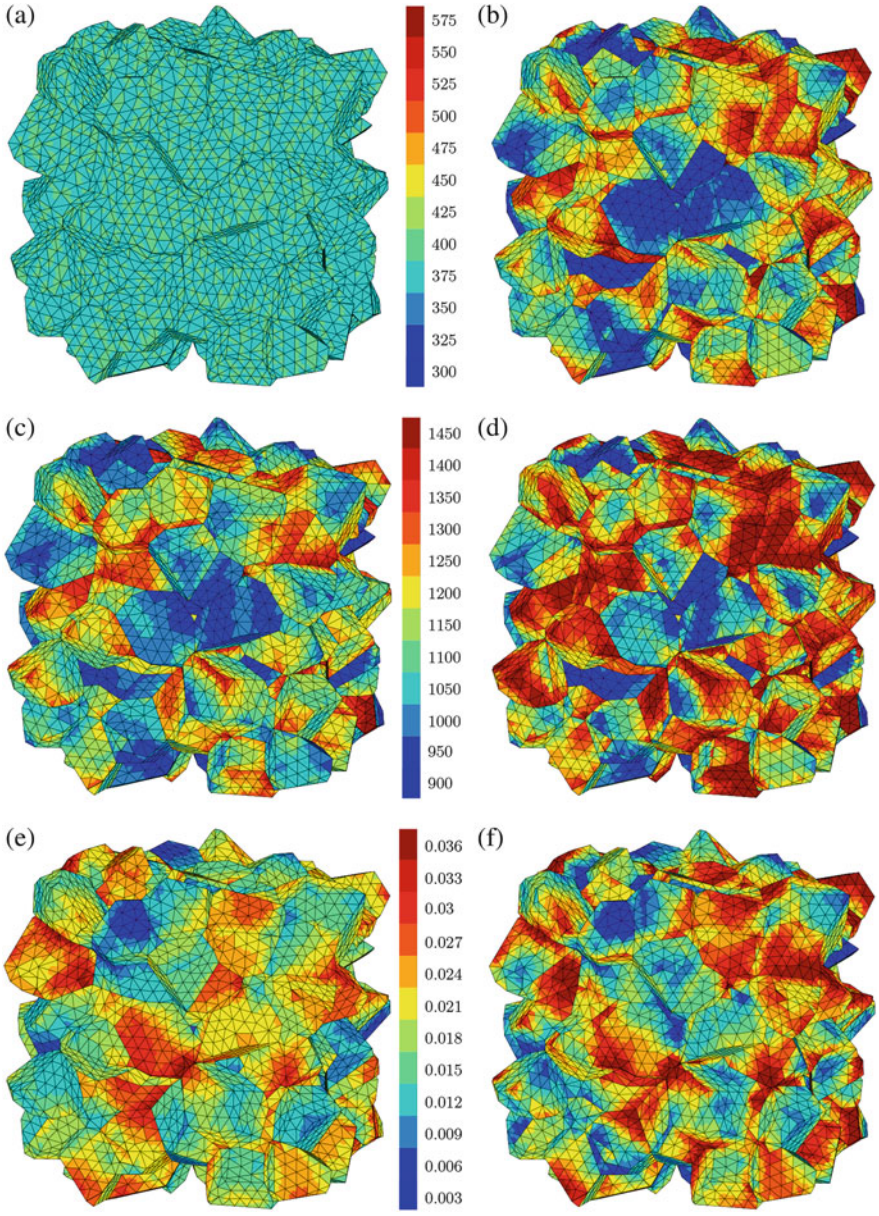

Fig. 1 Comparative results of uniform and non-uniform local elastic behavior of a 200 grain non-textured polycrystalline aggregate. (**a**, **b**) Elastic response with respectively a uniform and non-uniform elasticity (von Mises equivalent stress). (**c**, **d**) Plastic response with respectively a uniform and non-uniform elasticity (von Mises equivalent stress). (**e**, **f**) Plastic response with respectively a uniform and non-uniform elasticity (cumulated plastic strain)

tensor with no plasticity ($E_{11} = 0.004$) and at the end of the load. For the purely elastic part of the load, a uniform stress field is observed for the IE case whereas a highly scattered local stress field with more than 200 MPa is obtained in the CE case. Consequently, for the IE model, the first grain becoming plastically active is the grain with the higher Schmid factor. For the CE model, a competition between the orientation tensor and the elasticity tensor takes place, so that the plastic activity does not start necessarily within the same grain and for the same global stress than the IE case. This difference is highlighted in Fig. 2, where the macroscopical responses of both mean-field models presented before and full-field simulations are compared. Several models as Lin and Taylor model as well as Berveiller and Zaoui model or KBW model are based on the assumption of a uniform elastic behavior. This is mainly traduced by a dependence of their scale transition rule only

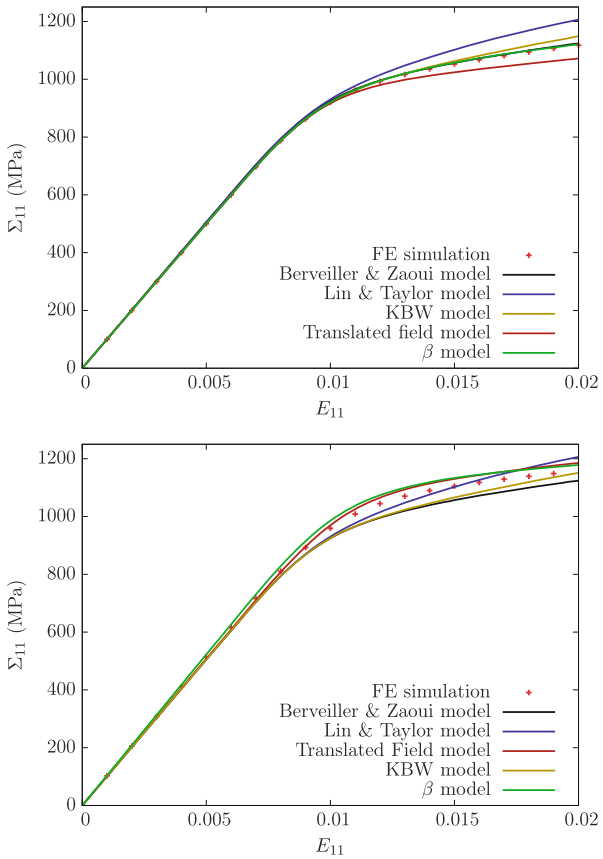

Fig. 2 Macroscopical response of a tensile test $E_{11} = 0.02$ for various mean-field models (1000 grains with random crystallographical orientations) and the average of the six FE simulations (equivalent to 1200 grains with random crystallographical orientations). *Top*: isotropic local elasticity. *Bottom*: cubic local elasticity

on the effective elastic behavior which is isotropic in both cases. For the CE case, this kind of models well known to overestimate the global stress then provides an overall stress lower than CPFEM simulations. This is directly linked to a different value of the overall yield stress, much larger for CE than IE case, while values estimated with these Level 2 models are similar. By contrast, others models, for example, the β rule or the translated field model, are developed in the general case of heterogeneous local elastic behavior. These models provide decent predictions of the overall behavior in both cases. It is worth noting that the β rules are constructed on the assumption of time-independent plasticity (the viscosity is taken into account only at the local scale) whereas translated field models introduce viscous effects in the scale relation. The fact that the macroscopical curves of the two mean-field models are collapsed could suggest that viscoplastic accommodations have a second order impact in this kind of test. Future works must be conducted to study the orientation and neighboring effects on the local behavior. Otherwise, even if the macroscopical test is unidirectional, grains are exposed to multi-axial loadings. It could be interesting to study locally the predictive capabilities of mean-field models on the residual stress and strain evolution.

References

1. Abdul-Latif A, Dingli JP, Saanouni K (1998) Modeling of complex cyclic inelasticity in heterogeneous polycrystalline microstructure. Mech Mater 30:287–305
2. Ausias G, Thuillier S, Omnès B, Wiessner S, Pilvin P (2007) Micro-mechanical model of TPE made of Polypropylene and rubber waste. Polymer 48:3367–3376. doi:http://dx.doi.org/10.1016/j.polymer.2007.03.049
3. Berveiller M, Zaoui A (1979) An extension of the self-consistent scheme to plastically flowing polycrystal. J Mech Phys Solids 26:325–344
4. Bishop J, Hill R (1951) A theoretical derivation of the plastic properties of a polycrystalline face-centered metal. Philos Mag 42:414–427
5. Budianski B, Wu T (1962) Theoretical prediction of plastic strains of polycrystals. In: Proceedings 4th U.S. national congress of applied mechanics, pp 1175–1185
6. Busso E, Cailletaud G (2005) On the selection of active slip systems in crystal plasticity. Int J Plast 21:2212–2231
7. Cailletaud G (1987) Une approche micromécanique phénoménologique du comportement inélastique des métaux. Ph.D. thesis, Université Pierre et Marie Curie
8. Cailletaud G, Pilvin P (1994) Utilisation de modèles polycristallins pour le calcul par éléments finis. Revue Européenne des Éléments Finis 3(4):515–541
9. Cailletaud G, Saï K (2008) A polycrystalline model for the description of ratchetting: effect of intergranular and intragranular hardening. Mater Sci Eng A 480:24–39
10. Dingli JP, Abdul-Latif A, Saanouni K (2000) Predictions of the complex cyclic behavior of polycrystals using a self-consistent modeling. Int J Plast 16:411–437
11. Doghri I, Adam L, Bilger N (2010) Mean-field homogenization of elasto-viscoplastic composites based on a general incrementally affine linearization method. Int J Plast 26:219–238
12. Doghri I, Brassart L, Adam L, Gérard JS (2011) A second-moment incremental formulation for the mean-field homogenization of elasto-plastic composites. Int J Plast 27:352–371
13. Eshelby J (1957) The determination of the elastic field of an ellipsoidal inclusion, and related problems. Proc R Soc Lond 241:376–396

14. Hashin Z, Shtrikman S (1962) On some variational principles in anisotropic and nonhomogeneous elasticity. J Mech Phys Solids 10:335–342
15. Hill R (1965) Continuum micro-mechanisms of elastoplastic polycrystals. J Mech Phys Solids 13:89–101
16. Hutchinson J (1966) Bounds and self-consistent estimates for creep of polycrystalline materials. Proc R Soc Lond A348:101–127
17. Kouddane R, Zouhal N, Molinari A (1994) Complex loading of viscoplastic materials: micro-macro modelling. Mater Sci Eng A175:31–36
18. Kröner E (1961) Zur plastischen Verformung des Vielkristalls. Acta Metall 9:155–161
19. Lahellec N, Suquet P (2013) Effective response and field statistics in elasto-plastic and elasto-viscoplastic composites under radial and non-radial loadings. Int J Plast 42:1–30
20. Lebensohn R, Tomé CN (1993) A self-consistent anisotropic approach for the simulation of plastic deformation and texture development of polycrystals: application to zirconium alloys. Acta Metall 41:2611–2624
21. Lebensohn R, Tomé CN (1994) A self-consistent viscoplastic model: prediction of rolling textures of anisotropic polycrystals. Mater Sci Eng A 175:71–82
22. Lebensohn R, Castaneda PP, Brenner R, Castelnau O (2011) Full-field vs. homogenization methods to predict microstructure-property relations for Polycrystalline materials. In: Ghosh S, Dimiduk D (eds) Computational methods for microstructure-property relationships. Springer, Berlin
23. Liu Y, Ponte-Castaneda P (2004) Homogenization estimates for the average behavior and field fluctuations in cubic and hexagonal viscoplastic polycrystals. J Mech Phys Solids 52:1175–1211
24. Mareau C, Berbenni S (2015) An affine formulation for the self-consistent modeling of elasto-viscoplastic heterogeneous materials based on the translated field method. Int J Plast 64:134–150
25. Martin G, Ochoa N, Sai K, Hervé-Luanco E, Cailletaud G (2014) A multiscale model for the elastoviscoplastic behavior of directionally solidified alloys: application to fe structural computations. Int J Solids Struct 51:1175–1187
26. Masson R, Zaoui A (1999) Self-consistent estimates for the rate-dependent elastoplastic behaviour of polycrystalline materials. J Mech Phys Solids 47:1543–1568
27. Masson R, Bornert N, Suquet M, Zaoui A (2000) An affine formulation for the prediction of the effective properties of nonlinear composites and polycrystals. J Mech Phys Solids 48:1203–1227
28. Méric L, Cailletaud G (1991) Single crystal modeling for structural calculations. Part 2: finite element implementation. J Eng Mater Technol 113:171–182
29. Molinari A, Canova G, Ahzi S (1987) A self-consistent approach to the large deformation polycrystal viscoplasticity. Acta Metall 35:2983–2994
30. Mori T, Tanaka K (1973) Average stress in matrix and average elastic energy of materials with misfitting inclusions. Acta Metall 21:571–574
31. Nemat-Nasser S, Obata M (1986) Rate-dependent, finite elasto-plastic deformation of polycrystals. Proc R Soc Lond A 407:343–375
32. Pan J, Rice JR (1983) Rate sensitivity of plastic flow and implications for yield-surface vertices. Int J Solids Struct 19:973–987
33. Paquin A, Sabar H, Berveiller M (1999) Integral formulation and self-consistent modelling of elastoviscoplastic behavior of heterogeneous materials. Appl Mech Rev 69:14–35
34. Ponte-Castaneda P (1991) The effective mechanical properties of nonlinear isotropic composites. J Mech Phys Solids 39:45–71
35. Ponte-Castaneda P (1996) Exact second-order estimates for the effective mechanical properties of nonlinear composite materials. J Mech Phys Solids 44:827–862
36. Rekik A, Allaoui S, Gasser A, Blond E, Adreev K, Sinnema S (2015) Experiments and nonlinear homgenization sustaining mean-field theories for refractory mortarless masonry: the classical secant procedure and its improved variants. Eur J Mech A Solids 49:67–81

37. Sabar H, Berveiller M, Favier V, Berbenni S (2002) A new class of micro-macro models for elastic-viscoplastic heterogeneous materials. Int J Solids Struct 39:3257–3276
38. Sai K (2011) Multi-mechanism models: present state and future trends. Int J Plast 27:250–281
39. Sai K, Cailletaud G, Forest S (2006) Micro-mechanical modeling of the inelastic behavior of directionally solidified materials. Mech Mater 38:203–217
40. Sauzay M (2006) Effet de l'anisotropie élastique cristalline sur la distribution des facteurs de Schmid à la surface des polycristaux. Technical report, Comptes Rendus de Mécanique
41. Suquet P (1985) Elements of homogeneization for inelastic solid mechanics. In: Sanchez-Palencia E, Zaoui A (eds) Homogeneization techniques for composite media. Springer, New York, pp 193–278
42. Suquet P (1987) Elements of homogenization for inelastic solid mechanic. In: Homogenization techniques for composite media. Springer, New York, pp 193–278
43. Suquet P, Lahellec N (2014) Elasto-plasticity of heterogeneous materials at different scales. Procedia IUTAM 10:247–262
44. Taylor G (1938) Plastic strain in metals. J Inst Met 62:307–324
45. Weng GJ (1983) Cyclic stress relaxation of polycrystalline metals at elevated temperature. Int J Solids Struct 19(6):541–551
46. Yoshida K, Brenner R, Bacroix B, Bouvier S (2009) Effect of regularization of schmid law on self-consistent estimates for rate-independent plasticity of polycrystals. Eur J Mech A Solids 28:905–915
47. Zaoui A (1997) Structural morphology and constitutive behaviour of microheterogeneous materials. In: Suquet P (ed) Continuum micromechanic. Springer, New York, pp 291–347
48. Zaoui A, Masson R (2000) Micromechanics-based modeling of plastic polycrystals: an affine formulation. Mater Sci Eng A285:418–424
49. Zeng T, Shao J, Xu W (2014) Multiscale modeling of cohesive geomaterials with a polycrystalline approach. Mech Mater 69:132–145

A Numerical Assessment of Phase-Field Models for Fracture

René de Borst, Stefan May, and Julien Vignollet

Abstract We first give a concise description of phase-field models for the brittle and the cohesive approach to fracture. For brittle fracture we will address issues like the impact of the internal length scale parameter and the degradation function that are prominent in the model, and whether the functional that describes the smeared crack approaches that of the discrete crack in the limiting case that the internal length scale parameter vanishes. By an example we will show that this Γ-convergence is not necessarily attained numerically. For cohesive fracture the crack opening must be explicitly available as input for the cohesive traction-relative displacement relation. The resulting three-field problem can be solved properly on structured meshes when using a balanced interpolation of the field variables: displacements, phase field, and crack opening. A patch test shows that this does not necessarily extend to unstructured meshes.

1 Introduction

Basically, two methods exist to capture discontinuities: one can either distribute them over a finite width, or handle them as true discontinuities, i.e. in a discrete sense. When a discontinuity has a stationary character it is straightforward to describe it in a discrete manner. An evolving or moving discontinuity is more difficult to capture. One possibility is to adapt the mesh upon every change in the topology, as was done by Ingraffea and co-workers in the context of linear elastic fracture mechanics [1], and later for cohesive fracture [2].

The other approach to fracture is to model it within the framework of continuum mechanics. A fundamental problem then emerges, namely that standard continuum models do not furnish a *non-zero internal length scale*. To remedy this deficiency, regularisation methods have been proposed, including nonlocal averaging, the addition of viscosity or rate dependency, or the inclusion of couple stresses or higher-order strain gradients [3]. The effect of these strategies is that

R. de Borst (✉) • S. May • J. Vignollet
University of Glasgow, Rankine Building, Oakfield Avenue, Glasgow G12 8LT, UK
e-mail: Rene.DeBorst@glasgow.ac.uk; S.May.2@research.gla.ac.uk;
Julien.Vignollet@glasgow.ac.uk

P. Trovalusci (ed.), *Materials with Internal Structure*, Springer Tracts
in Mechanical Engineering, DOI 10.1007/978-3-319-21494-8_2

the discontinuity is transformed into a continuous displacement distribution. The internal length scale is set by the constitutive model, and for a sufficiently fine discretisation, the numerically calculated results are objective with respect to mesh refinement. Particularly in damage mechanics, gradient approaches have gained popularity [4].

Not unrelated to gradient damage approaches are the phase-field models for fracture. However, the point of departure is different. In gradient damage models intrinsically a mechanical approach is adopted, and the damage model is regularised by adding gradients to restore well-posedness of the boundary value problem in the post-peak regime. The basic idea of phase-field models, on the other hand, is to replace the zero-width discontinuity by a small, but finite zone with sharp gradients in a mathematically consistent manner. Indeed, the latter requirement inevitably leads to spatial derivatives in the energy functional, similar to gradient damage models. The first attempts to apply phase-field models for fracture have focused on brittle fracture. Pioneering work has been done in [5–7], where a phase-field approximation was proposed for the variational approach to brittle fracture.

An extension of the variational formulation for brittle fracture to cohesive fracture has been considered in [6], and a phase-field approximation has been developed in [8], with a focus on the application to adhesive fracture, i.e. debonding along a predefined interface. As pointed out in [8], models for brittle and cohesive fracture rely on very different concepts, and the development of a cohesive phase-field model that works for arbitrary configurations and loading conditions is a non-trivial task.

2 Phase-Field Representation for a Crack

The basic idea of phase-field models is to approximate a discontinuity Γ by a smeared surface Γ_ℓ. In a one-dimensional setting the exponential function

$$d(x) = e^{-\frac{|x|}{2\ell}} \tag{1}$$

is used to approximate the discontinuous function of Fig. 1a, with ℓ the internal length scale parameter. The phase-field variable $d \in [0, 1]$ describes the phase field. Herein, d is defined such that $d = 0$ characterises the intact state of the material, while $d = 1$ represents the fully broken material, similar to the definition commonly adopted in damage mechanics. For the one-dimensional case, Eq. (1) is the solution to the differential equation

$$d - 4\ell^2 d_{,xx} = 0, \tag{2}$$

where a comma denotes differentiation, and which is subject to the boundary conditions: $d(0) = 1$ and $d(\pm\infty) = 0$. This can be demonstrated simply by

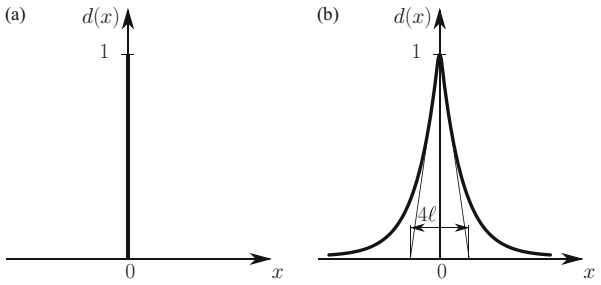

Fig. 1 (**a**) A sharp crack, and (**b**) smeared crack modelled with the length scale parameter ℓ

applying the Ansatz function $d = e^{-|\lambda||x|}$ to Eq. (2), solving for λ and subsequently using the boundary conditions to determine the constant parameter.

Using Eq. (2) the discontinuity Γ can be approximated by the functional Γ_ℓ

$$\Gamma_\ell = \int_\Omega \underbrace{\frac{1}{4\ell}\left(d^2 + 4\ell^2 d_{,x}{}^2\right)}_{\gamma_\ell} \mathrm{d}V, \tag{3}$$

with γ_ℓ the crack surface density function, see [9] for details. In a multi-dimensional setting γ_ℓ can be expanded as follows:

$$\gamma_\ell = \frac{1}{4\ell}\left(d^2 + 4\ell^2 d_{,i} d_{,i}\right). \tag{4}$$

3 Brittle Fracture

3.1 Derivation

We consider a volume Ω with an internal discontinuity boundary Γ_d. As a starting point we consider the potential energy for the case of a discrete description of brittle fracture in the Griffith sense [7]:

$$\Psi_{\text{pot}} = \int_\Omega \psi^e(\boldsymbol{\varepsilon})\,\mathrm{d}V + \int_{\Gamma_d} \mathscr{G}_c\,\mathrm{d}A \tag{5}$$

with the elastic energy density ψ^e a function of the infinitesimal strain tensor $\boldsymbol{\varepsilon}$. The elastic energy density is expressed by Hooke's law for an isotropic linear elastic material as:

$$\psi^e(\boldsymbol{\varepsilon}) = \frac{1}{2}\lambda\varepsilon_{ii}\varepsilon_{jj} + \mu\varepsilon_{ij}\varepsilon_{ij} \tag{6}$$

with λ and μ the Lamé constants, and the summation convention applies. In Eq. (5) the fracture energy, i.e. the amount of energy dissipated upon the creation of a unit of fracture surface, is denoted by $\mathscr{G}_c$. The potential energy Ψ_{pot} governs the balance between elastic energy in the bulk material and the fracture energy.

In the spirit of the regularised crack topology introduced in Sect. 2, the work required to create a unit crack area is now expressed as a volume integral which depends on the phase-field variable d and the fracture energy $\mathscr{G}_c$:

$$\int_{\Gamma_d} \mathscr{G}_c \mathrm{d}A = \int_{\Omega} \mathscr{G}_c \gamma_\ell(d, \nabla d)\, \mathrm{d}V. \tag{7}$$

The next step is inspired by damage mechanics concepts and relies on the assumption that the evolution of the phase field is directly related to crack growth. As such, it can be thought of as a way to model the loss of stiffness of the bulk of the solid. For this purpose a degradation function $g = g(d)$ is introduced, which must satisfy the following conditions: $g : [0, 1] \to [0, 1], g(1) = 0, g'(0) < 0, g'(1) = 0$. These properties ensure damage propagation and provide an upper bound to the phase-field d variable of one [10]. A quadratic polynomial is widely used:

$$g(d) = (1 - d)^2. \tag{8}$$

Recently, Borden [11] has introduced a cubic degradation function:

$$g_s(d) = s((1 - d)^3 - (1 - d)^2) + 3(1 - d)^2 - 2(1 - d)^3, \tag{9}$$

which has the advantage that it better mimics linear elastic-brittle behaviour.

In [5] the degradation function g was multiplied with the elastic energy density of the undamaged state, ψ_0, such that the elastic energy density of the damaged state reads:

$$\psi^e(\boldsymbol{\varepsilon}, d) = g(d)\psi_0(\boldsymbol{\varepsilon}). \tag{10}$$

This formulation was subsequently refined to account for the fact that damage evolution occurs under different straining modes [11, 12], and it was assumed that the elastic energy of the undamaged state can be additively decomposed into a damaged and an intact part, $\psi_0 = \psi_0^{\mathrm{d}} + \psi_0^{\mathrm{i}}$, such that the degradation function g only acts on the damaged part:

$$\psi^e(\boldsymbol{\varepsilon}, d) = g(d)\psi_0^{\mathrm{d}}(\boldsymbol{\varepsilon}) + \psi_0^{\mathrm{i}}(\boldsymbol{\varepsilon}). \tag{11}$$

Substituting Eqs. (7) and (11) into Eq. (5) yields the total potential energy of the smeared form for brittle fracture:

$$\Psi = \int_{\Omega} \left(g(d)\psi_0^{\mathrm{d}}(\boldsymbol{\varepsilon}) + \psi_0^{\mathrm{i}}(\boldsymbol{\varepsilon}) + \mathscr{G}_c \gamma_l(d, \nabla d) \right) \mathrm{d}V. \tag{12}$$

Minimisation of Ψ and introduction of a history field $\mathscr{H}$ to enforce irreversibility [10] lead to the strong form:

$$\operatorname{div} \boldsymbol{\sigma}(\boldsymbol{\varepsilon}, d) = \mathbf{0} \qquad \mathbf{x} \in \Omega \tag{13a}$$

$$\mathscr{G}_c\left(\frac{d}{2\ell^2} - 2\Delta d\right) = g'\mathscr{H} \qquad \mathbf{x} \in \Omega \tag{13b}$$

subject to the boundary conditions $\mathbf{n} \cdot \boldsymbol{\sigma} = \bar{\mathbf{t}}$, $\mathbf{u} = \bar{\mathbf{u}}$, $\mathbf{n} \cdot \nabla d = 0$, with $\bar{\mathbf{t}}$ and $\bar{\mathbf{u}}$ the prescribed boundary tractions and displacements, respectively. The Cauchy stress $\boldsymbol{\sigma}$ and history field $\mathscr{H}$ read:

$$\boldsymbol{\sigma}(\boldsymbol{\varepsilon}, d) = g(d)\frac{\partial \psi_0^{\mathrm{d}}}{\partial \boldsymbol{\varepsilon}} + \frac{\partial \psi_0^{\mathrm{i}}}{\partial \boldsymbol{\varepsilon}} \tag{14}$$

$$\mathscr{H}(t) = \max_t \psi_0^{\mathrm{d}}(t). \tag{15}$$

3.2 Analysis of a One-Dimensional Bar

Now, the one-dimensional bar of Fig. 2 is considered. The bar has a reduced thickness in the centre and is loaded at the right edge by a force $\lambda \hat{f}$. The Young's modulus is $E = 10\,\mathrm{MPa}$ and the fracture toughness $\mathscr{G}_c = 0.1\,\mathrm{N/mm}$. The bar has a length $L = 1\,\mathrm{mm}$ and a thickness $b = 1\,\mathrm{mm}$. The length scale parameter is chosen to be $\ell = \frac{L}{20}$. Since the problem is one-dimensional, $\psi_0^{\mathrm{d}} = E$ and $\psi_0^{\mathrm{i}} = 0$, so that the degradation function g directly acts on the Young's modulus E.

Inspection of the strong form, Eq. (13b), shows that at the onset of loading the "driving force" term $g'\mathscr{H} = g'\psi_0^{\mathrm{d}}(\varepsilon)$ starts to grow, forcing the phase field, and consequently also the crack density γ_ℓ, to increase along the entire bar. As shown by Eq. (7), this process dissipates energy, which explains the early departure from linearity of the force-displacement curve in Fig. 3.

Next, the importance of using a monolithic solver for this nonlinear problem is studied. For a constant mesh size (150 elements, $h = 0.0067\,\mathrm{mm}$) and a length scale $\ell = 0.05\,\mathrm{mm}$, the response of the system for the staggered and the monolithic schemes is compared. Figure 3 shows that the staggered scheme is very sensitive to the size of the load increments, and has not converged for the smallest step size.

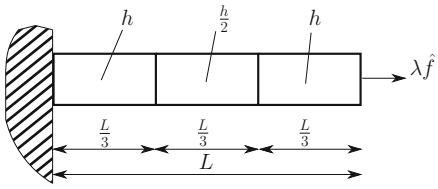

Fig. 2 1D tension test for a bar with a reduced thickness in the centre

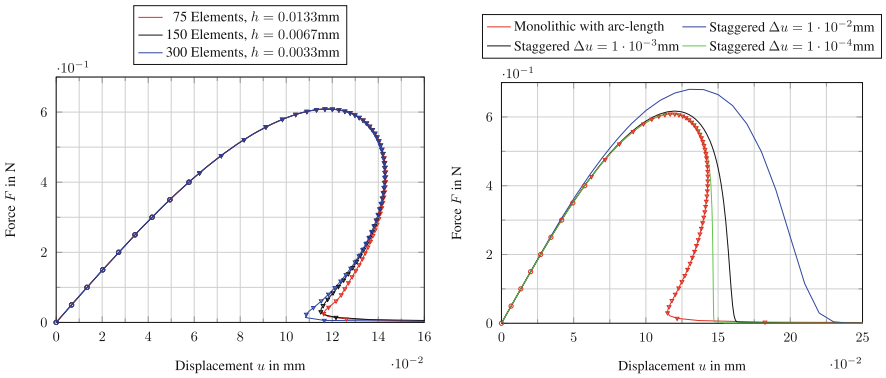

Fig. 3 *Left*: mesh refinement study for a constant length scale $\ell = 0.05$ mm. *Right*: comparison of the monolithic and the staggered approaches for $\ell = 0.05$ mm with a constant mesh size (150 elements, $h = 0.0067$ mm)

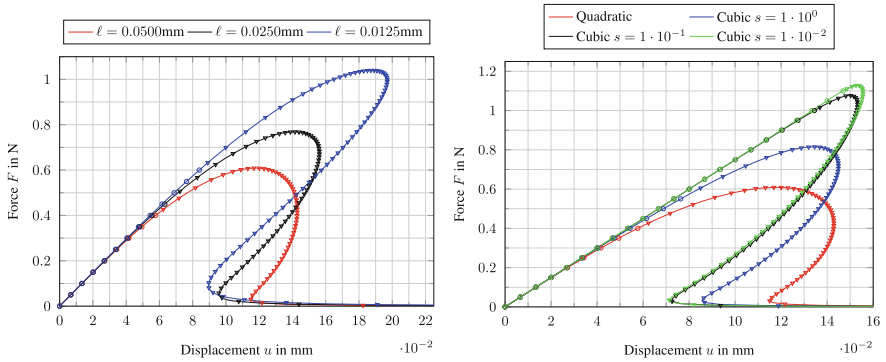

Fig. 4 *Left*: influence of the length scale parameter ℓ for a constant mesh size (150 elements, $h = 0.0067$ mm). *Right*: comparison of the quadratic and cubic degradation functions

The dependence on the length scale ℓ is shown in Fig. 4 for a constant mesh size (150 elements, $h = 0.0067$ mm), which respects the rule of thumb $h < \ell$ to accurately approximate the crack topology proposed in [9], which implies that there are at least four elements over the smeared crack width, see Fig. 1b. Clearly, an increasing length scale results in a decreasing peak force. This makes it difficult to interpret the length scale parameter for the brittle model. On the one hand, ℓ has been introduced on mathematical grounds, Sect. 2, independent from the mechanical field problem. On the other hand, when linking the phase field and the mechanical field, the length scale parameter behaves like a material parameter, cf. [12].

From Figs. 3 and 4 it appears that the brittle model does not exhibit linear elastic behaviour prior to softening. Instead, the curves show nonlinearity from the very beginning. Therefore, a cubic degradation function has been proposed in [11], which results in a linear behaviour up to the peak force. The drawback of this function is

that an additional parameter s is introduced, cf. Eq. (9). The quadratic and the cubic degradation functions are compared in Fig. 4 using different parameters s. For $s \to 0$ the peak force converges to a unique value.

Next, a convergence study has been carried out with respect to the *final* crack surface Γ_ℓ. The purpose is to check whether Γ_ℓ converges to Γ in a non-linear computation. The theoretical *final* crack surface for the bar of Fig. 2 is $\Gamma = A/2$, which is equal to the cross section of the segment in the centre of the bar. The numerically obtained *final* crack surface Γ_ℓ can be calculated using Eq. (3) with Γ_ℓ evaluated when $\max d > 0.99$, and the error Γ_E is defined according to:

$$\Gamma_{\mathrm{E}} = \frac{|\Gamma_\ell - \Gamma|}{\Gamma}. \tag{16}$$

Figure 5 gives the convergence study of the *final* crack surface Γ_ℓ when using the quadratic degradation function for different values of the length scale parameter ℓ. In this convergence study the correction factor to the fracture energy proposed in [6] has been taken into account. Three mesh sizes h have been used, and the internal length scale ℓ has been varied for each mesh size. Figure 5 shows that all results give a rather poor approximation of the theoretical *final* crack surface Γ, since invariably the error $\Gamma_{\mathrm{E}} > 0.1$. Below a certain value of the ratio ℓ/h, a further decrease results in an increase of the error Γ_{E}. The minimum occurs for the same value of the internal length scale, $\ell = 0.05\,\mathrm{mm}$. It is remarkable that for finer meshes the error Γ_{E} does *not* decrease.

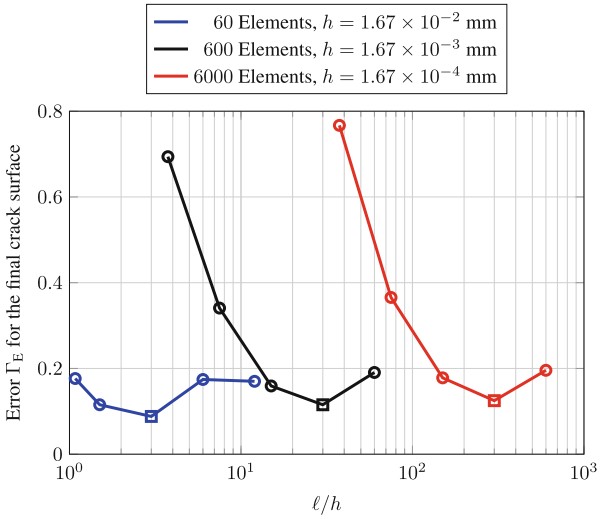

Fig. 5 Convergence study for the *final* crack surface Γ_ℓ for a one-dimensional bar. The *squares* correspond to $\ell = 0.05\,\mathrm{mm}$

4 Phase-Field Model for Cohesive Fracture

4.1 Continuum Formulation

For cohesive zone models the fracture energy $\mathscr{G}_c$ is released gradually and governed by the fracture energy function

$$\mathscr{G} = \mathscr{G}(\llbracket u_i \rrbracket). \tag{17}$$

The fracture energy function $\mathscr{G}$ depends on the crack opening $\llbracket u_i \rrbracket$ at the interface and equals the fracture energy $\mathscr{G}_c$ at full crack opening. The traction t_i in the cohesive zone is evaluated as:

$$t_i(\llbracket u_j \rrbracket) = \frac{\partial \mathscr{G}(\llbracket u_j \rrbracket)}{\partial \llbracket u_i \rrbracket}. \tag{18}$$

In the phase-field model for cohesive fracture, the crack is distributed over the solid, again by employing Eq. (3):

$$\int_\Gamma \mathscr{G}(\llbracket u_i \rrbracket)\, \mathrm{d}A = \int_\Omega \mathscr{G}(\llbracket u_i \rrbracket)\gamma_\ell \, \mathrm{d}V. \tag{19}$$

The spatial distribution in Eq. (19) should not affect $\mathscr{G}(\llbracket u_i \rrbracket)$ in the direction normal to the crack since, for any quantity $\mathscr{B}$, $\int_\Gamma \mathscr{B}\, \mathrm{d}A = \int_\Omega \mathscr{B}\gamma_\ell \, \mathrm{d}V$. The crack opening $\llbracket u_i \rrbracket$, and therefore $\mathscr{G}(\llbracket u_i \rrbracket)$, only exists at the crack surface Γ. For this reason, an auxiliary field v_i is introduced when distributing the crack, which is defined over the volume Ω. Since $\mathscr{G}(v_i)$ must not change in the direction normal to the crack, the following constraint is enforced on the auxiliary field v_i:

$$\frac{\partial v_i}{\partial n} = 0. \tag{20}$$

Evidently, v_i being constant in the direction normal to the crack implies that $\mathscr{G}(v_i)$ is constant as well. The expression for Eq. (19) thus becomes:

$$\int_\Gamma \mathscr{G}(\llbracket u_i \rrbracket)\, \mathrm{d}A = \int_\Omega \mathscr{G}(v_i)\gamma_\ell \, \mathrm{d}V \quad \text{subject to } \frac{\partial v_\mathrm{i}}{\partial n} = 0. \tag{21}$$

The phase-field model for cohesive fracture assumes a split of the strain tensor into an elastic component and a component that accounts for damage:

$$\varepsilon_{ij} = \varepsilon_{ij}^{\mathrm{el}} + \varepsilon_{ij}^{\mathrm{d}} \tag{22}$$

such that in Eq. (6) ε_{ij} needs to be replaced by $\varepsilon_{ij}^{\mathrm{el}}$, which finally yields for the stress:

$$\sigma_{ij} = \frac{\partial \psi^{\mathrm{el}}}{\partial \varepsilon_{ij}} = \frac{\partial \psi^{\mathrm{el}}}{\partial \varepsilon_{kl}^{\mathrm{el}}} \frac{\partial \varepsilon_{kl}^{\mathrm{el}}}{\partial \varepsilon_{ij}} = \frac{\partial \psi^{\mathrm{el}}}{\partial \varepsilon_{kl}^{\mathrm{el}}} \delta_{ki} \delta_{lj} = \frac{\partial \psi^{\mathrm{el}}}{\partial \varepsilon_{ij}^{\mathrm{el}}}. \tag{23}$$

The tensor $\varepsilon_{ij}^{\mathrm{d}}$ that accounts for damage can be derived from thermodynamical considerations. The second law of thermodynamics gives [13]:

$$\dot{\mathscr{D}} = \sigma_{ij}\dot{\varepsilon}_{ij} - \dot{\psi}^{\mathrm{el}} = \sigma_{ij}(\dot{\varepsilon}_{ij}^{\mathrm{el}} + \dot{\varepsilon}_{ij}^{\mathrm{d}}) - \frac{\partial \psi^{\mathrm{el}}}{\partial \varepsilon_{ij}^{\mathrm{el}}} \dot{\varepsilon}_{ij}^{\mathrm{el}} = \sigma_{ij}(\dot{\varepsilon}_{ij}^{\mathrm{el}} + \dot{\varepsilon}_{ij}^{\mathrm{d}}) - \sigma_{ij}\dot{\varepsilon}_{ij}^{\mathrm{el}} = \sigma_{ij}\dot{\varepsilon}_{ij}^{\mathrm{d}} \geq 0. \tag{24}$$

The dissipation $\dot{\mathscr{D}}$ for the distributed form in Eq. (21) can be evaluated explicitly from

$$\dot{\mathscr{D}} = \frac{\mathrm{d}}{\mathrm{d}t}\big(\gamma_\ell(d)\mathscr{G}(v_i)\big) = \mathscr{G}\frac{\partial \gamma_\ell}{\partial d}\dot{d} + \gamma_\ell \frac{\partial \mathscr{G}(v_j)}{\partial v_i}\dot{v}_i = \mathscr{G}\frac{\partial \gamma_\ell}{\partial d}\dot{d} + \gamma_\ell t_i \dot{v}_i. \tag{25}$$

The first term in Eq. (25) corresponds to the energy that is dissipated when advancing the cohesive zone by $\dot{d}$. Assuming that the smeared jump v_i is initially zero in the newly created cohesive zone, the first term does not contribute to dissipation of energy, since $\mathscr{G}(0) = 0$. The second term in Eq. (25) represents the energy dissipation as the result of further crack opening by $\dot{v}_i$. Substituting Eq. (25) into Eq. (24)

$$\gamma_\ell t_i \dot{v}_i = \sigma_{ij}\gamma_\ell \mathrm{sym}(\dot{v}_i n_j) = \sigma_{ij}\dot{\varepsilon}_{ij}^{\mathrm{d}} \tag{26}$$

yields $\varepsilon_{ij}^{\mathrm{d}}$, the contribution of the strain tensor that accounts for damage:

$$\varepsilon_{ij}^{\mathrm{d}} = \gamma_\ell \mathrm{sym}(v_i n_j). \tag{27}$$

The potential of the phase-field model for cohesive fracture now reads:

$$\Psi = \int_\Omega \left(\psi^{\mathrm{el}} + \mathscr{G}(v_i)\gamma_\ell + \frac{\alpha}{2}\left|\frac{\partial v_i}{\partial n}\right|^2 \right) \mathrm{d}V \tag{28}$$

where the last term has been introduced in order to enforce Eq. (20). Minimising Ψ yields:

$$\sigma_{ij,i} = 0 \qquad \text{in } \Omega, \tag{29}$$

$$\gamma_\ell[t_i(v_j) - \sigma_{ij}n_j] = \alpha\frac{\partial^2 v_i}{\partial n^2} \qquad \text{in } \Gamma_\ell \tag{30}$$

subject to the boundary conditions $\sigma_{ij}n_j = \bar{t}_i$ on $\partial\Omega_h$, $u_i = \bar{u}_i$ on $\partial\Omega_u$ and $\frac{\partial v_i}{\partial n} = 0$ on $\partial\Gamma_\ell$.

4.2 Numerical Examples for the Phase-Field Model for Cohesive Fracture

In what follows, a constant phase field d is considered, i.e. an interface is modelled. For this purpose a one-dimensional bar is considered with an elastic interface, Fig. 6. First, the bar is modelled with one-dimensional bar elements. The Young's modulus is $E = 10\,\mathrm{MPa}$, the stiffness of the interface $k = 10\,\mathrm{N\,mm^{-3}}$, the length $L = 1\,\mathrm{mm}$ and the length scale parameter is $\ell = L/10$. The penalty parameter is set $\alpha = 1$, and $d = 1$ is prescribed at the elastic interface, i.e. at the node in the centre of the bar. The bar consists of ten elements with five elements in each segment, so that the mesh size is $h = 0.1\,\mathrm{mm}$. The prescribed displacement is $\bar{u}_x = 0.1\,\mathrm{mm}$.

Application of linear shape functions for the displacement u_x, the smeared jump v_x and the phase field d results in stress oscillations, Fig. 7a, as was also observed in [8]. In one dimension, Eq. (22) can be rewritten using Eq. (3) as follows:

$$\varepsilon_{xx}^{\mathrm{el}} = \varepsilon_{xx} - \varepsilon_{xx}^{\mathrm{d}} = \frac{\mathrm{d}u_x}{\mathrm{d}x} - \gamma_\ell v_x = \frac{\mathrm{d}u_x}{\mathrm{d}x} - \frac{1}{4\ell}(d^2 + 4\ell^2 d_{,x}{}^2)v_x. \tag{31}$$

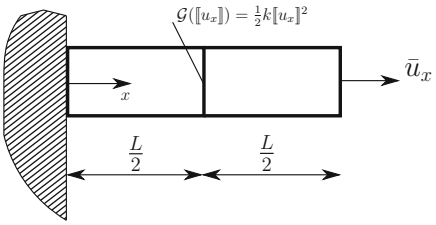

Fig. 6 Bar with an elastic interface $\mathscr{G} = \frac{1}{2}k[\![u_x]\!] = \frac{1}{2}kv_x^2$ in the centre; with Eq. (18) the cohesive traction becomes $t_x = k[\![u_x]\!] = kv_x$

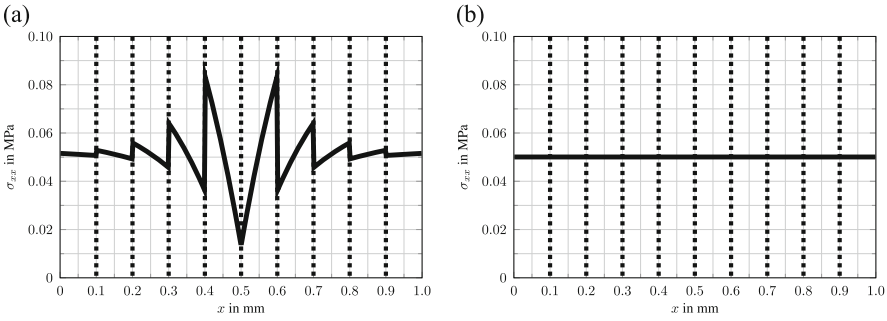

Fig. 7 Stress distribution along the bar in Fig. 6 for (**a**) linear shape functions for u_x, v_x, d and (**b**) cubic shape functions for u_x and linear shape functions for v_x, d; the *dashed lines* mark element boundaries

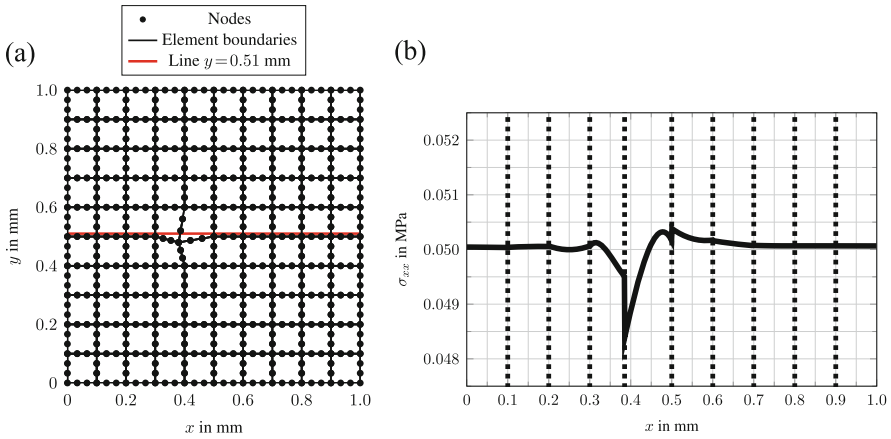

Fig. 8 For the unstructured mesh in (**a**) stress oscillations can be observed along the line $y = 0.51$ mm in (**b**). *Dashed lines* correspond to element boundaries

Since v_x is enforced to be constant, the strain $\varepsilon_{xx}^{\mathrm{d}}$ that accounts for damage has a quadratic distribution when linear shape functions are used for d. Therefore, the total strain ε_{xx} must have a quadratic distribution as well. This can be achieved when cubic shape functions are used for the displacement u_x. Figure 7b shows that this is a good solution.

Keeping the interpolation of the displacement of the third order while those for the phase field and the crack opening remain linear, the bar is now reconsidered in a two-dimensional setting by putting Poisson's ratio $\nu = 0$ and by prescribing all $v_y = 0$. A structured mesh with 10×10 elements is used. The width is $c = 1$ mm and $d = 1$ is prescribed at all nodes for which $x = L/2$. The other parameters are the same as in the purely one-dimensional case. No stress oscillations are observed.

Next, the nodes are slightly displaced in a patch of four elements, Fig. 8a, and stress oscillations result along the line $y = 0.51$ mm, see Fig. 8b, cf. [14], where the use of unstructured meshes for a peel test also resulted in stress oscillations. The present simulation can be considered as a patch test, since a homogeneous stress state should be obtained when prescribing a uniform traction or displacement at the boundary, irrespective of the mesh lay-out. Unfortunately, this is not obtained for the present three-field formulation of the cohesive phase-field fracture model.

5 Concluding Remarks

One-dimensional numerical studies have been discussed for the phase-field approach to brittle fracture. They indicate that monolithic solution strategies, in which the mechanical problem and the phase field are solved for simultaneously, are more accurate than staggered solution schemes. The simulations also show the

internal length scale parameter ℓ takes on the role of a material parameter, quite similar to the internal length scale parameter in gradient damage models [4]. The same holds for the degradation function $g(d)$, which turns out to have the physical meaning of a material degradation function. Furthermore, the numerical results indicate that, when the internal length scale $\ell \to 0$, the length of the smeared crack does not converge towards the true crack length in the phase-field models for brittle fracture. Loosely speaking, this implies that this numerical experiment suggests that the so-called Γ-convergence is not necessarily attained.

Next, the cohesive phase-field model proposed in [8] was examined numerically. A simple patch test was devised in a two-dimensional setting, with boundary conditions such that a uniform, uniaxial stress state should be obtained. Unfortunately stress oscillations were found when displacing the nodes in a patch of four elements. This renders the current state of the cohesive phase-field approach to fracture not yet applicable to arbitrary loading configurations and discretisations.

References

1. Ingraffea AR, Saouma V (1985) Numerical modelling of discrete crack propagation in reinforced and plain concrete. In: Fracture mechanics of concrete. Martinus Nijhoff Publishers, Dordrecht, pp 171–225
2. Camacho GT, Ortiz M (1996) Computational modelling of impact damage in brittle materials. Int J Solids Struct 33:2899–2938
3. de Borst R, Mühlhaus H-B, Pamin J, Sluys LJ (1993) Fundamental issues in finite element analyses of localization of deformation. Eng Comput 10:99–121
4. Peerlings RHJ, de Borst R, Brekelmans WAM, de Vree HPJ (1996) Gradient-enhanced damage for quasi-brittle materials. Int J Numer Methods Eng 39:3391–3403
5. Bourdin B, Francfort GA, Marigo J-J (2000) Numerical experiments in revisited brittle fracture. J Mech Phys Solids 48:797–826
6. Bourdin B, Francfort GA, Marigo J-J (2008) The variational approach to fracture. J Elast 91:5–148
7. Francfort GA, Marigo J-J (1998) Revisiting brittle fracture as an energy minimization problem. J Mech Phys Solids 46:1319–1342
8. Verhoosel CV, de Borst R (2013) A phase-field model for cohesive fracture. Int J Numer Methods Eng 96:43–62
9. Miehe C, Welschinger F, Hofacker M (2010) Thermodynamically consistent phase-field models of fracture: variational principles and multi-field FE implementations. Int J Numer Methods Eng 83:1273–1311
10. Miehe C, Hofacker M, Welschinger F (2010) A phase field model for rate-independent crack propagation: robust algorithmic implementation based on operator splits. Comput Meth Appl Mech Eng 199:2765–2778
11. Borden MJ (2012) Isogeometric analysis of phase-field models for dynamic Brittle and Ductile fracture. Ph.D. thesis, The University of Texas at Austin
12. Amor H, Marigo J-J, Maurini C (2009) Regularized formulation of the variational brittle fracture with unilateral contact: numerical experiments. J Mech Phys Solids 57:1209–1229
13. Jiràsek M, Bažant ZP (2001) Inelastic analysis of structures. Wiley, Chichester
14. Vignollet J, May S, de Borst R, Verhoosel CV (2014) Phase-field models for brittle and cohesive fracture. Meccanica 49:2587–2601

On the Effective Properties of Elastic Materials and Structures at the Micro- and Nano-Scale Considering Various Models of Surface Elasticity

Victor A. Eremeyev

Abstract We discuss influence of surface properties on effective (apparent) properties of materials and structures such as Young's modulus of a porous rod or bending stiffness of a nanosized plate. We consider various models of surface elasticity by Gurtin–Murdoch, Steigman–Ogden, and its generalizations. Difference between models is discussed, and formulas for some effective properties are given.

1 Introduction

The development of nanotechnologies has recently led to the appearance of new materials with very promising physical properties. A reliable understanding of their mechanical properties is by now of crucial importance. The aim of the paper is to discuss material properties of nanostructured materials at the macroscale considering surface/interface properties. Nowadays it is well established that unusual and sometimes very promising properties of nanomaterials relate with surface/interfacial properties. For example, one can observe the so-called size-effect, that is dependency of material properties on the size of considered specimen, see for example [11, 31] where Young's modulus of nanobeams made of Ag, Pb is presented. Unlike in classical mechanics where the size-effects can be explained by various mechanisms, such as size of grains and subgrains, dislocations density, microcracks, etc., see, for example, [7], at the nanoscale surface effects are the main reason for them. Nanoobjects such as nanowires, nanotubes, nanofibers, etc., can be used as working elements of various nanoelectromechanical systems (NEMS), see [8, 10, 17, 54, 56]. Often nanoelements form thin coatings with regular inner microstructure on a substrate. As an example of such regular coating one can consider arrays of ordered nanowires or nanotubes grown on a substrate

V.A. Eremeyev (✉)
Otto von Guericke University Magdeburg, Universitätplatz 2, 39106 Magdeburg, Germany
South Scientific Centre of RASci & South Federal University, Milchakova St. 8a, 344090 Rostov on Don, Russia
e-mail: eremeyev.victor@gmail.com

P. Trovalusci (ed.), *Materials with Internal Structure*, Springer Tracts in Mechanical Engineering, DOI 10.1007/978-3-319-21494-8_3

[8, 40, 44, 50, 53, 54]. Besides coatings with regular and sometimes periodical inner microstructure there are more interesting modifications of material surfaces based on highly irregular structures similar to classical cellular or fabric materials. Among them there are the so-called self-cleaning and bactericide coatings. The latter are based on recent progresses in the production of superhydrophobic and superoleophobic coatings, see [9, 12, 21, 32, 38] and reference therein. Such coating can nowadays be applied to relatively rigid material such as glass or metal but also to flexible materials such as textile.

The coatings discussed above dramatically change the surface physical properties of the material and the material properties at all. These very promising materials can be called *surface metamaterials* since their properties is almost determined by inner microstructure and interaction forces acting between elements of coating. Detailed description of surface nanostructures like those shown in is not possible, in general, and even not required. This results in the necessity to develop new models of surface-enhanced materials at the nano- and macro-scale.

The origin of mechanics of surface phenomena relates with the pioneer works by Laplace [36, 37], Young [58], Poisson [15] where the surface tension for fluids was introduced and the corresponding boundary-value problems are considered. For recent state of the art of the theory of capillarity we refer to books [23, 45]. Later Gibbs generalized the notion of surface tension in the case of solids [39]. The model of surface elasticity for elastic solids under large deformations was proposed by Gurtin and Murdoch [25]. From the physical point of view the model can be considered as nonlinear solid with attached on its surface an elastic membrane. The stress resultant tensor acting in the membrane can be interpreted as a surface stress. As a result, the constitutive equations for bulk and surface behavior are required, thus for the surface elasticity model, in addition to the three-dimensional constitutive equations, the two-dimensional constitutive relations are also formulated, where the surface stress tensor depends on the surface strain measure. Recently Gurtin–Murdoch model found many applications in micro- and nanomechanics [16, 28, 57]. In particular, the surface stresses are used for the explanation of the aforementioned size-effect [55]. The key problem of the theory is the determination of surface elastic moduli. For determination of the latter, molecular dynamics methods were applied in [41, 49] while in [11] the measurement by atom force microscopy with analysis of size-effect is used.

This model is generalized in [52] where bending stiffness of the attached film is taken into account. For further generalizations we refer to [27, 28] and the references therein. The presence of surface enhancements leads to non-classical mathematical problems. For example, it changes the behavior of solutions near singularities (cracks, holes, notches), see [33, 43]. Mathematical study of the boundary-value problems of the linear elasticity with surface stresses are provided through various methods in [3, 4, 47], see also [20]. The surface elasticity influences the actual (apparent) properties of materials [1, 16, 19, 34, 35, 57]. It was shown that the action of surface stresses leads to the stiffening of the material, see, for example, [4, 16, 55, 57]. Finite element analysis of solids with surface stresses is developed in [28–30].

Other methods of considering of surface elasticity are also known. Among them we mention ab initio methods and other atomistic simulations, see for example [6, 41, 48, 49]. Since we focus on mechanical behavior of surface-enhanced materials we restrict ourselves to continuum methods referring to discrete models only for comparison of results. A different model of surface elasticity was introduced in [26]. Here surface energy was introduced through estimation of excess of bulk energy near the surface. Finally, after the seminal work of Mindlin [42] the surface stresses can be modeled within the framework of the second-gradient theory of elasticity, see for example [13, 14, 22, 45] and references therein.

The paper is organized as follows. Using variational approach in Sect. 2 we briefly discuss some models of surface elasticity. Here we present the basic equations of Gurtin–Murdoch, Steigmann–Ogden models, and further generalizations. Section 3 is devoted to effective properties of materials and structures considering surface phenomena.

2 Models of Surface Elasticity

Using the principle of virtual work here we discuss few models of surface elasticity. For the sake of simplicity we are restricted ourselves by the case of infinitesimal deformations. Let an elastic solid with surface stresses occupies the volume $V \subset \mathbb{R}^3$ with the boundary A. The general form of the principle of virtual work is given by the variational equation

$$\delta \mathfrak{E} = \mathfrak{A}, \tag{1}$$

where $\mathfrak{E}$ is the functional of total energy and $\mathfrak{A}$ the virtual work of external loads, δ stands for the variation symbol. For the surface elasticity models $\mathfrak{E}$ is a sum of volumetric and surface parts

$$\mathfrak{E} = \iiint\limits_V \mathscr{W} \, \mathrm{d}v + \iint\limits_{A_s} \mathscr{U} \, \mathrm{d}a, \tag{2}$$

where $\mathscr{W}$ and $\mathscr{U}$ are the bulk and surface strain energy functions, respectively. A_s is the part of $A = \partial V$ where the surface energy is defined, see Fig. 1a.

For small deformations of an isotropic body we have the following constitutive equations in the bulk

$$\mathscr{W} = \mu \mathbf{e} : \mathbf{e} + \frac{1}{2}\lambda \mathrm{tr}^2 \mathbf{e}, \quad \boldsymbol{\sigma} \equiv \frac{\partial \mathscr{W}}{\partial \mathbf{e}} = 2\mu \mathbf{e} + \lambda \mathbf{I} \mathrm{tr}\, \mathbf{e}, \quad \mathbf{e} = \frac{1}{2}\left(\nabla \mathbf{u} + (\nabla \mathbf{u})^T\right), \tag{3}$$

where $\mathbf{e}$ is the strain tensor, $\mathbf{u}$ is the displacement vector, λ and μ are Lamé moduli, $\mu > 0$, $3\lambda + 2\mu > 0$, and ∇ is the 3D nabla operator.

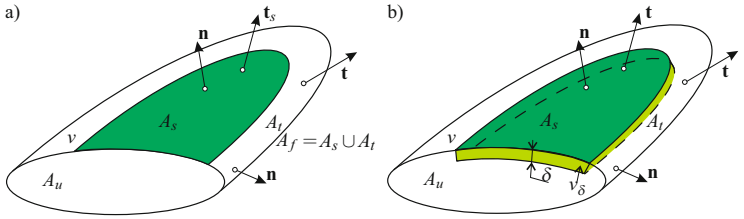

Fig. 1 Material with surface stresses (**a**) and with surface layer (**b**)

In addition to $\mathbf{u}$, we introduce the surface displacement vector $\mathbf{v}$ which describes the displacements of A_s. In this theory the following assumption is usually used that:

$$\mathbf{v} = \mathbf{u}\big|_{A_s}. \tag{4}$$

This compatibility condition plays an important role in the theory. Obviously, it is valid for perfect surfaces while for coatings with complex inner structures it should be replaced by more general relation

$$\mathbf{v} = \mathbb{A}\left[\mathbf{u}\big|_{A_s}\right], \tag{5}$$

where $\mathbb{A}$ is an operator which depends on inner microstructure of coating, see comments in [1]. Indeed, for thin coating $\mathbf{v}$ describes averaged through-the-thickness (mean) displacements attributed to the coating and it does not coincide with $\mathbf{u}\big|_{A_s}$, in general.

In what follows we consider various forms of surface energy density $\mathscr{U}$ which specifies the model of surface elasticity.

2.1 Gurtin–Murdoch Model of Surface Elasticity

Following [25] let us recall the basic equations of Gurtin–Murdoch model of surface elasticity in the case of infinitesimal deformations. The surface strain energy density of an isotropic material is given by

$$\mathscr{U} = \mu_S \boldsymbol{\epsilon} : \boldsymbol{\epsilon} + \frac{1}{2}\lambda_S \mathrm{tr}^2 \boldsymbol{\epsilon}, \qquad \boldsymbol{\epsilon} = \frac{1}{2}\left(\nabla_S \mathbf{v} \cdot \mathbf{A} + \mathbf{A} \cdot (\nabla_S \mathbf{v})^T\right), \tag{6}$$

where λ_S and μ_S are the surface Lamé moduli, ∇_S is the surface nabla operator, $\mathbf{I}$ and $\mathbf{A} \equiv \mathbf{I} - \mathbf{n} \otimes \mathbf{n}$ are the 3D and surface unit tensors, respectively, $\mathbf{n}$ is the unit vector of normal to A_s. In the theory of Gurtin and Murdoch the tensor of surface

stresses $\boldsymbol{\tau}$ is an analogue of membrane stress resultants. It is given by the relation

$$\boldsymbol{\tau} \equiv \frac{\partial \mathscr{U}}{\partial \boldsymbol{\epsilon}} = \mu_S \boldsymbol{\epsilon} + \lambda_S \mathbf{A} \mathrm{tr}\, \boldsymbol{\epsilon}.$$

The key problem of the theory is the determination of surface Lamé moduli λ_S and μ_S. There are restrictions for λ_S and μ_S of mathematical nature, see [3] for details,

$$\mu_S > 0, \quad \lambda_S + \mu_S > 0. \tag{7}$$

Methods of molecular dynamics for determination of λ_S and μ_S were applied in [41, 49] while in [11] the measurement by atom force microscopy with size-effect is used.

Comparison of deformations of a three-layered plate and plate with surface stresses gives us another interpretations of λ_S and μ_S, see [2]. Let us consider tension and bending of a three-layered plate with two thin faces (skins) of thickness h_f with Lamé moduli μ_f and λ_f. For $h_\mathrm{f} \to 0$ with accuracy up to $O(h_\mathrm{f}^2)$ from comparison of the tangential and bending stiffness parameters of the tree-layered plate and the plate with surface stresses it follows that, see [2],

$$\mu_S = \lim_{h_\mathrm{f} \to 0} \mu_\mathrm{f} h_\mathrm{f}, \quad \lambda_S = \lim_{h_\mathrm{f} \to 0} \lambda_\mathrm{f} \frac{1 - 2\nu_\mathrm{f}}{1 - \nu_\mathrm{f}} h_\mathrm{f}. \tag{8}$$

Assuming $\mathfrak{A}$ in the form

$$\mathfrak{A} = \iiint\limits_V \mathbf{f} \cdot \boldsymbol{\delta} \mathbf{u} \, \mathrm{d}v + \iint\limits_{A_f} \mathbf{t} \cdot \boldsymbol{\delta} \mathbf{u} \, \mathrm{d}a,$$

where $\mathbf{f}$ and $\mathbf{t}$ are the body force and surface loads vectors, respectively, A_f is the surface where the external surface loads $\mathbf{f}$ act, $A_s \subset A_f$, and taking into account kinematic boundary conditions $\mathbf{u}\big|_{A_u} = \mathbf{0}$ and (4), from variational equation (1) with constitutive relations (3) and (6) we obtain the equilibrium equations and static boundary conditions for solids with surface stresses

$$\nabla \cdot \boldsymbol{\sigma} + \mathbf{f} = \mathbf{0} \quad \text{in } V, \quad (\mathbf{n} \cdot \boldsymbol{\sigma} - \nabla_S \cdot \boldsymbol{\tau})|_{A_s} = \mathbf{t}, \quad \mathbf{n} \cdot \boldsymbol{\sigma}|_{A_t} = \mathbf{t}. \tag{9}$$

We assume that the part of body surface A_u is fixed, while on $A_t \equiv A_f \backslash A_s$ the surface stresses are absent, see Fig. 1a. The vector of surface forces $\mathbf{t}_s$ at A_s consist of external surface traction $\mathbf{t}$ and vector $\nabla_s \cdot \boldsymbol{\tau}$, so $(9)_2$ takes the form $\mathbf{n} \cdot \boldsymbol{\sigma}|_{A_s} = \mathbf{t}_s$.

2.2 Steigmann–Ogden Model of Surface Reinforcements

Steigman and Ogden extended the model of surface elasticity taking into account the bending stiffness of surface film first for plane problems [51] and then for general 3D case [52]. For infinitesimal deformations of an isotropic material the surface strain energy is now given by the formula

$$\mathscr{U} = \mu_S \boldsymbol{\epsilon} : \boldsymbol{\epsilon} + \frac{1}{2}\lambda_S \mathrm{tr}^2 \boldsymbol{\epsilon} + \eta \boldsymbol{\kappa} : \boldsymbol{\kappa} + \frac{1}{2}\zeta \mathrm{tr}^2 \boldsymbol{\kappa}, \tag{10}$$

$$\boldsymbol{\kappa} = -\frac{1}{2}\left(\nabla_S \boldsymbol{\vartheta} \cdot \mathbf{A} + \mathbf{A} \cdot (\nabla_S \boldsymbol{\vartheta})^T\right), \quad \boldsymbol{\vartheta} = \nabla_S w + \mathbf{B} \cdot \mathbf{u},$$

where $\boldsymbol{\epsilon}$ is defined in (6), $\boldsymbol{\kappa}$ is the bending strain measure called also the tensor of changes of curvature, $w \equiv \mathbf{n} \cdot \mathbf{u}$ is the displacement normal to surface A_s, $\mathbf{B} \equiv -\nabla_S \mathbf{n}$ is the curvature tensor, ζ and η are additional material parameters describing the bending stiffness of material surface A_s.

For Steigmann–Ogden model $\mathfrak{A}$ may include surface moments and edge forces and moments. So, the boundary conditions have also more complex form, see [52] for details.

2.3 Classic Approach

It is worse to mention that surface phenomena can be also modeled using classical approach considering thin surface layer with another material properties than in the bulk, see Fig. 1b. In this case the functional of total energy take the form

$$\mathfrak{E} = \iiint\limits_{V \setminus V_\delta} \mathscr{W} \, \mathrm{d}v + \iiint\limits_{V_\delta} \mathscr{W}_\delta \, \mathrm{d}v, \tag{11}$$

where V_δ is the volume of the surface layer and $\mathscr{W}_\delta$ is the stain energy density. In other words, Eq. (11) relates with non-homogeneous solid where non-homogeneity located near the surface or its part. As a result, the mechanics of composites or theories of laminates can be used for modeling of deformations of solids with surface stresses.

Obviously, one can combine models of surface elasticity using the total energy functional in the form

$$\mathfrak{E} = \iiint\limits_{V \setminus V_\delta} \mathscr{W} \, \mathrm{d}v + \iiint\limits_{V_\delta} \mathscr{W}_\delta \, \mathrm{d}v + \iint\limits_{A_s} \mathscr{U} \, \mathrm{d}a. \tag{12}$$

In the literature are known further generalizations of surface/interface elasticity, see for example [46] where the Cosserat-type model suggested for description of interfacial elasticity.

3 On Effective Properties of Nanomaterials Considering Surface Stresses

The analysis of influence of surface stresses on the effective material properties is given in many works, see [16, 28, 57] and reference therein. To illustrate the possible approach let us discuss the simplest example of tension of a nanoporous rod.

3.1 Stiffness of a Nanoporous Rod

Following [19] in this section we discuss the effective stiffness of a nanoporous rod. We consider a rod with circular cross-section of radius R and n identical pores of radius r which are uniformly distributed parallel to the rod axis. We denote the area of pores in the rod cross-section as $S = \pi n r^2$ and introduce the porosity ϕ by the relation $\phi = S/F$, $F = \pi R^2$, $\phi \in [0, 1)$. Further, assuming the porosity is fixed we consider how the effective Young's modulus depends on the number of pores.

The theory of strength of materials results in elementary formula

$$E_\circ^* = E\,(1 - \varphi)\,. \tag{13}$$

Obviously, there is no influence of surface effects.

Theory of surface stresses leads to

$$E_S^* = E(1 - \varphi) + E_S \frac{2\sqrt{S}}{\sqrt{\pi} F}\sqrt{n} = E_\circ^* + E_S \frac{2\sqrt{S}}{\sqrt{\pi} F}\sqrt{n}. \tag{14}$$

Here E_S is the surface Young modulus.

Mechanics of composites results in

$$E_f^* = E\left(1 - \frac{S + S_\delta}{F}\right) + E_f \frac{S_\delta}{F} = E_\circ^* + (E_f - E)\frac{S_\delta}{F}, \tag{15}$$

where $S_\delta(n) = \pi n[(r + \delta)^2 - r^2]$ is the total area of the surface layers of thickness δ or to

$$E_f^* = E_\circ^* + (E_f - E)\frac{2\delta\sqrt{\pi S}}{F}\sqrt{n}. \tag{16}$$

And, finally, we have the combined formula

$$E^* = E^*_\circ + E_S \frac{2\sqrt{S}}{\sqrt{\pi} F} \sqrt{n} + (E_f - E) \frac{S_\delta(n)}{F}. \tag{17}$$

Here E^* depends on the values of h_f, R, E_S, and E. $d = 2E_S/E$ is the characteristic length parameter introduced in [55].

In a similar way we obtained formulae for effective stiffness parameters for plates and shells [2, 5].

3.2 Scaling Law

In [16, 55] the following scaling law was discussed for nano-structured materials. Let F be some material property, i.e., Young's modulus, temperature of melting, etc. We denote $F(L)$ the value of F for a nano-specimen with characteristic size L and $F(\infty)$ for material in the bulk. According to scaling law [55] we have

$$\frac{F(L)}{F(\infty)} = 1 + \frac{l_{in}}{L} + O\left(\frac{l_{in}}{L}\right)^2. \tag{18}$$

Here l_{in} is a characteristic length, usually $l_{in} = 2$–$20\,\mathrm{nm}$. Among examples of application of (18) is the size-effect observed in [11, 31]. In particular, the effective Young modulus of a rod with circular cross-section of radius R and with surface stresses is given by the formula

$$\frac{E^*_S}{E} = 1 + \frac{l_{in}}{R} \tag{19}$$

with $l_{in} = 2E_S/E$, which entirely coincides with the scaling law (18).

3.3 On Spectrum of Eigen-Oscillations of Solids with Surface Stresses

General mathematical analysis of boundary-value problems of free vibrations of solids with surface stresses performed in [3, 4] using Rayleigh and Courant variational principles. As a result, the following theorem can be proved.

Theorem 1 *Let ω_k^{GM} be eigenfrequencies of a bounded elastic body with surface stresses according to Gurtin–Murdoch model enumerated in increasing order as $\omega_0^{\mathrm{GM}} \le \omega_1^{\mathrm{GM}} \le \omega_2^{\mathrm{GM}}, \ldots$, let ω_k^{SO} be eigenfrequencies of a bounded elastic body with surface stresses according to Steigmann–Ogden model, and let ω_k^f and ω_k° be*

correspondingly ordered eigenfrequencies of the elastic body with free boundary A_S and with fixed boundary, respectively. Then

$$\omega_k^f \leq \omega_k^{\mathrm{GM}} \leq \omega_k^{\mathrm{SO}} \leq \omega_k^{\circ}, \quad k = 1, 2, 3, \ldots. \tag{20}$$

The increase in the eigenfrequencies for the elastic body with surface stresses, in comparison with the same body with free boundary, can be interpreted as the increase in the stiffness. So, in this sense the solids with surface stresses described within Steigmann–Ogden model are stiffer then ones described within Gurtin–Murdoch model.

3.4 On Effective Properties of Solids with Coatings of Complex Inner Structure

For coatings with complex inner microstructure, mentioned in the "Introduction" we propose two steps of homogenization for taking into account the surface properties. The main idea consists of replacing thin coating by material surface with effective properties and then using these properties for determination of material properties at the macrolevel. So we propose to find 2D effective (apparent) material properties and then using these 2D properties obtain 3D effective material properties.

To illustrate the idea let us discuss the effective properties for "foam-like" surfaces such as discussed in [12, 21, 32]. Instead of detailed description of geometry of these structures simple idealized models of cell structures is often used in the mechanics of open-cell foams [24], see Fig. 2. Considering the deformation of the cell shown in Fig. 2 the following relations between elastic properties of foam and bulk material which is used for foam manufacturing were derived:

$$\frac{E_{\mathrm{f}}}{E} \sim \varphi^m, \qquad \frac{\mu_{\mathrm{f}}}{\mu} \sim \varphi^m.$$

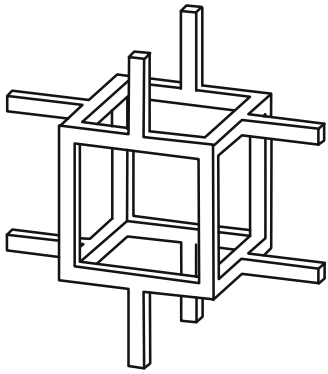

Fig. 2 Simple idealization of open-cell structures: the cubic model [24]

Here φ is the porosity, index f stands for foam properties, $m \approx 2$, $\nu_f \approx 0.3$. So E_f and μ_f are Young's and shear moduli of foam, respectively, while E and μ are their bulk counterparts.

Applying the scaling law (18) or formula (19) we obtain Young's modulus E_n at the nanoscale

$$E_\mathrm{n} = E\left(1 + \frac{l_{in}}{R}\right),$$

where R is the width of struts in Fig. 2 while l_in is an intrinsic length scale parameter given by $l_\mathrm{in} = 2E_S/E$. Repeating the calculations of [24] we modify the dependence of the elastic moduli of a nanofoam on the porosity according to the following rule

$$\frac{E_\mathrm{nf}}{E} \sim \left(1 + \frac{l_{in}}{R}\right)\varphi^m, \qquad \frac{\mu_\mathrm{nf}}{\mu} \sim \left(1 + \frac{l_{in}}{R}\right)\varphi^m,$$

where E_nf and μ_nf are Young's and shear moduli of a nanofoam, respectively. Finally, using formulae (8) we estimate the surface elastic moduli as follows

$$\mu_S \approx \mu_\mathrm{nf} h_\mathrm{f}, \quad E_S \approx E_\mathrm{nf} h_\mathrm{f}, \tag{21}$$

where h_f is the thickness of "foam-like" coating. Having in hands more general formulae for effective properties at the nanoscale such as (17) we obtain another approximations for surface elastic moduli, for example, the relation

$$E_S \approx E^* \varphi^m h_\mathrm{f} \tag{22}$$

can be used. Let us also note that for this coating $\mathbf{v}$ does not coincide with $\mathbf{u}$ as formulated in (4) and compatibility equation (5) should be used. Indeed, here $\mathbf{v}$ corresponds to averaged though the thickness displacement of nanofoam and includes shear deformations as well as thickness changes of the coating.

4 Conclusions

We briefly discuss various models of surface elasticity as well as influence of surface stresses on the effective (apparent) properties of materials. As an example, stiffness of nanoporous rod is presented. We have shown that depending on the model of surface effects the surface elasticity may make a rod stiffer or softer in comparison with the rod without surface stresses. We discuss effective (apparent) properties of solids with imperfect surfaces/interfaces or coatings with inner microstructure such as foam-like coating. The new approximated formulae for surface elastic moduli of this coating are proposed. For further details we refer to [18]. As a result, we conclude that the surface properties play an important role at the nano- and

microscales as well as for materials with great ratio of surface layer volume to the volume of material in the bulk.

References

1. Altenbach H, Eremeyev VA (2011) On the shell theory on the nanoscale with surface stresses. Int J Eng Sci 49(12):1294–1301
2. Altenbach H, Eremeev V, Morozov NF (2010) On equations of the linear theory of shells with surface stresses taken into account. Mech Solids 45(3):331–342
3. Altenbach H, Eremeyev VA, Lebedev LP (2010) On the existence of solution in the linear elasticity with surface stresses. Zeitschrift für Angewandte Mathematik und Mechanik 90(3):231–240
4. Altenbach H, Eremeyev VA, Lebedev LP (2011) On the spectrum and stiffness of an elastic body with surface stresses. Zeitschrift für Angewandte Mathematik und Mechanik 91(9):699–710
5. Altenbach H, Eremeyev VA, Morozov NF (2012) Surface viscoelasticity and effective properties of thin-walled structures at the nanoscale. Int J Eng Sci 59:83–89
6. Arroyo M, Belytschko T (2002) An atomistic-based finite deformation membrane for single layer crystalline films. J Mech Phys Solids 50(9):1941–1977
7. Bažant ZP (2000) Size effect. Int J Solids Struct 37(1):69–80
8. Bhushan B (ed) (2007) Handbook springer of nanotechnology. Springer, Berlin
9. Bhushan B, Jung YC, Koch K (2009) Micro-, nano- and hierarchical structures for superhydrophobicity, self-cleaning and low adhesion. Philos Trans R Soc A 367(1894):1631–1672
10. Craighead HG (2000) Nanoelectromechanical systems. Science 290(5496):1532–1535
11. Cuenot S, Frétigny C, Demoustier-Champagne S, Nysten B (2004) Surface tension effect on the mechanical properties of nanomaterials measured by atomic force microscopy. Phys Rev B 69(16):165410
12. Dastjerdi R, Montazer M (2010) A review on the application of inorganic nano-structured materials in the modification of textiles: focus on anti-microbial properties. Colloids Surf B Biointerfaces 79(1):5–18
13. dell'Isola F, Seppecher P (1997) Edge contact forces and quasi-balanced power. Meccanica 32(1):33–52
14. dell'Isola F, Seppecher P, Madeo A (2012) How contact interactions may depend on the shape of Cauchy cuts in *N*th gradient continua: approach "à la d'Alembert". Zeitschrift für Angewandte Mathematik und Physik 63:1119–1141
15. de Poisson SD (1831) Nouvelle théorie de l'action capillaire. Bachelier Père et Fils, Paris
16. Duan HL, Wang J, Karihaloo BL (2008) Theory of elasticity at the nanoscale. In: Advances in applied mechanics, vol 42. Elsevier, Amsterdam, pp 1–68
17. Ekinci KL, Roukes ML (2005) Nanoelectromechanical systems. Rev Sci Instrum 76(6):061101
18. Eremeyev VA (2015) On effective properties of materials at the nano- and microscales considering surface effects. Acta Mechanica. doi:10.1007/s00707-015-1427-y
19. Eremeyev V, Morozov N (2010) The effective stiffness of a nanoporous rod. Dokl Phys 55(6):279–282
20. Eremeyev VA, Lebedev LP (2013) Existence of weak solutions in elasticity. Math Mech Solids 18(2):204–217
21. Ganesh VA, Raut HK, Nair AS, Ramakrishna S (2011) A review on self-cleaning coatings. J Mater Chem 21(41):16304–16322
22. de Gennes PG (1981) Some effects of long range forces on interfacial phenomena. J Phys Lett 42(16):377–379

23. de Gennes PG, Brochard-Wyart F, Quéré D (2004) Capillarity and wetting phenomena: drops, bubbles, pearls, waves. Springer, New York
24. Gibson LJ, Ashby MF (1997) Cellular solids: structure and properties, 2nd edn. Cambridge solid state science series. Cambridge University Press, Cambridge
25. Gurtin ME, Murdoch AI (1975) A continuum theory of elastic material surfaces. Arch Ration Mech Anal 57(4):291–323
26. Ibach H (1997) The role of surface stress in reconstruction, epitaxial growth and stabilization of mesoscopic structures. Surf Sci Rep 29(5):195–263
27. Javili A, dell'Isola F, Steinmann P (2013) Geometrically nonlinear higher-gradient elasticity with energetic boundaries. J Mech Phys Solids 61(12), 2381–2401
28. Javili A, McBride A, Steinmann P (2012) Thermomechanics of solids with lower-dimensional energetics: On the importance of surface, interface, and curve structures at the nanoscale. A unifying review. Appl Mech Rev 65:010802-1–010802-31
29. Javili A, Steinmann P (2010) A finite element framework for continua with boundary energies. Part II: the three-dimensional case. Comput Methods Appl Mech Eng 199(9–12):755–765
30. Javili A, Steinmann P (2011) A finite element framework for continua with boundary energies. Part III: the thermomechanical case. Comput Methods Appl Mech Eng 200(21):1963–1977
31. Jing GY, Duan HL, Sun XM, Zhang ZS, Xu J, Wang YDLJX, Yu DP (2006) Surface effects on elastic properties of silver nanowires: contact atomic-force microscopy. Phys Rev B 73(23):235409-6
32. Kang X, Zi WW, Xu ZG, Zhang HL (2007) Controlling the micro/nanostructure of self-cleaning polymer coating. Appl Surf Sci 253(22):8830–8834
33. Kim C, Ru C, Schiavone P (2013) A clarification of the role of crack-tip conditions in linear elasticity with surface effects. Math Mech Solids 18(1):59–66
34. Kushch VI, Sevostianov I, Chernobai VS (2014) Effective conductivity of composite with imperfect contact between elliptic fibers and matrix: Maxwell's homogenization scheme. Int J Eng Sci 83:146–161
35. Kushch VI, Chernobai VS, Mishuris GS (2014) Longitudinal shear of a composite with elliptic nanofibers: local stresses and effective stiffness. Int J Eng Sci 84:79–94
36. Laplace PS (1805) Sur l'action capillaire. supplément à la théorie de l'action capillaire. In: Traité de mécanique céleste, vol 4. Supplement 1, Livre X. Gauthier–Villars et fils, Paris, pp 771–777
37. Laplace PS (1806) À la théorie de l'action capillaire. supplément à la théorie de l'action capillaire. In: Traité de mécanique céleste, vol 4. Supplement 2, Livre X. Gauthier–Villars et fils, Paris, pp 909–945
38. Liu K, Jiang L (2012) Bio-inspired self-cleaning surfaces. Ann Rev Mater Res 42:231–263
39. Longley WR, Name RGV (eds) (1928) The collected works of J. Willard Gibbs, Ph.D., LL.D. Thermodynamics, vol I. Longmans, New York
40. Ma X, Liu A, Xu H, Li G, Hu M, Wu G (2008) A large-scale-oriented ZnO rod array grown on a glass substrate via an in situ deposition method and its photoconductivity. Mater Res Bull 43(8):2272–2277
41. Miller RE, Shenoy VB (2000) Size-dependent elastic properties of nanosized structural elements. Nanotechnology 11(3):139
42. Mindlin RD (1965) Second gradient of strain and surface-tension in linear elasticity. Int J Solids Struct 1(4):417–438
43. Mishuris GS, Kuhn G (2001) Asymptotic behaviour of the elastic solution near the tip of a crack situated at a nonideal interface. Zeitschrift für Angewandte Mathematik und Mechanik 81(12):811–826
44. Özgür Ü, Alivov YI, Liu C, Teke A, Reshchikov M, Doğan S, Avrutin V, Cho SJ, Morkoc H (2005) A comprehensive review of ZnO materials and devices. J Appl Phys 98(4):041301
45. Rowlinson JS, Widom B (2003) Molecular theory of capillarity. Dover, New York
46. Rubin M, Benveniste Y (2004) A Cosserat shell model for interphases in elastic media. J Mech Phys Solids 52(5):1023–1052

47. Schiavone P, Ru CQ (2009) Solvability of boundary value problems in a theory of plane-strain elasticity with boundary reinforcement. Int J Eng Sci 47(11):1331–1338
48. Sfyris D, Sfyris G, Galiotis C (2014) Curvature dependent surface energy for a free standing monolayer graphene: some closed form solutions of the non-linear theory. Int J Non Linear Mech 67:186–197
49. Shenoy VB (2005) Atomistic calculations of elastic properties of metallic fcc crystal surfaces. Phys Rev B 71(9):094104
50. Spinelli P, Verschuuren M, Polman A (2012) Broadband omnidirectional antireflection coating based on subwavelength surface Mie resonators. Nat Commun 3:692
51. Steigmann DJ, Ogden RW (1997) Plane deformations of elastic solids with intrinsic boundary elasticity. Proc Roy Soc A 453(1959):853–877
52. Steigmann DJ, Ogden RW (1999) Elastic surface-substrate interactions. Proc R Soc A 455(1982):437–474
53. Tan LK, Kumar MK, An WW, Gao H (2010) Transparent, well-aligned TiO2 nanotube arrays with controllable dimensions on glass substrates for photocatalytic applications. ACS Appl Mater Interfaces 2(2):498–503
54. Wang ZL, Song J (2006) Piezoelectric nanogenerators based on zinc oxide nanowire arrays. Science 312(5771):242–246
55. Wang J, Duan HL, Huang ZP, Karihaloo BL (2006) A scaling law for properties of nano-structured materials. Proc R Soc A 462(2069):1355–1363
56. Wang X, Wang X, Zhou J, Song J, Liu J, Xu N, Wang ZL (2006) Piezoelectric field effect transistor and nanoforce sensor based on a single ZnO nanowire. Nano Lett 6(12):2768–2772
57. Wang J, Huang Z, Duan H, Yu S, Feng X, Wang G, Zhang W, Wang T (2011) Surface stress effect in mechanics of nanostructured materials. Acta Mech Solida Sinica 24:52–82
58. Young T (1805) An essay on the cohesion of fluids. Philos Trans R Soc Lond 95:65–87

Microstructure Sensitive Fatigue Crack Nucleation in Titanium Alloys Using Accelerated Crystal Plasticity FE Simulations

Somnath Ghosh and Pritam Chakraborty

Abstract This chapter investigates microstructure and load sensitive fatigue behavior of Ti-6242 using cyclic crystal plasticity finite element (CPFE) simulations of statistically equivalent image-based microstructures. A wavelet transformation induced multi-time scaling (WATMUS) method (Joseph et al., Comput Methods Appl Mech Eng 199:2177–2194, 2010; Chakraborty et al., Finite Elem Anal Des 47:610–618, 2011; Chakraborty and Ghosh, Int J Numer Methods Eng 93:1425–1454, 2013; Ghosh and Chakraborty, Int J Fatigue 48:231–246, 2013) is used to perform accelerated cyclic CPFE simulations till crack nucleation, otherwise infeasible using conventional time integration schemes. A physically motivated crack nucleation model in terms of crystal plasticity variables (Anahid et al., J Mech Phys Solids 59(10):2157–2176, 2011) is extended in this work to predict nucleation. The dependence of yield strength on the underlying grain orientations and sizes is developed through the introduction of an effective microstructural parameter *Plastic Flow Index* or *PFI*. To determine the effects of the microstructure on crack nucleation, a local microstructural variable is defined in terms of the surface area fraction of soft grains surrounding each hard grain or *SAFSSG*. Simulations with different cyclic load patterns suggest that fatigue crack nucleation in Ti-6242 strongly depends on the dwell cycle hold time at maximum stress.

1 Introduction

The fatigue life and number of cycles to crack nucleation in commercially used titanium alloys, such as Ti-6242, exhibit considerable variation at room temperature due to the heterogeneity of the underlying microstructure [2, 16, 17]. Mechanistic

S. Ghosh (✉)
Department of Civil Engineering, Johns Hopkins University, 3400 N. Charles Street, Baltimore, MD 21218, USA
e-mail: sghosh20@jhu.edu

P. Chakraborty
Idaho National Laboratory, Idaho Falls, ID, USA
e-mail: pritam.chakraborty@inl.gov

P. Trovalusci (ed.), *Materials with Internal Structure*, Springer Tracts in Mechanical Engineering, DOI 10.1007/978-3-319-21494-8_4

approaches, implementing crystal plasticity-based finite element (CPFE) simulations of polycrystalline microstructures, have been pursued in the literature [3, 8, 13–16] to develop fatigue life models. At room temperature, inelastic deformation in Ti-6242 commences predominantly by slip on different slip systems in individual grains of the microstructure [2, 17]. The number of slip systems and their resistance to slip depends on the morphological and crystallographic characteristics. In the *hcp* phase of Ti-6242, the three basal and prismatic $\langle a \rangle$ slip systems have much lower slip resistances in comparison with the 6 $\langle a \rangle$ pyramidal, 12 $\langle c + a \rangle$ first order pyramidal and 6 $\langle c + a \rangle$ second order pyramidal slip systems [6, 11]. Consequently, grains with orientations that induce higher resolved shear stresses on the basal or prismatic systems have more plastic deformation than those activating the pyramidal systems. This material anisotropy due to the large difference in critical resolved shear stress in different slip systems results in large heterogeneity in the plastic deformation in polycrystalline aggregates. It leads to significant load-shedding induced stress concentration at grain boundaries. This is perceived to be the primary driver of microstructure-dependent crack nucleation [2].

The present work uses a size and rate-dependent CPFE model of Ti-6242 developed in [6, 11, 19] to capture this load-shedding induced stress rise in the microstructure leading to crack nucleation. Particularly vulnerable are boundaries between grains having large time-dependent plastic deformation (soft grain) and those with little or no plasticity (hard grain) owing to their orientation with respect to the loading direction. Morphological and crystallographic features of the polycrystalline alloy are statistically represented in the CPFE models using methods developed in [9, 10]. The use of such a statistical description not only reduces the number of grains in the FE simulations but also captures the key features of the microstructure that affect its macroscopic and microscopic response. A non-local crack nucleation model has been developed in [1] to study early crack nucleation in polycrystalline Ti-alloys under dwell fatigue cyclic loading. The crack nucleation criterion is functionally dependent on stress concentration and dislocation pile-up at grain boundaries. These variables are obtained from CPFEM simulations. A combination of CPFE simulations and ultrasonic testing of dwell fatigue Ti-6242 samples has been used in [1] for calibrating and validating the nucleation model. This model is adopted in the present work to study microstructure and load-dependent crack nucleation in Ti-6242.

Although CPFE simulations accurately capture the deformation behavior of polycrystalline alloys, they require very small time steps when conventional time integration schemes are used to march forward in time. In cyclic loading and deformation, small time steps in every cycle of the loading process leads to prohibitively large computations, when analysis is performed for a large number of cycles to fatigue failure. The *wavelet transformation induced multi-time scaling* or WATMUS method, developed in [4, 5, 7, 12], has shown significant computational benefits in rapidly traversing a high number of cycles. This chapter discusses the effects of microstructure and cyclic loading conditions on grain-level crack nucleation.

The WATMUS method based cyclic CPFE simulations of polycrystalline Ti-6242 microstructures are used to accomplish this mechanistic approach. A detailed numerical study of the different factors affecting fatigue crack nucleation in Ti-6242 is executed in Sect. 5. In Sect. 5.1, relations between crystallographic features and cycles to crack nucleation are developed. The dependence on the number of cycles to crack nucleation on characteristics of the applied load is studied in Sect. 5.2.

2 Rate-Dependent Crystal Plasticity and Nonlocal Crack Evolution Models for Ti-6242

The rate and size-dependent crystal plasticity constitutive laws governing deformation in polycrystalline, bi-phasic Ti-6242 alloys have been detailed in [6, 11, 19]. A power law model is used to determine the slip-rate on different slip systems as:

$$\dot{\gamma^{\alpha}} = \dot{a} \left| \frac{\tau^{\alpha} - \chi^{\alpha}}{g^{\alpha}} \right|^{\frac{1}{m}} sign(\tau^{\alpha} - \chi^{\alpha}) \tag{1}$$

where $\dot{a}$ is a reference slip rate, τ^{α} is the resolved shear stress on the slip system, χ^{α} is a back stress, g^{α} is the slip system resistance, and m is the power law exponent. The resolved shear stress on a slip system is obtained from the relation

$$\tau^{\alpha} = \mathbf{F^{eT}F^{e}T^{*}} : \mathbf{S_0^{\alpha}} \tag{2}$$

where $\mathbf{T^{*}}$ is the second Piola–Kirchoff (PK2) stress. The back stress evolution on a slip system follows the law:

$$\dot{\chi^{\alpha}} = c\dot{\gamma^{\alpha}} - d\chi^{\alpha} \left| \dot{\gamma^{\alpha}} \right| \tag{3}$$

where c and d are the direct hardening and dynamic recovery coefficients, respectively. The evolution of slip system deformation resistance is controlled by two types of dislocations, viz., statistically stored dislocations (SSDs) and geometrically necessary dislocations (GNDs) [1]. The corresponding deformation resistance rate is expressed as:

$$\dot{g}^{\alpha} = \sum_{\beta} h^{\alpha\beta} |\dot{\gamma}^{\beta}| + \frac{k_0 \hat{\alpha}^2 G^2 b}{2(g^{\alpha} - g_0^{\alpha})} \sum_{\beta} \lambda^{\beta} |\dot{\gamma}^{\beta}| \tag{4}$$

The modulus $h^{\alpha\beta} = q^{\alpha\beta} h^{\beta}$ (no sum on β) is the strain hardening rate due to self and latent hardening on the α-th slip system by slip on the β-th slip system, respectively. Here, h^{β} is the self hardening coefficient and $q^{\alpha\beta}$ is a matrix describing latent hardening. Different self hardening relationships are used for modeling the α

and β phases [6]. The evolution of self hardening for the α phase is modeled as:

$$h^{\alpha} = h_0^{\alpha} \left| 1 - \frac{g^{\alpha}}{g_s^{\alpha}} \right|^r sign\left(1 - \frac{g^{\alpha}}{g_s^{\alpha}} \right) \quad , \quad g_s^{\alpha} = \tilde{g} \left| \frac{\dot{\gamma^{\alpha}}}{\dot{a}} \right|^c \tag{5}$$

where h_0^{α} is a reference self hardening parameter and g_s^{α} is the saturation value of slip system resistance. Self hardening rate of the β phase is given as:

$$h^{\alpha} = h_s^{\alpha} + sech^2 \left[\frac{h_0^{\alpha} - h_s^{\alpha}}{\tau_s^{\alpha} - \tau_0^{\beta}} \gamma^{acc} \right] \left(h_0^{\alpha} - h_s^{\alpha} \right) \quad \text{where} \quad \gamma^{acc} = \int_0^t \sum_{\alpha} \left| \dot{\gamma^{\alpha}} \right| dt \tag{6}$$

h_0^{α} and h_s^{α} are the initial and the asymptotic hardening rates, τ_s^{α} represents the saturation value of shear stress when $h_s^{\alpha} = 0$, and γ^{acc} is the accumulated plastic slip. The second term in Eq. (4) accounts for the effect of GNDs on work hardening. Here, k_0 is a dimensionless material constant, G is the elastic shear modulus, b is the Burgers vector, g_0^{α} is the initial deformation resistance, and $\hat{\alpha}$ is a non-dimensional constant. $\hat{\alpha}$ is taken to be $\frac{1}{3}$ in [1]. λ^{β} is a measure of slip plane lattice incompatibility, which can be expressed for each slip system as a function of slip plane normal $\mathbf{n}^{\beta}$ and an incompatibility tensor Λ as:

$$\lambda^{\beta} = \Lambda \mathbf{n}^{\beta} : \Lambda \mathbf{n}^{\beta})^{\frac{1}{2}} \tag{7}$$

The dislocation density tensor Λ can be expressed using the curl of plastic deformation gradient tensor $\mathbf{F}^P$.

The effect of grain size and lath thickness on the slip system resistance is also considered in the crystal plasticity model in [19]. A Hall Petch type relation is used to modify the initial slip system resistances $g^{\alpha}(t = 0)$ to capture size effect according to the relation:

$$g^{\alpha}(t = 0) = g_0^{\alpha} + \frac{K^{\alpha}}{\sqrt{D^{\alpha}}} \tag{8}$$

where g_0^{α} is the homogeneous slip system resistance, D^{α} is a characteristic length parameter that corresponds to the mean-free path of the dislocations in a grain. For globular α grains, the transmission of dislocations to adjacent grains is resisted by grain boundaries and hence grain diameter is considered as characteristic length in Eq. (8). For transformed β colonies, dislocation motions can be impeded either by the colony boundary or lath boundary depending on the Burger's orientation relation between α and β laths [6, 11]. Hence either colony size or lath thickness is used for D^{α} in Eq. (8) for slip system resistances of the transformed β colonies. K^{α} is a constant that depends on the Poisson's ratio, shear modulus, Burgers vector, and barrier strength.

A crack nucleation model, developed in [1], is used in this work to model grain-level nucleation in a polycrystalline ensemble. Experimentally extracted crystallographic features of grains at failure sites suggest that regions of hard grains surrounded by soft grains are susceptible to initiate a crack. Contiguous hard grains with less-favorably oriented for $< a >$-type slip ($< c >$-axis parallel to the deformation direction), experience large local stress concentrations, especially near the shared grain boundary. This is a consequence of compatible, large elastic strains in the hard grains near the shared boundary. The phenomenon of rising stress-concentration with evolving creep strains in dwell cycles has been called load shedding [1, 11]. The hard grain crack nucleation criterion, ahead of dislocation pile-ups in adjacent soft grain has been derived to be [1]:

$$T_{eff} = \sqrt{< T_n >^2 + \beta T_t^2} \geq \frac{K_c}{\sqrt{\pi c}} \tag{9}$$

or equivalently

$$R = T_{eff} \cdot \sqrt{c} \geq R_c \,, \qquad \text{where } R_c = \frac{K_c}{\sqrt{\pi}} \tag{10}$$

In Eqs. (9) and (10), T_{eff} is an effective traction on the hard grain basal plane for mixed mode crack nucleation. It is expressed in terms of the stress component normal to the crack surface $T_n = \sigma_{ij} n_i^b n_j^b$ and the tangential stress component $T_t = \|\mathbf{T} - T_n \mathbf{n}^b\|$. Here $\mathbf{T}$ is the stress vector on the crack surface, σ_{ij} is the Cauchy stress tensor, and n_i^b are the components of unit outward normal to the crack surface. Only the tensile normal stress $< T_n >$, represented by the McCauley bracket $<>$, contributes to the effective stress responsible for crack opening. K_c is the critical mixed-mode stress intensity factor and $\beta \approx K_{nc}/K_{tc}$ is a shear stress factor used to assign different weights to the normal and shear traction components for mixed-mode. A value of $\beta = 0.7071$ is used for Ti-64 alloys in this study. c is the length of a wedge micro-defect or crack on the basal plane of the hard grain caused by dislocation pile-up in the adjacent soft grain. The micro-crack length c in Eq. (10) is obtained from the relation proposed in [18] as:

$$c = \frac{G}{8\pi(1-\nu)\gamma_s} B^2 \tag{11}$$

where B is the crack opening displacement, G is the shear modulus, ν is the Poisson's ratio, and γ_s is the surface energy. The crack opening displacement $B = \|\mathbf{B}\|$ is a non-local variable. The critical crack nucleation parameter R_c in Eq. (10) is a material property, which is calibrated from experiments.

3 Wavelet Transformation Based Multi-time Scale Method for Accelerated Cyclic CPFEM Simulations

Fatigue life predictions in polycrystalline metallic microstructures involve cyclic crystal plasticity FEM simulations till crack nucleation. Depending on the microstructure and load profile, this may involve simulations for large number of cycles. Such simulations may become computationally prohibitive using conventional time integration schemes in FEM codes. In [4, 5, 7, 12], a wavelet transformation based multi-time scale or WATMUS method has been developed to reduce the problem to a set of low frequency, coarse time-scale governing equations. In the WATMUS scheme, any time-dependent variable $v^{\zeta}(t)$ is expressed as:

$$v^{\zeta}(t) = v(N,\tau) = \sum_{k=1}^{n} v_k(N)\psi_k(\tau) \quad \forall \quad \tau \in [0,T] \tag{12}$$

The superscript ζ corresponds to the dependence of the variable on the two time-scales, which for this problem correspond to a cycle scale N and an intra-cycle fine time-scale τ. $\psi_k(\tau)$ are wavelet basis functions that capture the high frequency response within each cycle, n is the number of basis functions required for accurate representation of the waveform. The finite support of the wavelet basis functions eliminates spurious oscillations that may arise with truncation of terms in infinitely supported basis functions such as the spectral basis functions. $v_k(N)$ are the associated coefficients that evolve monotonically in the cycle (N)-scale. Using orthogonality property, they may be expressed as:

$$v_k(N) = \frac{1}{T}\int_0^T v(N,\tau)\psi_k(\tau)d\tau \tag{13}$$

where T is the time period of the applied load. Wavelet transformation facilitates numerical integration of the CPFEM equations in the cycle-scale traversing several cycles in each step. This leads to significant efficiency gain.

The oscillatory stress response $\sigma_{ji}(N,\tau)$ depends on the oscillatory deformation gradient $F_{ij}(N,\tau)$ and internal variables $y_m(N,\tau)$. $F_{ij}(N,\tau)$ at each integration point in any cycle is obtained from the coefficients of nodal displacements $C^{\alpha}_{i,k}(N)$ using the relation:

$$F_{ij}(N,\tau) = \delta_{ij} + \frac{\partial P^{\alpha}}{\partial X_j}\sum_{k=1}^{n} C^{\alpha}_{i,k}(N)\psi_k(\tau) \tag{14}$$

In crystal plasticity, the evolution of internal variables is governed by first order rate equations of the type

$$\dot{y}^{\zeta}_m(t) = f_m(y^{\zeta}_m, F^{\zeta}_{ij}, t) \tag{15}$$

Here y_m^{ζ} are internal variables represented in a single time-scale, t and f_m are non-linear functions. The oscillatory evolution of the dual-scale variable $y_m(N, \tau)$ in any cycle may be obtained from the fine-scale time integration as:

$$y_m(N, \tau) = y_{m0}(N) + \int_0^{\tau} f_m(y_m, F_{ij}, N, \tau) d\tau \tag{16}$$

where $y_{m0}(N) = y_m(N, \tau = 0)$ are values of internal variables at the beginning of a cycle. This forms a new cycle-scale variable, corresponding to the initial values of internal variables y_{m0}, which have a monotonic evolution in the cycle-scale. Cycle-scale rate equations are numerically defined for y_{m0} as [12]:

$$\frac{\partial y_{m0}}{\partial N} = y_{m0}(N+1) - y_{m0}(N) = y_m(N, T) - y_{m0}(N) \tag{17}$$

where

$$y_m(N, T) = y_{m0}(N) + \int_0^{T} f_m(y_m, F_{ij}, N, \tau) d\tau \tag{18}$$

Since f_m are non-linear functions, numerical time-integration using the backward Euler scheme is performed on Eq. (18). The cycle-scale internal variables are integrated using a second order backward difference formula, expressed as:

$$\begin{aligned} & y_{m0}(N) = \beta_1 y_{m0}(N - \Delta N) - \beta_2 y_{m0}(N - \Delta N - \Delta N_p) + \beta_3 \frac{\partial y_{m0}}{\partial N}\Big|_N \Delta N \\ & \text{where} \quad \beta_1 = \frac{(r+1)^2}{(r+1)^2 - 1} \quad \beta_2 = \frac{1}{(r+1)^2 - 1} \quad \beta_3 = \frac{(r+1)^2 - (r+1)}{(r+1)^2 - 1} \\ & \text{and} \quad r = \frac{\Delta N_p}{\Delta N} \end{aligned} \tag{19}$$

The Newton–Raphson iterative scheme is used to solve Eq. (19).

The accuracy of the WATMUS method is demonstrated by comparing the evolution of crystal plasticity variables obtained from (1) single time-scale, and (2) WATMUS method-enhanced dual time-scale simulations of a statistically equivalent virtual polycrystalline Ti-6242 microstructure [9, 10]. In Fig. 1, the microstructure is subjected to a triangular cyclic load on the y-face with a maximum and minimum normal traction of 869 MPa and 0 MPa respectively, and a time period of 2 s. The WATMUS method-enhanced CPFEM simulation is performed for 300,000 cycles and the evolutionary variables, e.g. set of wavelet coefficients of nodal displacements $C_{i,k}^{\alpha}$ and the history of coarse scale internal variables $\mathbf{y}_0^{\alpha/\beta} = \left\{F_{ij,0}^{p}, g_0^{\alpha}, \chi_0^{\alpha}\right\}$ are compared with a single time-scale simulation. The single time-scale simulation

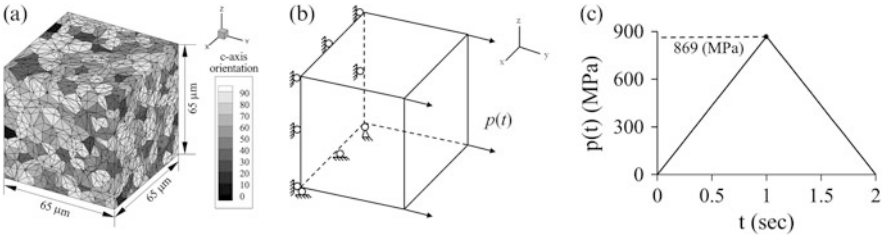

Fig. 1 FE model of a polycrystalline microstructure and loading conditions to demonstrate the accuracy and efficiency of the WATMUS method: (**a**) microstructure with $< c >$-axis orientation and mesh, (**b**) boundary conditions, and (**c**) cyclic loading profile

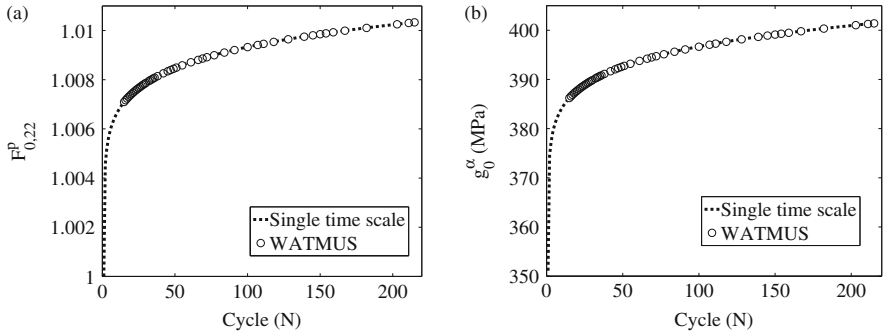

Fig. 2 Comparison of the evolution of the cycle-scale with averaged single time-scale internal variables at an integration point in the FE model of the polycrystalline microstructure for: (**a**) $F^p_{0,22}$, (**b**) g^α_0

suffers from a large computational overhead, and the simulation is performed for 215 cycles only. A comparison of the evolution of coarse internal variables at an integration point in the microstructure is shown in Fig. 2.

The distribution of the loading direction stress σ_{22} along a specified material line in the microstructure, as obtained by the WATMUS and single time-scale simulations is compared in the Fig. 3. These comparisons conclusively show that the WATMUS method is able to capture the evolution of the local microstructural variables very accurately. Finally to demonstrate the power of the WATMUS method in traversing a large number of cycles, the evolution of plastic deformation gradient $F^p_{0,22}$ with advancing cycles are shown in Fig. 4 for up to 300,000 cycles. To evaluate the computational efficiency, the CPU time to perform 215 cycles for the single time-scale CPFEM simulation is extrapolated to 300,000 cycles and compared with the CPU time taken to perform 300,000 cycles of WATMUS simulation. A computational speedup of $\sim$100 times is obtained for this problem.

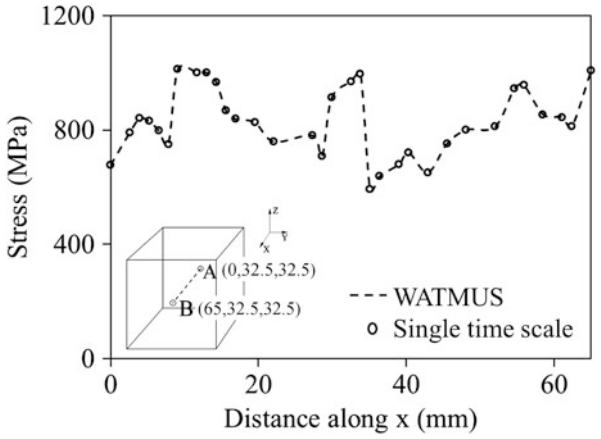

Fig. 3 Comparison of distribution of stress σ_{22} along a material line in the microstructure at $N = 211$ and $\tau = 1$ s, by the WATMUS and single time-scale CPFEM simulations for σ_{22}

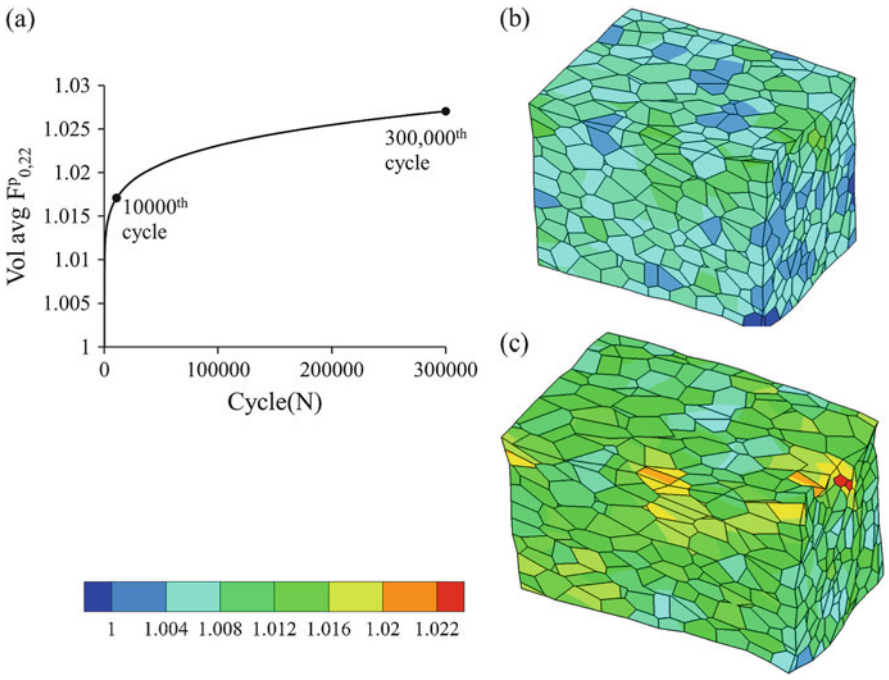

Fig. 4 Evolution of $F^p_{0,22}$ with cycles by WATMUS-based CPFEM simulation: (**a**) volume averaged $F^p_{0,22}$, (**b**) distribution of $F^p_{0,22}$ at the 10,000th cycle, and (**c**) distribution of $F^p_{0,22}$ at the 300,000th cycle

3.1 WATMUS Method Based Dwell Fatigue Simulation of Ti-6242 Microstructure

The ability of the WATMUS method in handling large time periods is demonstrated through a dwell fatigue simulation for the polycrystalline microstructure shown in Fig. 1. A schematic of the dwell load with 2 min hold and the corresponding segments are shown in Fig. 5a, b, respectively.

The cycle-scale evolution of $F^p_{0,22}$ and g^α_0 for a slip system at an integration point in the microstructure by the WATMUS method-enhanced CPFEM simulation is shown in Fig. 6. The evolution of σ_{22} along a material line in the microstructure is evaluated for the cycles 21 and 500, at $\tau = 121$ s, and is depicted in Fig. 7. Large stresses develop in the hard grains adjacent to soft grains due to anisotropy, leading to orientation dependent rate of plastic deformation and load-shedding. The stress peak rises with advancing cycles of the load, thus enhancing the probability

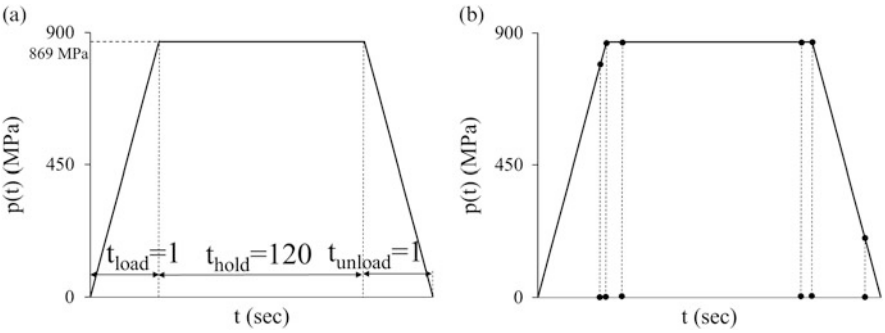

Fig. 5 Schematic of cyclic dwell loading: (**a**) dwell load profile applied on *y*-face of the polycrystalline microstructure (**b**) segments with different maximum resolution

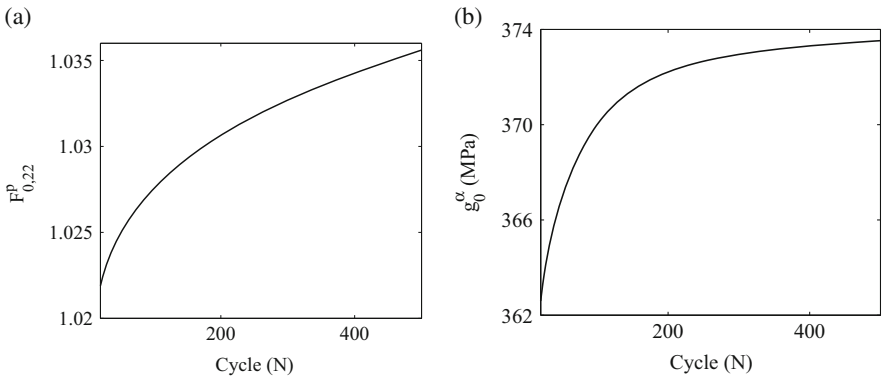

Fig. 6 Evolution of cycle-scale internal variables at an integration point in the microstructure: (**a**) $F^p_{0,22}$ (**b**) one of the slip system resistances g^α_0

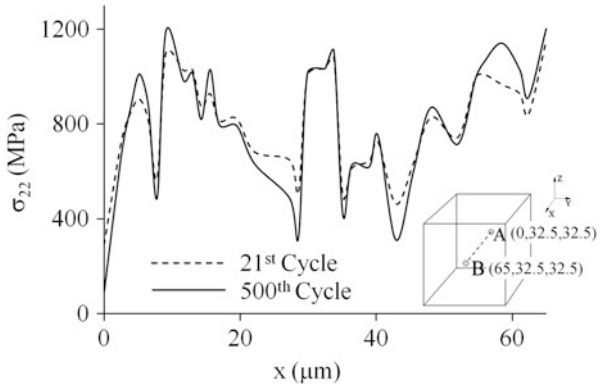

Fig. 7 Evolution of loading direction stress component σ_{22} along a material line in the microstructure evaluated at cycles N = 21 and N = 500 and $\tau = 121$ s

of crack nucleation in these hard grains. The WATMUS method-enhanced CPFE simulations are used in conjunction with the crack nucleation model to study the fatigue nucleation behavior of Ti-alloys.

4 Calibration and Validation of Critical Crack Nucleation Parameter R_c

The critical crack nucleation parameter R_c should be calibrated prior to conducting crack nucleation sensitivity analyses using CPFE simulations. Validation studies are performed using two different specimens of the Ti-6242 alloy, subject to dwell fatigue load with a hold time of 2 min, and loading and unloading time of 1 s each. The maximum stress in a loading cycle is 869 MPa, which is 95 % of the yield strength, while the minimum stress is 0 MPa. Subsurface crack propagation has been monitored by using micro-radiographic images from interrupted experiments in [20]. From dwell fatigue experiments, it has been observed that crack nucleation occurs at 80–85 % of the total number of cycles to failure N_f. The overall yield strengths of the specimens 1 and 2 in the loading direction are evaluated from constant strain rate simulations prior to dwell fatigue simulations. Corresponding to 0.2 % elastic strain, an yield strength value of ∼915 MPa is assessed for these specimens.

The WATMUS method-enhanced CPFEM simulations are performed under dwell loading for validating the crack nucleation model. Consistent with experimental procedures, a maximum applied stress of 869 MPa, which corresponds to 95 % of the yield stress, and a stress ratio $\sigma_R = \sigma_{min}/\sigma_{max} = 0$ is applied. Following the procedure described in [1], the crack nucleation parameter R_α at every node on grain interfaces is evaluated at $\tau = 121$ s in each cycle for the 2-min dwell. Experimental

results of specimen 1, which fails after 352 cycles, are used to calibrate R_c. From the conclusions of experimental studies in [20], the minimum and maximum number of cycles to crack nucleation for the specimen 1 is estimated as $N_{c(80\,\%)} = 282$ (80 % of N_f) and $N_{c(85\,\%)} = 300$ (85 % of N_f). The evolution of the nodal R_α at the grain boundaries is obtained from CPFE simulations of specimen 1. The maximum R_α values at $N_{c(80\,\%)} = 282$ and $N_{c(80\,\%)} = 300$ are considered as the lower and upper limits of R_c, respectively.

$$\begin{aligned} R_{c(80\,\%)} &= \max_{\alpha} R_\alpha (N = 282, \tau = 121\,\text{s}) = 6.54\,\text{MPa}\sqrt{\mu m} \\ R_{c(85\,\%)} &= \max_{\alpha} R_\alpha (N = 300, \tau = 121\,\text{s}) = 6.80\,\text{MPa}\sqrt{\mu m} \end{aligned} \tag{20}$$

Experimental results of specimen 2 are used to validate the crack nucleation model for the calibrated R_c value. The number of cycles to crack nucleation from interrupted dwell fatigue experiments is 550 cycles. From the CPFE simulations, the number of cycles to crack nucleation is predicted for 80 % and 85 %, respectively of the total life as:

$$\begin{aligned} N_{c(80\,\%)} : \max_{\alpha} R_\alpha (N, \tau = 121\,\text{s}) = R_{c(80\,\%)} \Rightarrow N_{c(80\,\%)} = 620 \\ N_{c(85\,\%)} : \max_{\alpha} R_\alpha (N, \tau = 121\,\text{s}) = R_{c(85\,\%)} \Rightarrow N_{c(85\,\%)} = 694 \end{aligned} \tag{21}$$

The evolution of maximum R_α at a grain boundary node with crack nucleation is shown in Fig. 8.

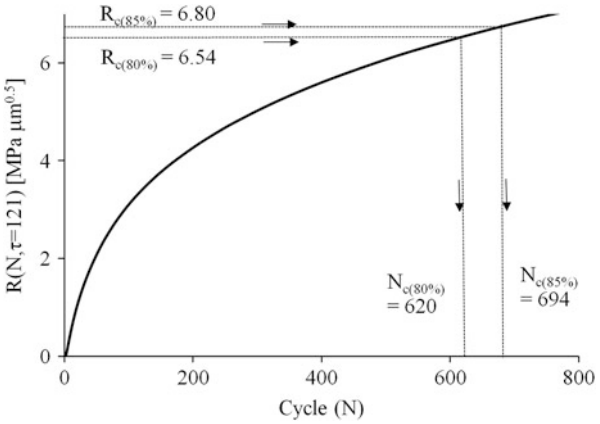

Fig. 8 Evolution of maximum R_α with N in specimen 2 at a crack nucleation site under dwell cyclic loading, evaluated at $\tau = 121$ s

Table 1 Comparison of the number of cycles to crack nucleation predicted by the model with experimental results for specimen 2

Cycles to crack nucleation (Experiment)	Cycles to crack nucleation (Predicted)		% Relative error	
	80 % of life	85 % of life	80 % of life	85 % of life
550	620	694	12.7	25.4

Table 2 Crystallographic features of the crack nucleation site predicted by the model and experiments for specimens 1 and 2

Microstructural parameters	Experiments	Specimen 1	Specimen 2
θ_c	0–30°	38.5°	25.2°
Prismatic Schmid factor	0.0–0.1	0.17	0.09
Basal Schmid factor	0.3–0.45	0.48	0.38

The predicted number of cycles to crack nucleation for specimen 2 along with the associated error are summarized in Table 1. The crystallographic features of the predicted crack nucleation site for both the specimens are compared with experimentally observed characteristics in Table 2.

5 Influence of Microstructural and Loading Characteristics on Crack Nucleation in Ti-6242

In this section, room temperature crack nucleation in Ti-6242 is related to microstructural features and loading profile under cyclic loading using the WATMUS method-enhanced CPFE simulations. The yield strength of a polycrystalline alloy depends on the plastic flow behavior of the individual grains. Room temperature plastic deformation in Ti-6242 is primarily due to slip in individual grains. Consequently, factors affecting initiation of slip are used to study the sensitivity of yield strength to the underlying microstructure. Plastic deformation in a grain of a given size and orientation with the loading direction, is represented by a parameter termed as the *Plastic Flow Index* or *PFI*, defined as:

$$PFI = \max_{\alpha} \left(\frac{\left| \cos \theta_n^{\alpha} \cos \theta_m^{\alpha} \right|}{0.5} \right) \left(\frac{g_0^{prismatic}}{g^{\alpha}} \right) \tag{22}$$

where θ_n^{α} and θ_m^{α} are the angles made by the slip plane normals and the corresponding slip directions with the loading direction. $g_0^{prismatic}$ is the slip system resistance of the prismatic $\langle a \rangle$ slip system in Eq. (8). The calibrated value of g_0 in [19] is the smallest for the prismatic $\langle a \rangle$ slip system. Hence, it is considered as a reference in Eq. (22) since it implies least resistance to slip. A crystal oriented with the maximum Schmid factor 0.5 along the prismatic $\langle a \rangle$ slip system has the minimum

yield strength and maximum plastic flow, compared to any other grain orientation. Thus the *PFI* is considered to provide an effective measure of plastic flow in the grain. It also depends on the loading direction or Schmid factor of individual slip systems in the grain. The *PFI* has characteristics similar to the Taylor factor in [17] in that it uses a measure of the slip rate to determine the degree of plasticity in each grain of the polycrystalline microstructure. However there are also some distinct differences, viz.

- The maximum ratio from all the slip systems in a grain is considered in PFI.
- The microstructure with maximum slip activity (single crystal with SF = 0.5 on prismatic slip system) is considered to obtain the relative measure PFI.
- The distribution of PFI instead of a volume average is used to obtain a relative measure of yield strength for polycrystalline alloys.

For a grain, the value of *PFI* can vary between 0 and 1, i.e., $0 \leq PFI < 1$. A higher value of *PFI*, i.e., $PFI \rightarrow 1$ indicates higher plastic flow and lower strength for the grain. The yield strengths of specimens 1 and 2 in the *y*-direction are related to the underlying grain sizes and orientations by considering the *PFI* distribution of individual grains in the microstructure. The distributions are compared in Fig. 9. The distributions show that both specimens 1 and 2 have similar high volume fractions (VF ≈ 0.2) in the range $0.7 \leq PFI < 0.8$. The *PFI* distribution provides an effective metric in relating the yield strength to the underlying grain sizes and orientations. To validate this postulate, a third virtual microstructure (specimen 3) is constructed by randomly assigning orientations to grains in the FE model of Fig. 1a. The orientations are chosen from the set of orientations in specimen 1. The grain sizes of specimen 3 are the same as for specimen 1. The *PFI* distribution for specimen 3 is compared with those for specimens 1 and 2 in Fig. 9. This has a lower volume fraction in the range $0.7 \leq PFI < 0.8$. Correspondingly, specimen 3 is

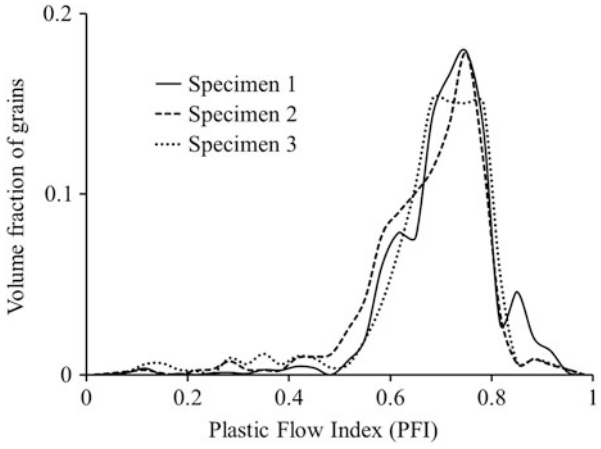

Fig. 9 Plastic flow index (*PFI*) distribution for specimens 1–3

expected to have a higher yield strength. This is corroborated by constant strain-rate CPFE simulation results, for which the yield strength is 940 MPa.

5.1 Sensitivity of Crack Nucleation to Microstructural Features

Crystallographic features at the crack nucleation site, obtained from fatigue experiments on Ti-6242 in [17] are reported in Table 2. This data can be used to capture the effect of local variations in microstructural features on the number of cycles to fatigue crack nucleation. Grains are distinguished as hard or soft, based on their $< c >$-axis orientation with respect to the loading axis. Orientations between 0° and 30° ensures that the maximum prismatic and basal $< a >$ Schmid factors are in the range 0.0–0.1 and 0.3–0.45, respectively.

The $< c >$-axis orientation at the crack nucleation site for specimen 1 is predicted to be 38.5° by the crack nucleation model. Consequently, a $< c >$-axis orientation range of 0–40° is used here to identify hard and soft grains. A grain is assumed to be hard when its $< c >$-axis orientation with respect to the loading direction is less than 40°. Since hard grains surrounded by soft grains are more susceptible to crack nucleation, the surface area fraction of soft grains surrounding each hard grain or *SAFSSG* is examined as a potential metric. The distribution of *SAFSSG* for specimens 1–3 is shown in Fig. 10.

The number of cycles to crack nucleation depends on the extreme values of the distribution in Fig. 10. This implies that a microstructure with a higher volume fraction of hard grains with high *SAFSSG* is likely to nucleate cracks earlier. Figure 10 illustrates that specimen 2 should have the longest nucleation life and specimen 3 should have the shortest life. This observation is supported by dwell

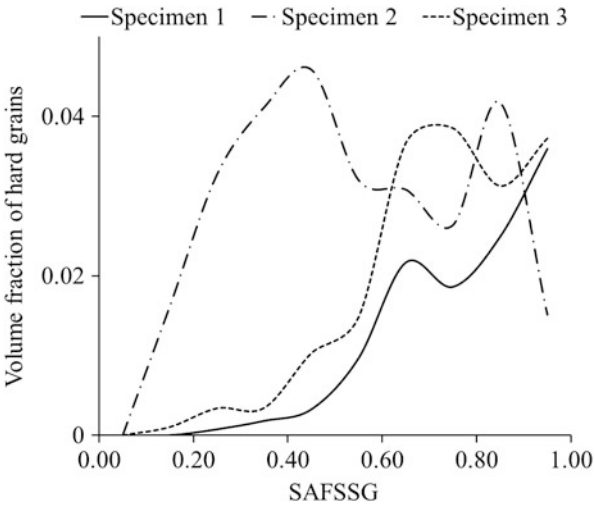

Fig. 10 Volume fraction distribution of hard grains and corresponding surface area fractions of surrounding soft grains (*SAFSSG*) in specimens 1–3

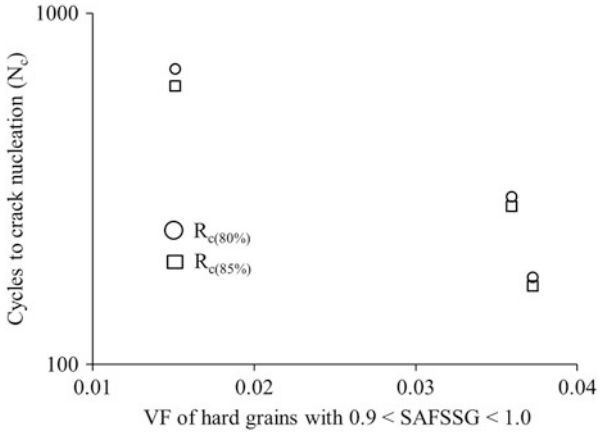

Fig. 11 Comparison of number of cycles to crack nucleation for different volume fraction (VF) of hard grains with surface area fraction of surrounding soft grains (SAFSSG) between 0.9 and 1

fatigue simulations and experiments for specimens 1 and 2. A comparison of cycles to crack nucleation for different volume fraction (VF) of hard grains with increasing surface area fraction *SAFSSG* between 0.9 and 1 is shown in Fig. 11.

5.2 *Sensitivity of Crack Nucleation to Characteristics of Applied Loading*

Specimen 3 is subjected to four different loading cases for this sensitivity study, viz.:

- Case A: $\sigma_{max} = 894\,\text{MPa}$, $\sigma_r = 0$, $T_{load} = T_{unload} = 1\,\text{s}$ and $T_{hold} = 120\,\text{s}$
- Case B: $\sigma_{max} = 847\,\text{MPa}$, $\sigma_r = 0$, $T_{load} = T_{unload} = 1\,\text{s}$ and $T_{hold} = 120\,\text{s}$
- Case C: $\sigma_{max} = 894\,\text{MPa}$, $\sigma_r = 0$, $T_{load} = T_{unload} = 61\,\text{s}$ and $T_{hold} = 0\,\text{s}$
- Case D: $\sigma_{max} = 894\,\text{MPa}$, $\sigma_r = 0$, $T_{load} = T_{unload} = 1\,\text{s}$ and $T_{hold} = 0\,\text{s}$

The maximum applied stress σ_{max} is 95 % of yield strength for cases A, C, and D, while it is 90 % for case B. Dwell load with 2 min hold is applied in cases A and B. Triangular loading with time periods $T = 122\,\text{s}$ and $T = 2\,\text{s}$ are respectively applied for cases C and D. The WATMUS method is used to perform cyclic CPFEM simulations and the crack nucleation parameter R_α is evaluated at nodes on the grain boundaries. Within a cycle, R_α is evaluated at the beginning of unloading. This corresponds to $\tau = 121\,\text{s}$ for cases A and B, $\tau = 61\,\text{s}$ for case C and $\tau = 1\,\text{s}$ for case D. The evolution of R_α at the node, where crack nucleation is predicted, is shown in Fig. 12. The predicted number of cycles to crack nucleation based on the calibrated R_c values are summarized in Table 3. The microstructure has a shorter life when subjected to dwell loading cases A and B in comparison with normal cyclic

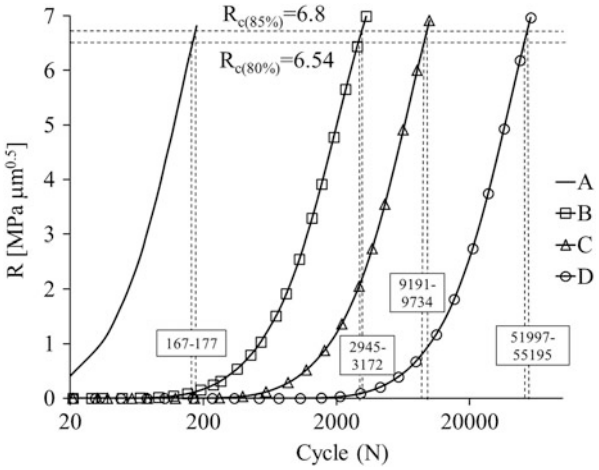

Fig. 12 Evolution of R_α with cycles at the predicted crack nucleation site for specimen 3, under four different fatigue loading cases described in Sect. 5.2

Table 3 Comparison of number of cycles to crack nucleation in specimen 3 for different cyclic loadings

	Cycles to crack nucleation	
Case no.	80 % of life	85 % of life
A	167	177
B	2945	3172
C	9191	9734
D	51,997	55,195

loading cases C and D. For the latter cases, a decrease in loading frequency reduces life. The number of cycles to crack nucleation for dwell case A and normal fatigue case D at 95 % of yield strength shows the same trend as observed experimentally in [2, 17].

In every dwell cycle, the microstructure is held at the maximum stress level for a longer period of time than in the normal cyclic loading. This results in a larger inelastic deformation and strain accumulation in the microstructure within each dwell cycle. Stress concentration and micro-crack growth at the hard soft grain interface are more pronounced in every cycle for the dwell loading. This explains the reduction in life to crack nucleation under dwell load of case A when compared to normal cyclic load of case D. A reduction in the maximum applied stress in dwell loading for case B reduces the cyclic strain accumulation and the accompanying stress rise. Consequently, it shows a longer life than case A. When the frequency of normal cyclic loading is reduced in case C, ramping to the maximum applied stress in every cycle happens slowly. This results in increased plastic strain accumulation and stress rise, compared to the higher frequency case D. Thus, frequency reduction for the same maximum stress level decreases the nucleation life of the microstructure.

The number of cycles to crack nucleation for specimen 3 for different hold, loading, and unloading times in dwell cyclic loading are also compared. The applied stress levels are kept at $\sigma_{max} = 894\,\text{MPa}$ and $\sigma_{min} = 0\,\text{MPa}$, while the total period of loading is $T = 122\,\text{s}$. The WATMUS based CPFEM simulations are performed for three different cases, viz.:

- Case E: $T_{load} = T_{unload} = 16\,\text{s}$ and $T_{hold} = 90\,\text{s}$
- Case F: $T_{load} = T_{unload} = 31\,\text{s}$ and $T_{hold} = 60\,\text{s}$
- Case G: $T_{load} = T_{unload} = 46\,\text{s}$ and $T_{hold} = 30\,\text{s}$

The number of cycles to nucleate a crack is evaluated and the nodal R_α at the predicted crack nucleation site is evaluated at $\tau = 106\,\text{s}$, 91 s, and 76 s, respectively within the cyclic increments. The number of cycles to crack nucleation for cases E, F and G are summarized in Table 4. A comparison of the number of cycles to crack nucleation for different hold times is shown in Fig. 13.

Table 4 Number of cycles to crack nucleation in specimen 3 for dwell cyclic load with different hold times

	Cycles to crack nucleation	
Case no.	80 % of life	85% of life
E	247	261
F	364	394
G	690	755

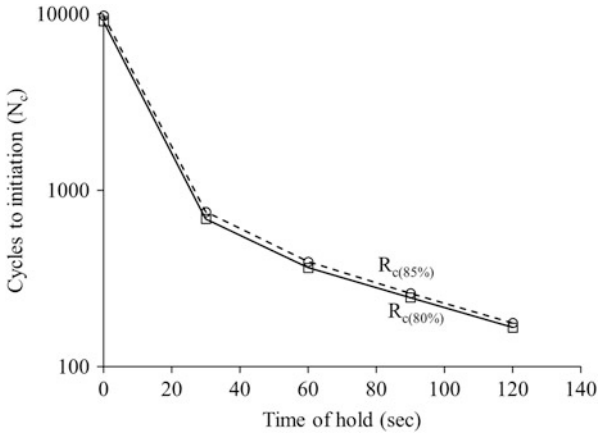

Fig. 13 Number of cycles to crack nucleation in specimen 3 for different hold times

6 Conclusion

This chapter investigates the effects of critical morphological and crystallographic characteristics of the microstructure and loading conditions on grain-level crack nucleation in polycrystalline Ti-6242 microstructures. Crystal plasticity FEM simulations of statistically equivalent microstructures, in conjunction with a physically motivated crack nucleation model, are used to provide a mechanistic approach towards predicting this behavior. A non-local crack nucleation model in terms of the local stresses near the hard grain boundary and the piled-up dislocations in the adjacent soft grain is implemented to predict nucleation in the hard grain. Crack nucleates when a parameter R at any node on hard soft grain interfaces exceeds a critical value R_c for the material. A necessary ingredient of cyclic simulations is the wavelet transformation induced multi-time scaling or WATMUS algorithm for accelerated cyclic CPFEM simulations.

Crack nucleation studies are performed for cyclic loads with the maximum applied stress levels at 90–95 % of the macroscopic yield strength. To understand the effect of microstructural characteristics on the fatigue crack nucleation behavior, the dependence of yield strength on the underlying grain orientations and sizes is developed through the introduction of an effective microstructural parameter *Plastic Flow Index* or *PFI*. The *PFI* distribution is found to provide a good measure of the yield strength for a microstructure. However, this distribution is not suitable to undermine the effects of the microstructure on crack nucleation, since it is a *local* event. Hence a local microstructural variable is defined in terms of the neighborhood of the hard grains. Specifically the surface area fraction of soft grains surrounding each hard grain or *SAFSSG* is used to establish the microstructural sensitivity of cycles to crack nucleation. The WATMUS-based CPFEM simulations of three representative microstructures are performed under cyclic dwell loading and the cycles to crack nucleation are predicted. The results confirm the effectiveness of the *SAFSSG* in capturing the influence of microstructure on cycles to crack nucleation. Furthermore, simulations with different cyclic load patterns suggest that fatigue crack nucleation in Ti-6242 strongly depends on the dwell cycle hold time at maximum stress. This is in compliance with experimental observations.

Acknowledgements This work has been partially supported by the Air Force Office of Scientific through a grant FA9550-13-1-0062 (Program Manager: Dr. David Stargel) and by the National Science Foundation, Mechanics and Structure of Materials Program through Grant No. CMMI-1100818 (Program Manager: Dr. Thomas Siegmund). This sponsorship is gratefully acknowledged.

References

1. Anahid M, Samal MK, Ghosh S (2011) Dwell fatigue crack nucleation model based on crystal plasticity finite element simulations of polycrystalline Titanium alloys. J Mech Phys Solids 59(10):2157–2176
2. Bache MR (2003) A review of dwell sensitive fatigue in titanium alloys: the role of microstructure, texture and operating conditions. Int J Fatigue 25:1079–1087
3. Bridiera F, McDowell DL, Villechaisea P, Mendeza J (2009) Crystal plasticity modeling of slip activity in Ti-6Al-4V under high cycle fatigue loading. Int J Plast 25:1066–1082
4. Chakraborty P, Ghosh S (2013) Accelerating cyclic plasticity simulations using an adaptive wavelet transformation based multi-time scaling method. Int J Numer Methods Eng 93:1425–1454
5. Chakraborty P, Joseph DS, Ghosh S (2011) Wavelet transformation based multi-time scale crystal plasticity FEM for cyclic deformation in titanium alloys under dwell load. Finite Elem Anal Des 47:610–618
6. Deka D, Joseph DS, Ghosh S, Mills MJ (2006) Crystal plasticity modeling of deformation and creep in polycrystalline Ti-6242. Metall Trans A 37(5):1371–1388
7. Ghosh S, Chakraborty P (2013) Microstructure and load sensitive fatigue crack nucleation in Ti-6242 using accelerated crystal plasticity FEM simulations. Int J Fatigue 48:231–246
8. Goh CH, Wallace JM, Neu RW, McDowell DL (2001) Polycrystal plasticity simulations of fretting fatigue. Int J Fatigue 23:5423–5435
9. Groeber M, Ghosh S, Uchic MD, Dimiduk DM (2008) A framework for automated analysis and simulation of 3D polycrystalline microstructures. Part 1: statistical characterization. Acta Mater 56:1257–1273
10. Groeber M, Ghosh S, Uchic MD, Dimiduk DM (2008) A framework for automated analysis and simulation of 3D polycrystalline microstructures. Part 2: synthetic structure generation. Acta Mater 56:1274–1287
11. Hasija V, Ghosh S, Mills MJ, Joseph DS (2003) Modeling deformation and creep in Ti-6Al alloys with experimental validation. Acta Mater 51:4533–4549
12. Joseph DS, Chakraborty P, Ghosh S (2010) Wavelet transformation based multi-time scaling for crystal plasticity FE simulations under cyclic loading. Comput Methods Appl Mech Eng 199:2177–2194
13. McDowell D, Dunne FPE (2010) Microstructure-sensitive computational modeling of fatigue crack formation. Int J Fatigue 32:1521–1542
14. Mineur M, Villechaise P, Mendeza J (2000) Influence of the crystalline texture on the fatigue behavior of a 316L austenitic stainless steel. Mater Sci Eng A 286:257–268
15. Sackett EE, Germain L, Bache MR (2007) Crystal plasticity, fatigue crack initiation and fatigue performance of advanced titanium alloys. Int J Fatigue 29:2015–2021
16. Sinha S, Ghosh S (2006) Modeling cyclic ratcheting based fatigue life of HSLA steels using crystal plasticity FEM simulations and experiments. Int J Fatigue 28:1690–1704
17. Sinha V, Mills MJ, Williams JC (2004) Understanding the contributions of normal-fatigue and static loading to the dwell fatigue in a near-alpha titanium alloy. Metall Mater Trans A 35:3141–3148
18. Stroh AN (1954) The formation of cracks as a result of plastic flow. Proc R Soc Lond Ser A 223:404–414
19. Venkatramani G, Ghosh S, Mills MJ (2007) A size-dependent crystal plasticity finite element model for creep and load-shedding in polycrystalline Titanium alloys. Acta Mater 55:3971–3986
20. Williams JC (2006) The evaluation of cold dwell fatigue in Ti-6242. FAA report. The Ohio State University

Advances in Multiscale Modeling of Granular Materials

Xikui Li, Yuanbo Liang, Youyao Du, and Bernhard Schrefler

Abstract The paper reports recent advances in multiscale modeling of granular materials, particularly in the second-order computational homogenization method and corresponding global–local mixed FEM-DEM nested analysis scheme. The gradient Cosserat continuum and the classical Cosserat continuum are assumed for modelling granular media at the macro- and meso- scales, respectively. According to the generalized Hill's lemma formulated for the adopted meso-macro continuum modeling the non-uniform macroscopic strain field with macroscopic strain gradients is downscaled to each representative volume element (RVE), while satisfaction of the generalized Hill–Mandel condition is ensured. The advantage of the gradient Cosserat continuum model in capturing the meso-structural size effect and the performance of the proposed second-order computational homogenization in the simulation of strain softening and localization phenomena are demonstrated, without need to specify macroscopic phenomenological constitutive relationship and material failure model.

1 Introduction

Granular materials are highly heterogeneous and discontinuous media at the grain scale. Multiscale methods have been proposed to bridge their two distinct scales ranging from particle scale to continuum scale. The main objective of these methods is to construct a continuum-based constitutive model in terms of properties and responses of the meso-structure of granular materials assigned to the material point, without resorting to macroscopic phenomenological constitutive model [1–6].

X. Li (✉) • Y. Liang • Y. Du
The State Key Laboratory of Structural Analysis for Industrial Equipment, Dalian University of Technology, Dalian 116024, P.R. China
e-mail: xikuili@dlut.edu.cn

B. Schrefler
Department of Civil, Environmental and Architectural Engineering, University of Padua, via Marzolo 9, 35131 Padua, Italy
e-mail: bernhard.schrefler@unipd.it

P. Trovalusci (ed.), *Materials with Internal Structure*, Springer Tracts in Mechanical Engineering, DOI 10.1007/978-3-319-21494-8_5

Equivalent material properties of heterogeneous media, which are modelled as elastic Cauchy or Cosserat continua at the macro-scale, have been obtained as results of analytical or semi-analytical homogenization techniques [7–11]. When significant meso-structural evolution in the granular material develops, severe dissipative sliding and rolling frictions and loss of contacts among immediate neighboring particles occur and the irreversible energy dissipation of effective continuum, such as damage-plastic one, is to be taken into account [12, 13]. Then computational multiscale approaches [14–23] should be adopted to establish the meso-mechanically informed non-linear macroscopic constitutive relationships.

One promising method among computational multiscale approaches is the computational homogenization approach (the global–local nested analysis scheme) [21–26] under the category of concurrent methods [14]. The approach enables incorporating large deformations and upscaling nonlinear material behaviors of well-characterized meso-structure evolving with the load history, while not requiring the macroscopic constitutive relationship to be specified a priori at selected macroscopic points.

In the frame of computational homogenization, granular material is homogenized with the Cosserat continuum rather than the Cauchy continuum due to the nature of the granular medium as a discrete particle assembly at the meso-scale [1–5, 23, 27–29]. Although a high-order continuum structure is introduced into the classical Cosserat continuum, the admissible meso-scale boundary conditions derived from the generalized Hill's lemma [30] are still prescribed by a uniform macroscopic strain field attributed to each RVE if the classical Cosserat continuum is assumed for both the macro-scale and all RVEs in the macro-meso homogenization [31, 23]. It implies that the macroscopic strain field scaled down to each RVE is restricted to be uniform, and no high-order modes such as bending deformation modes of the RVE due to gradients of the macroscopic strain field over the spatial length scale associated to the RVE size can be represented. The macroscopic energy product may be incorrectly predicted due to the absence of the high-order deformation modes in a homogenization procedure using the classical Cosserat continuum model at the macroscopic level. Indeed, the rationality of the uniform macroscopic strain field attributed to each RVE relies on the concept of separation of scales. The uniformity assumption is not appropriate in critical regions of high strain gradients. As a consequence, the first-order computational homogenization methods are not suited for the analysis of strain localization. It is remarked that satisfaction of the generalized Hill–Mandel condition in the homogenization is ensured if and only if the meso-scale boundary conditions attributed to each meso-structural RVE are enforced by the macroscopic strain (or stress) field so that the boundary integrals at the right-hand side of the corresponding Hill's lemma equal null.

To remedy the defects of the first-order homogenization scheme mentioned above it is required to develop the second-order computational homogenization for granular materials, in which the gradient Cosserat continuum model and the classical Cosserat continuum model are adopted for both the macro-scale and all RVEs, respectively [32]. The inclusion of gradients would also introduce an internal length scale [33, 34] which is effective for localization analysis in all

situations. According to the generalized Hill's lemma derived for the second-order computational homogenization the non-uniform macroscopic strain field with macroscopic strain gradients may be transferred to each RVE, while satisfaction of the generalized Hill–Mandel condition is ensured. The macroscopic strain field is no longer restricted to be uniform over the spatial length scale associated to the RVE size, and the high-order (bending) deformation modes of the RVE may be represented. Consequently, the second-order computational homogenization is appropriate in critical regions of high strain gradients.

To formulate the generalized Hill's lemma each RVE is modelled as a classical Cosserat continuum. On the other hand, the RVE is also modelled as a discrete particle assembly for a detailed description of the RVE meso-structure and its evolutions. Equivalence between the discrete particle assembly and the classical Cosserat continuum at the RVE scale was established by Chang and Kuhn [2] in the sense of the equivalence between the virtual work of the discrete system and the virtual work of the classical Cosserat continuum approximately restricted to continuous virtual displacement fields with a polynomial series containing quadratic terms.

With this equivalence the non-uniform macroscopic strain field derived from the generalized Hill's lemma is imposed to deform the peripheral particles of the RVE of discrete particle assembly. The second-order computational homogenization method and the global–local FEM-DEM nested analysis scheme for granular material are developed as in [35, 36]. In the method the material is modelled as a gradient Cosserat continuum using the mixed FEM [36] and a discrete particle assembly using the DEM [37, 38] at the macro- and meso-scales, respectively.

A key issue in the development of the FEM-DEM nested analysis scheme is to construct a displacement-based finite element (FE) attaining C^1-continuity of the interpolation of displacement for the gradient Cosserat continuum, or alternatively, a mixed FE based on the Hu-Washizu generalized variational principle to circumvent the C^1-continuity requirement [36]. A potential promising approach to numerically perform the boundary value problem (BVP) of the gradient Cosserat continuum is the element-free Galerkin (EFG) method with high-order interpolation approximations, and keeping at the same time high computational efficiency and accuracy [39].

The BVP for the RVE of discrete particle assembly is well determined and performed by the DEM. The meso-mechanical behavior is then identified with the DEM solutions for the BVP of the RVE, in which the discontinuity (loss and re-generation of contacts) and dissipative inter-particle movement involved at the meso-scale and their evolutions with respect to the loading history are taken into account.

To develop the second-order computational homogenization for granular material, downscaling and upscaling rules to perform the two-way coupling should be specified. The downscaling determines the meso-scale BVP of the RVE in light of the Hill's lemma. On the other hand, the upscaling transits back the meso-mechanically informed macroscopic stress variables and rate stress–strain constitutive equations to the macro-scale from volume average of DEM solutions for the BVP of the RVE at each incremental load step.

2 Gradient Cosserat Continuum Model

The independent kinematic degrees of freedom in Cosserat continuum are the displacement u_i and microrotation ω_i [40]. In addition to the strain variables ε_{ji} and κ_{ji} defined by

$$\varepsilon_{ji} = u_{i,j} - e_{kji}\omega_k, \qquad \kappa_{ji} = \omega_{i,j} \tag{1}$$

the strain gradient E_{ljk} is defined in the gradient-enhanced Cosserat continuum model and can be decomposed into two parts, expressed as

$$E_{ljk} = \frac{\partial \varepsilon_{jk}}{\partial x_l} = u_{k,jl} - e_{ijk}\omega_{i,l} = \hat{E}_{ljk} + \check{E}_{ljk} \tag{2}$$

Accordingly, in addition to independent classical Cauchy stress σ_{ji} and couple stress μ_{ji}, the stress moment Σ_{ljk} is introduced and decomposed into symmetric part $\hat{\Sigma}_{ljk}$ and skew-symmetric part $\tilde{\Sigma}_{ljk}$

$$\Sigma_{ljk} = \hat{\Sigma}_{ljk} + \tilde{\Sigma}_{ljk} \tag{3}$$

The equilibrium equations for the gradient Cosserat continuum are

$$\left(\sigma_{ji} - \Sigma_{kji,k}\right)_{,j} = b_i^f, \qquad \mu_{ji,j} + e_{ijk}\left(\sigma_{jk} - \Sigma_{ljk,l}\right) = b_i^m \tag{4}$$

Equilibrium on the surface of the body gives

$$t_i = \left(\sigma_{ji} - \Sigma_{kji,k}\right) n_j, \quad m_i = \left(\mu_{ji} - e_{ilk}\Sigma_{jlk}\right) n_j, \quad g_{ji} = \Sigma_{kji} n_k \tag{5}$$

where t_i, m_i, and g_{ji} are the surface traction, the surface couple, and the surface high-order traction, n_j is the unit vector normal to the surface. Due to the existence of curved surfaces, t_i and g_{ji} are replaced by the generalized surface traction t_i^* and the double stress traction r_i on the surface given by

$$t_i^* = t_i + n_k n_j \Sigma_{kji}\left(D_p n_p\right) - D_j\left(n_k \Sigma_{kji}\right), \qquad r_i = n_k n_j \Sigma_{kji} \tag{6}$$

with $D_j = \left(\delta_{ji} - n_j n_i\right)\frac{\partial}{\partial x_i}$

3 Generalized Hill's Lemma and RVE Boundary Conditions: Downscaling

The derived generalized Hill's lemma for the second-order computational homogenization of the gradient Cosserat continuum is written as

$$\begin{aligned}&\overline{\sigma_{ji}\varepsilon_{ji}} + \overline{\mu_{ji}\kappa_{ji}} - \overline{\sigma}_{ji}\overline{\varepsilon}_{ji} - \overline{\mu}_{ji}\overline{\kappa}_{ji} - \overline{\Sigma}_{lji}\overline{E}_{lji}\\ &= \frac{1}{V}\int_{S_r} \left(n_k\sigma_{ki} - n_k\overline{\sigma}_{ki}\right)\left(u_i - \overline{u}_{i,j}x_j - \frac{1}{2}\overline{u}_{i,jl}x_jx_l\right) dS_r\\ &+ \frac{1}{V}\int_{S_r} \left(n_k\mu_{ki} - n_k\overline{\mu}_{ki}\right)\left(\omega_i - \overline{\omega}_i - \overline{\omega}_{i,l}x_l\right) dS_r\end{aligned} \tag{7}$$

where $x_j(x_l)$ are the coordinates of a point on the boundary S_r of the RVE with the volume V, $\overline{\sigma_{ji}\varepsilon_{ji}}$ and $\overline{\mu_{ji}\kappa_{ji}}$ are defined as volume averages of the meso-scopic products $\sigma_{ji}\varepsilon_{ji}$ and $\mu_{ji}\kappa_{ji}$ over the RVE, respectively.

The Hill–Mandel energy condition for the gradient Cosserat continuum can be directly extracted from the Hill's lemma (7) and given in the form

$$\overline{\sigma_{ji}\varepsilon_{ji}} + \overline{\mu_{ji}\kappa_{ji}} = \overline{\sigma}_{ji}\overline{\varepsilon}_{ji} + \overline{\mu}_{ji}\overline{\kappa}_{ji} + \overline{\Sigma}_{lji}\overline{E}_{lji} \tag{8}$$

provided that the RVE boundary conditions are prescribed so that the following two boundary integrals for the RVE are enforced to vanish

$$\frac{1}{V}\int_{S_r} \left(n_k\sigma_{ki} - n_k\overline{\sigma}_{ki}\right)\left(u_i - \overline{u}_{i,j}x_j - \frac{1}{2}\overline{u}_{i,jl}x_jx_l\right) dS_r = 0 \tag{9}$$

$$\frac{1}{V}\int_{S_r} \left(n_k\mu_{ki} - n_k\overline{\mu}_{ki}\right)\left(\omega_i - \overline{\omega}_i - \overline{\omega}_{i,l}x_l\right) dS_r = 0 \tag{10}$$

To solve the RVE boundary value problem for average stress variables and to derive the meso-mechanically informed macroscopic constitutive equations, the displacement boundary conditions at the RVE are prescribed as

$$u_i|_{S_r} = \overline{u}_{i,j}x_j + \frac{1}{2}\overline{u}_{i,jl}x_jx_l, \qquad \omega_i|_{S_r} = \overline{\omega}_i + \overline{\omega}_{i,l}x_l \tag{11}$$

4 Meso-Mechanically Informed Macroscopic Stress Variables and Constitutive Model: Upscaling

The Hill–Mandel condition (8) can be re-written in two forms:

$$\overline{\sigma_{ji}\varepsilon_{ji}} + \overline{\mu_{ji}\kappa_{ji}} = \overline{\sigma}_{ji}\overline{\Gamma}_{ji} + \overline{T}_k\overline{\omega}_k + \overline{\mu}^0_{ji}\overline{\kappa}_{ji} + \hat{\overline{\Sigma}}_{jlk}\overline{E}_{jlk} \tag{12}$$

$$\overline{\sigma_{ji}\varepsilon_{ji}} + \overline{\mu_{ji}\kappa_{ji}} = \overline{\sigma}_{ji}\overline{\Gamma}_{ji} + \overline{T}_k\overline{\omega}_k + \overline{\mu}^*_{ji}\overline{\kappa}_{ji} + \hat{\overline{\Sigma}}_{jlk}\hat{\overline{E}}_{jlk} \tag{13}$$

where the macro internal torque $\overline{T}_k$ and derivatives of translational displacements $\overline{\Gamma}_{ji}$ are defined as

$$\overline{T}_k = -e_{kji}\overline{\sigma}_{ji}, \qquad \overline{\Gamma}_{ji} = \frac{1}{V}\int_V u_{i,j}dV \tag{14}$$

and the generalized couple stresses are defined as

$$\overline{\mu}^0_{ji} = \overline{\mu}_{ji} - e_{ikl}\tilde{\overline{\Sigma}}_{jkl}, \qquad \overline{\mu}^*_{ji} = \overline{\mu}^0_{ji} - e_{ikl}\hat{\overline{\Sigma}}_{jkl} = \overline{\mu}_{ji} - e_{ikl}\overline{\Sigma}_{jkl} \tag{15}$$

The boldfaced forms of macroscopic stress measures $\overline{\sigma}_{ji}, \overline{T}_k, \hat{\overline{\Sigma}}_{jkl}, \overline{\mu}^0_{ji}, \overline{\mu}^*_{ji}$ can be expressed below in the form of boundary integrals along the RVE boundary. With the equivalence between the classical Cosserat and the discrete particle assembly at the RVE scale [2], those boundary integrals are discretized into discrete quantities assigned at the N_c contact points of the peripheral particles of the particle assembly with the RVE boundary, i.e.,

$$\overline{\boldsymbol{\sigma}} = \frac{1}{V}\int_{S_r}\mathbf{x}\otimes\mathbf{t}dS = \frac{1}{V}\sum_{i=1}^{N_c}\mathbf{x}_i^c\otimes\mathbf{t}_i^c\Delta S_{r,i} = \frac{1}{V}\sum_{i=1}^{N_c}\mathbf{x}_i^c\otimes\mathbf{f}_i^c \tag{16}$$

$$\hat{\overline{\boldsymbol{\Sigma}}} = \frac{1}{2V}\int_{S_r}\mathbf{x}\otimes\mathbf{x}\otimes\mathbf{t}dS = \frac{1}{2V}\sum_{i=1}^{N_c}\mathbf{x}_i^c\otimes\mathbf{x}_i^c\otimes\mathbf{f}_i^c \tag{17}$$

$$\begin{aligned}\overline{\boldsymbol{\mu}}^0 &= \frac{1}{V}\int_{S_r}\mathbf{x}\otimes\mathbf{m}dS + \frac{1}{2V}\int_{S_r}\mathbf{x}\otimes\mathbf{x}\otimes\mathbf{t}dS:\mathbf{e}\\ &= \frac{1}{V}\sum_{i=1}^{N_c}\mathbf{x}_i^c\otimes\mathbf{m}_i^{ext} + \frac{1}{2V}\sum_{i=1}^{N_c}\mathbf{x}_i^c\otimes\mathbf{x}_i^c\otimes\mathbf{f}_i^c:\mathbf{e}\end{aligned} \tag{18}$$

$$\overline{\boldsymbol{\mu}}^* = \frac{1}{V}\sum_{i=1}^{N_c}\mathbf{x}_i^c\otimes\mathbf{m}_i^{ext}, \qquad \overline{\mathbf{T}} = -\mathbf{e}:\overline{\boldsymbol{\sigma}} = -\frac{1}{V}\mathbf{e}:\sum_{i=1}^{N_c}\mathbf{x}_i^c\otimes\mathbf{f}_i^c \tag{19}$$

where $\mathbf{x}_i^c, \mathbf{t}_i^c$, and $\mathbf{m}_i^c$ are the position vector, surface traction, and couple vectors, respectively, defined at the *ith* contact point of peripheral particles with the outside material, $\mathbf{f}_i^c$ and $\mathbf{m}_i^{ext}$ are the traction force and couple moment applied to the peripheral particle via the *ith* contact point by the outside material, respectively, $\Delta S_{r,i}$ is the length of the boundary segment associated with the *ith* contact point, and $\mathbf{e}$ is the boldfaced form of the third-order permutation tensor e_{kji}.

The discrete counterpart of the boundary conditions given by Eq. (11), which are prescribed on the N_c peripheral particles through their contacting points with the RVE boundary, can be written in the rate form for a typical contacting point b as

$$\dot{\mathbf{u}}_b^c = \mathbf{x}_b^c \cdot \dot{\overline{\mathbf{\Gamma}}} + \frac{1}{2}\left(\mathbf{x}_b^c \otimes \mathbf{x}_b^c\right) : \dot{\overline{\mathbf{E}}}, \qquad \dot{\boldsymbol{\omega}}_b = \dot{\overline{\boldsymbol{\omega}}} + \mathbf{x}_b^c \cdot \dot{\boldsymbol{\kappa}} \tag{20}$$

where $\dot{\overline{\mathbf{\Gamma}}}$, $\dot{\overline{\mathbf{E}}}$, $\dot{\overline{\boldsymbol{\omega}}}$, $\dot{\boldsymbol{\kappa}}$ are boldfaced forms of $\dot{\overline{\Gamma}}_{ji}$, $\dot{\overline{E}}_{lji}\left(\dot{\overline{u}}_{i,jl}\right)$, $\dot{\overline{\omega}}_i, \dot{\kappa}_{ji}\left(\dot{\overline{\omega}}_{i,j}\right)$, respectively, $\dot{\mathbf{u}}_b^c$ is the rate translational displacement of the contact point with the position $\mathbf{x}_b^c$ of peripheral particle $\mathbf{x}_b$, and $\dot{\boldsymbol{\omega}}_b$ is the microrotation rate of the peripheral particle b contacting with the RVE boundary.

Equations (11) and (20) transfer the macroscopic strain measures and their gradients down to each RVE via its boundary in the downscaling process. The DEM solver is used to solve for the BVP of the discrete particle assembly within each meso-structural RVE. The non-linear meso-mechanical behavior of the well-determinate meso-structure is identified with the DEM solutions for the BVP of the RVE, in which the discontinuity and dissipative relative movements between each two immediate neighboring particles at the meso-scale are taken into account.

The upscale transition for the macroscopic stress measures is fulfilled by Eqs. (16)–(19). With the transformation of the RVE boundary conditions from the contact points of the peripheral particles on the RVE boundary to their centers, substitution of RVE boundary conditions Eq. (20) into the rate forms of Eqs. (16)–(19) results in meso-mechanically informed macroscopic constitutive relationships for the gradient-enhanced Cosserat continuum of granular materials as follows:

$$\dot{\overline{\boldsymbol{\sigma}}} = \mathbf{D}_{\sigma\Gamma} : \dot{\overline{\mathbf{\Gamma}}} + \mathbf{D}_{\sigma\omega} \cdot \dot{\overline{\boldsymbol{\omega}}} + \mathbf{D}_{\sigma\hat{E}} \vdots \dot{\overline{\mathbf{E}}} + \mathbf{D}_{\sigma\kappa} : \dot{\boldsymbol{\kappa}} \tag{21}$$

$$\dot{\overline{\mathbf{T}}} = \mathbf{D}_{\mathrm{T}\Gamma} : \dot{\overline{\mathbf{\Gamma}}} + \mathbf{D}_{\mathrm{T}\omega} \cdot \dot{\overline{\boldsymbol{\omega}}} + \mathbf{D}_{\mathrm{T}\hat{E}} \vdots \dot{\overline{\mathbf{E}}} + \mathbf{D}_{\mathrm{T}\kappa} : \dot{\boldsymbol{\kappa}} \tag{22}$$

$$\dot{\overline{\mathbf{\Sigma}}} = \mathbf{D}_{\hat{\Sigma}\Gamma} : \dot{\overline{\mathbf{\Gamma}}} + \mathbf{D}_{\hat{\Sigma}\omega} \cdot \dot{\overline{\boldsymbol{\omega}}} + \mathbf{D}_{\hat{\Sigma}\hat{E}} \vdots \dot{\overline{\mathbf{E}}} + \mathbf{D}_{\hat{\Sigma}\kappa} : \dot{\boldsymbol{\kappa}} \tag{23}$$

$$\dot{\overline{\boldsymbol{\mu}}}^0 = \mathbf{D}_{\mu\Gamma} : \dot{\overline{\mathbf{\Gamma}}} + \mathbf{D}_{\mu\omega} \cdot \dot{\overline{\boldsymbol{\omega}}} + \mathbf{D}_{\mu\hat{E}} \vdots \dot{\overline{\mathbf{E}}} + \mathbf{D}_{\mu\kappa} : \dot{\boldsymbol{\kappa}} \tag{24}$$

The 16 meso-mechanically informed macroscopic tangent modular tensors shown in Eqs. (21)–(24) and their dependence on the meso-structure of the RVE of discrete particle assembly and its evolution are formulated in [35] and not be given here owing to the limitation of space.

5 Numerical Results

An advantage of the second-order computational homogenization approach over the first-order one is the capability of taking into account the absolute size of the meso-structure and subsequently exhibiting the meso-structural size effects. The capability is particularly demonstrated via an example composed of a set of RVEs with the same meso-structure. Each RVE consists of 40 uniform round particles collocated with the same regular pattern but different absolute sizes. The material parameters for the round particles are listed in [36]. The four terms on the right side of Eq. (13) are divided into two parts denoted by $J_1 = \overline{\sigma}_{ji}\,\overline{\Gamma}_{ji} + \overline{T}_k\,\overline{\omega}_k + \overline{\mu}^*_{ji}\overline{\kappa}_{ji}$ and $J_2 = \hat{\overline{\Sigma}}_{kji}\hat{\overline{E}}_{kji}$. They are used as indices for the low- and high-order energy densities of the RVE respectively, in the gradient Cosserat continuum. Figure 1 plots J_1 and J_2 of the RVE versus the radius of the particle obtained by the first-order and the proposed second-order homogenization schemes as the RVEs are subjected to a varying macroscopic strain gradient.

The square panel shown in Fig. 2a is subjected to uniaxial compression between two rigid plates. The compression is applied by a vertical prescribed displacement control. From the symmetry condition, which holds because gravity forces are neglected, the calculation is performed for only one fourth of the panel of size $L \times L (L = 30$ m). The panel is discretized by the regular 20×20 mixed FE mesh. The RVEs assigned at all integrating points of the FE mesh are initially morphologically identical with the same regular meso-structure. To investigate the influence of the RVE size on the macroscopic mechanical behaviors, the example is performed by using the three different samples of RVE. The three samples of RVE are assumed to have the same meso-structure but different RVE sizes. Each sample of RVE possesses the square shape of the effective Cosserat continuum with size $l \times l$ and consists of n_r uniform round discrete particles of radius $r = 0.02m$ collocated with the same regular pattern. The three samples of RVE used in the example are: RVE24: $l = 0.2097m$ $n_r = 24$; RVE40: $l = 0.2663m$ $n_r = 40$;

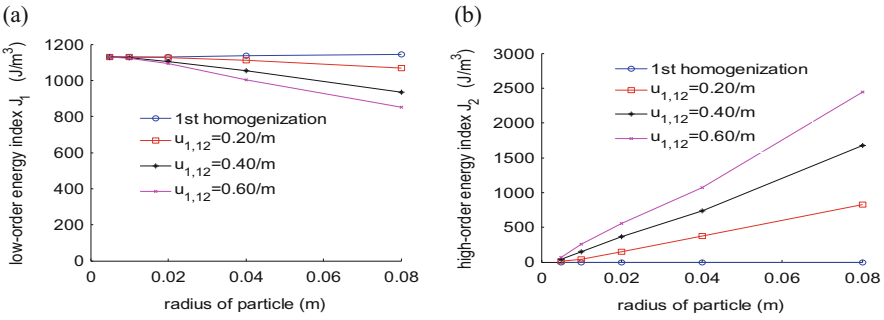

Fig. 1 Energy products versus the particle radius of the RVEs subjected to different macro-strain gradients: (**a**) J_1; (**b**) J_2

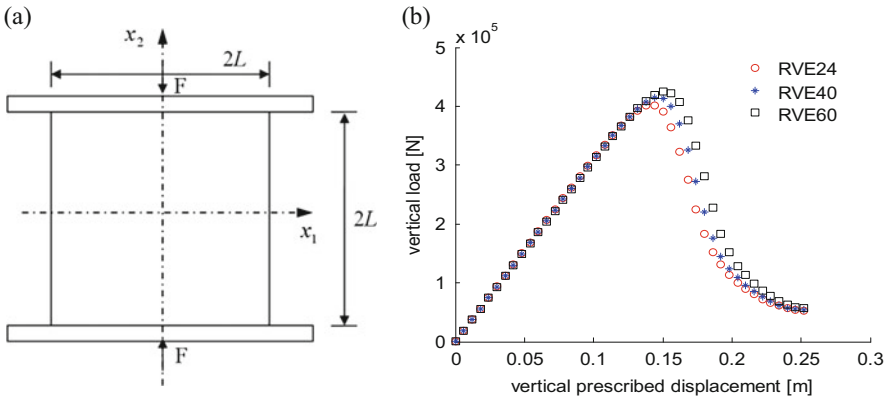

Fig. 2 Compression problem of a square panel. (**a**) Sizes and the vertical load applied by two rigid plates; (**b**) Load–displacement curves using the same 20×20 regular element mesh for three samples of RVE with the same meso-structure but different RVE sizes

RVE60: $l = 0.3228m$ $n_r = 60$. The material parameters for the round particles are listed in [36]. The load–displacement curves obtained for the three samples of RVE are plotted in Fig. 2b. It demonstrates the performance of the second-order computational homogenization method and corresponding global–local mixed FEM-DEM nested analysis scheme in the simulation of strain softening, without any need to specify the macroscopic phenomenological constitutive relationship and material failure model. In addition, the influence of the window size of RVE on macroscopic mechanical behaviors of the panel, i.e., on the load-carrying capability and the softening behavior is also observed.

6 Concluding Remarks

1. In the frame of computational homogenization granular medium should be modeled as Cosserat continuum instead of Cauchy continuum at the macro-scale due to its nature as a discrete particle assembly at the meso-scale.
2. To be suitable for the localization problem, the RVE boundary condition in computational homogenization should be prescribed by non-uniform macroscopic strain field with macroscopic strain gradients.
3. To downscale the non-uniform macroscopic strain field with macroscopic strain gradients to each RVE the second-order computational homogenization with gradient-enhanced macroscopic continuum model should be adopted.

Acknowledgement The authors are pleased to acknowledge the support for this work by the National Natural Science Foundation of China through contract/grant numbers 11372066, 11072046 and the National Key Basic Research and Development Program (973 Program) through contract number 2010CB731502.

References

1. Pasternak E, Muhlhaus HB (2005) Generalised homogenisation procedures for granular materials. J Eng Math 52:199–229
2. Chang CS, Kuhn MR (2005) On virtual work and stress in granular media. Int J Solids Struct 42:3773–3793
3. Ehlers W, Ramm E, Diebels S, d'Addetta G (2003) From particle ensembles to Cosserat continua: homogenization of contact forces towards stresses and couple stresses. Int J Solids Struct 40:6681–6702
4. d'Addetta G, Ramm E, Diebels S, Ehlers W (2004) A particle center based homogenization strategy for granular assemblies. Eng Comput 21:360–383
5. Alonso-Marroquin F (2011) Static equations of the Cosserat continuum derived from intra-granular stresses. Granul Matter 13:189–196
6. Andrade JE, Avila CF, Hall SA, Lenoir N, Viggiani G (2011) Multiscale modeling and characterization of granular matter: from grain kinematics to continuum mechanics. J Mech Phys Solids 59:237–250
7. Hicher PY, Chang CS (2005) Evaluation of two homogenization techniques for modeling the elastic behaviors of granular materials. J Eng Mech 131:1184–1194
8. Nemat-Nasser S, Hori M (1999) Micromechanics: overall properties of heterogeneous materials. Elsevier, Amsterdam
9. Suiker ASJ, de Borst R (2005) Enhanced continua and discrete lattices for modelling granular assemblies. Phil Trans Soc A 363:2543–2580
10. Bigoni D, Drugan WJ (2007) Analytical derivation of Cosserat moduli via homogenization of heterogeneous elastic materials. J Appl Mech 74:741–753
11. La Ragione L, Jenkins JT (2007) The initial response of an idealized granular material. Proc R Soc A 463:735–758
12. Gardiner BS, Tordesillas A (2005) Micromechanical constitutive modeling of granular media: evolution and loss of contact in particle clusters. J Eng Mech 52:93–106
13. Papanicolopulos SA, Veveakis E (2011) Sliding and rolling dissipation in Cosserat plasticity. Granul Matter 13:197–204
14. Luscher DJ, McDowell DL, Bronkhorst CA (2010) A second gradient theoretical framework for hierarchical multiscale modeling of materials. Int J Plast 26:1248–1275
15. Forest S, Pradel F, Sab K (2001) Asymptotic analysis of heterogeneous Cosserat media. Int J Solids Struct 38:4585–4608
16. Kouznetsova V, Brekelmans W, Baaijens F (2001) An approach to micro–macro modeling of heterogeneous materials. Comput Mech 27:37–48
17. Wagner GJ, Liu WK (2003) Coupling of atomistic and continuum simulations using a bridging scale decomposition. J Comput Phys 190:249–274
18. Li XK, Wan K (2011) A bridging scale method for granular materials with discrete particle assembly – Cosserat continuum modeling. Comput Geotech 38:1052–1068
19. Wellmann C, Wriggers P (2012) A two scale model of granular materials. Comput Methods Appl Mech Eng 205–208:46–58
20. Vernerey F, Liu WK, Moran B (2007) Multi-scale micromorphic theory for hierarchical materials. J Mech Phys Solids 55:2603–2651
21. Terada K, Kikuchi N (2001) A class of general algorithms for multi-scale analyses of heterogeneous media. Comput Methods Appl Mech Eng 190:5427–5464
22. Kaneko K, Terada K, Kyoya T, Kishino Y (2003) Global–local analysis of granular media in quasi-static equilibrium. Int J Solids Struct 40:4043–4069
23. Li XK, Liu QP, Zhang JB (2010) A micro–macro homogenization approach for discrete particle assembly – Cosserat continuum modeling of granular materials. Int J Solids Struct 47:291–303
24. Geers MGD, Kouznetsova VG, Brekelmans WAM (2010) Multi-scale computational homogenization: trends and challenges. J Comput Appl Math 234:2175–2182

25. Kouznetsova V, Geers MGD, Brekelmans WAM (2002) Multi-scale constitutive modelling of heterogeneous materials with a gradient-enhanced computational homogenization scheme. Int J Numer Methods Eng 54:1235–1260
26. Kouznetsova V, Geers MGD, Brekelmans WAM (2004) Multi-scale second-order computational homogenization of multi-phase materials: a nested finite element solution strategy. Comput Methods Appl Mech Eng 193:5525–5550
27. Li XK, Du YY, Duan QL (2013) Micromechanically informed constitutive model and anisotropic damage characterization of Cosserat continuum for granular materials. Int J Damage Mech 22:643–682
28. Kruyt NP (2003) Statics and kinematics of discrete Cosserat-type granular materials. Int J Solids Struct 40:511–534
29. Zhang HW, Wang H, Wriggers P, Schrefler BA (2005) Some investigations on finite element method for contact analysis of multiple Cosserat bodies. Comput Mech 36:444–458
30. Hill R (1963) Elastic properties of reinforced solids: some theoretical principles. J Mech Phys Solids 11:357–372
31. Li XK, Liu QP (2009) A version of Hill's lemma for Cosserat continuum. Acta Mech Sinica 25:499–506
32. Li XK, Zhang JB, Zhang X (2011) Micro–macro homogenization of gradient-enhanced Cosserat media. Eur J Mech A Solids 30:362–372
33. Zhang HW, Schrefler BA (2000) Gradient dependent plasticity model and dynamic strain localisation analysis of saturated and partially saturated porous media: one dimensional model. Eur J Mech A Solids 19:503–524
34. Zhang HW, Schrefler BA (2001) Uniqueness and localisation analysis of elastic–plastic saturated porous media. Int J Numer Anal Methods Geomech 25:29–48
35. Li XK, Zhang X, Zhang JB (2010) A generalized Hill's lemma and micro-mechanically based macroscopic constitutive model for heterogeneous granular materials. Comput Methods Appl Mech Eng 199:3137–3152
36. Li XK, Liang YB, Duan QL, Schrefler BA, Du YY (2014) A mixed finite element procedure of gradient Cosserat continuum for second-order computational homogenisation of granular materials. Comput Mech 54:1331–1356
37. Cundall PA, Strack ODL (1979) A discrete numerical model for granular assemblies. Geotechnique 29:47–65
38. Li XK, Chu XH, Feng YT (2005) A discrete particle model and numerical modeling of the failure modes of granular materials. Eng Comput 22(8):894–920
39. Duan QL, Gao X, Wang BB, Li XK, Zhang HW, Belytschko T, Shao YL (2014) Consistent element-free Galerkin method. Int J Numer Methods Eng. doi:10.1002/nme.4661
40. Onck PR (2002) Cosserat modeling of cellular solids. Comptes Rendus Mecanique 330:717–722

Tensor-Valued Random Fields in Continuum Physics

Anatoliy Malyarenko and Martin Ostoja-Starzewski

Abstract This article reports progress on homogeneous isotropic tensor random fields (TRFs) for continuum mechanics. The basic thrust is on determining most general representations of the correlation functions as well as their spectral expansions. Once this is accomplished, the second step is finding the restrictions dictated by a particular physical application. Thus, in the case of fields of material properties (like conductivity and stiffness), the restriction resides in the positive-definiteness, whereby a connection to experiments and/or computational micromechanics can be established. On the other hand, in the case of fields of dependent properties (e.g., stress, strain and displacement), restrictions are due to the respective field equations.

1 Introduction

Many fields arising in continuum physics take values in linear spaces of tensors over $\mathbb{R}^3$, the three-dimensional Euclidean space. For example, the heat flux and fluid velocity fields take values in the space of rank 1 tensors, whereas the stress, strain, rotation, and curvature-torsion fields take values in the space of rank 2 tensors. These are examples of dependent quantities as opposed to those of constitutive response which are typically independent of the loading: thermal conductivity, piezoelectricity, stiffness, viscosity..., which are either rank 2 or higher. Given the (nearly) ever present randomness of continuum physical phenomena, all of these fields are tensors of random nature. Thus, stochastic continuum physics involves tensor random fields (TRFs). While the mathematics of scalar RFs is very advanced, the tensor case poses many challenges. In the first place, a researcher in stochastic

A. Malyarenko
Division of Applied Mathematics, Mälardalen University, Högskoleplan 1, SE-721 23 Västerås, Sweden
e-mail: anatoliy.malyarenko@mdh.se

M. Ostoja-Starzewski (✉)
Department of Mechanical Science & Engineering, also Institute for Condensed Matter Theory and Beckon Institute, University of Illinois at Urbana-Champaign, Urbana, IL 61801, USA
e-mail: martinos@illinois.edu

P. Trovalusci (ed.), *Materials with Internal Structure*, Springer Tracts in Mechanical Engineering, DOI 10.1007/978-3-319-21494-8_6

mechanics needs a more explicit way of representing and generating vector and TRFs, and, secondly, (s)he needs to consider restrictions imposed by the actual physics on any such field. The principal restrictions stem from the field equations in the case of dependent TRFs and the non-negativeness of energy density and entropy production in the case of independent TRFs.

As background, the theories of first rank TRFs (i.e., vector RFs), date back to turbulence (von Kármán and Horwath [15]; Robertson [11]; Batchelor [1]; Monin and Yaglom [8]), and cosmology (Malyarenko [4]). It is by extending these vector RFs, that some advances were made in theories of second rank TRFs (Lomakin [2, 3]; Shermergor [12]). However, the subject of higher rank TRFs has been touched only in a few restricted settings. In this paper we review our recent work on rank 1, 2, and 4 TRFs, all in the context of wide-sense homogeneous fields, with particular focus on isotropic correlation functions having generally anisotropic realizations. The key role is played here by the theory of invariants and the $O(n)$ group theory.

2 Representations of Rank 1 and Rank 2 TRFs

We begin with V, a finite-dimensional real Hilbert space with norm $\|\cdot\|$. Then, we let $\mathbf{T}(\mathbf{x})$, $\mathbf{x} \in \mathbb{R}^3$ be a random field taking values in (a subset of) V: there is a probability space $(\Omega, \mathscr{F}, \mathsf{P})$, and $\mathbf{T}$ is a function of two variables

$$\mathbf{T}(\mathbf{x}, \omega) \colon E \times \Omega \to V,$$

such that for any fixed $\mathbf{x}_0 \in E$ the function $\mathbf{T}(\mathbf{x}_0, \omega) \colon \Omega \to V$ is measurable. We assume that $\mathsf{E}[\|\mathbf{T}(\mathbf{x})\|^2] < \infty$ and $\mathbf{T}(\mathbf{x})$ is mean-square continuous, i.e.

$$\lim_{\|\mathbf{x}-\mathbf{x}_0\|\to 0} \mathsf{E}[\|\mathbf{T}(\mathbf{x}) - \mathbf{T}(\mathbf{x}_0)\|^2] = 0 \quad \forall \mathbf{x}_0 \in \mathbb{R}^3.$$

Next, we let $E(\mathbf{x}) = \mathsf{E}[\mathbf{T}(\mathbf{x})]$ be the expectation of the field and let $B(\mathbf{x}, \mathbf{y}) = \mathsf{E}[\mathbf{T}(\mathbf{x}) \otimes \mathbf{T}(\mathbf{y})]$ be the two-point correlation function of the random field $\mathbf{T}(\mathbf{x})$. The group $\mathbb{R}^3$ acts on itself by translations. Assume that the above functions are invariant with respect to this action, i.e., for all $\mathbf{x}, \mathbf{y}, \mathbf{z} \in \mathbb{R}^3$,

$$\begin{aligned} E(\mathbf{x} + \mathbf{z}) &= E(\mathbf{x}), \\ B(\mathbf{x} + \mathbf{z}, \mathbf{y} + \mathbf{z}) &= B(\mathbf{x}, \mathbf{y}). \end{aligned} \qquad \forall \mathbf{x}, \mathbf{y}, \mathbf{z} \in \mathbb{R}^3.$$

It follows that $E(\mathbf{x}) = \mathbf{E} \in V$ is constant, while $B(\mathbf{x}, \mathbf{y}) \in V \otimes V$ depends only on the difference $\mathbf{x} - \mathbf{y}$.

Let $K = O(3)$ be the group of rotations and reflections in $\mathbb{R}^3$, and let (V, γ) be an orthogonal representation of K. Suppose that for all $k \in K$ and for all $\mathbf{x} \in \mathbb{R}^3$ we have

$$E(k\mathbf{x}) = \gamma(k)E(\mathbf{x}),$$
$$B(k\mathbf{x}) = \gamma(k)B(\mathbf{x})\gamma^{-1}(k).$$

Our first objective is to find a general form for the expectation and two-point correlation function of such a field. We now consider two particular cases.

2.1 Rank 1 TRF

V has dimension 3, $\gamma(k) = k$. Then $\gamma(k) = k$, $E(\mathbf{x}) = \mathbf{0}$ and

$$B_{ij}(\mathbf{x}, \mathbf{y}) := \mathsf{E}\{[T_i(\mathbf{x}) - \langle T_i(\mathbf{x})\rangle]\left[T_j(\mathbf{y}) - \left\langle T_j(\mathbf{x})\right\rangle\right]\}$$

is represented in terms of two continuous functions K_0, $K_2 \colon [0, \infty) \to \mathbb{R}$ with $K_2(0) = 0$, such that

$$B_{ij}(\mathbf{x}) = \delta_{ij}K_0(\|\mathbf{x}\|) + x_i x_j K_2(\|\mathbf{x}\|). \tag{1}$$

This representation has been known since the classical paper by Robertson [11], where it was proved using the invariants. This line of research goes back to Sir Geoffrey Ingram Taylor [14].

2.2 Rank 2 TRF

V is the space of all symmetric second-rank tensors over $\mathbb{R}^3$, and the representation is $\gamma(k)\mathbf{T} = k\mathbf{T}k^{-1}$. Then $E_{ij}(\mathbf{x}) = C\delta_{ij}$ with $C \in \mathbb{R}$. Using the theory of invariants (see, e.g., Spencer [13]), Lomakin [2] proved that

$$B_{ijlm}(\mathbf{x}, \mathbf{y}) := \mathsf{E}\{\left[T_{ij}(\mathbf{x}) - \left\langle T_{ij}(\mathbf{x})\right\rangle\right][T_{lm}(\mathbf{y}) - \langle T_{lm}(\mathbf{x})\rangle]\}$$

is represented in terms of five continuous functions $K_1, \ldots, K_5 \colon [0, \infty) \to \mathbb{R}$ with $K_3(0) = K_4(0) = K_5(0) = 0$, such that

$$B_{ij\ell m}(\mathbf{x}) = \sum_{n=1}^{5} L^n_{ij\ell m}(\mathbf{x})K_n(\|\mathbf{x}\|). \tag{2}$$

Here

$$\begin{aligned}
L^1_{ij\ell m}(\mathbf{x}) &= \delta_{ij}\delta_{\ell m},\\
L^2_{ij\ell m}(\mathbf{x}) &= \delta_{i\ell}\delta_{jm} + \delta_{im}\delta_{jl},\\
L^3_{ij\ell m}(\mathbf{x}) &= \frac{x_j x_\ell}{\|\mathbf{x}\|^2}\delta_{im} + \frac{x_i x_m}{\|\mathbf{x}\|^2}\delta_{j\ell} + \frac{x_i x_\ell}{\|\mathbf{x}\|^2}\delta_{jm} + \frac{x_j x_m}{\|\mathbf{x}\|^2}\delta_{i\ell},\\
L^4_{ij\ell m}(\mathbf{x}) &= \frac{x_i x_j}{\|\mathbf{x}\|^2}\delta_{\ell m} + \frac{x_\ell x_m}{\|\mathbf{x}\|^2}\delta_{ij},\\
L^5_{ij\ell m}(\mathbf{x}) &= \frac{x_i x_j x_\ell x_m}{\|\mathbf{x}\|^4}.
\end{aligned} \tag{3}$$

Malyarenko and Ostoja-Starzewski [7] found five functions $M^1_{ij\ell m}(\mathbf{x})$ such that

$$\begin{aligned}
M^1_{ij\ell m}(\mathbf{x}) &= \frac{1}{3}L^1_{ij\ell m}(\mathbf{x}),\\
M^2_{ij\ell m}(\mathbf{x}) &= -\frac{1}{3\sqrt{5}}L^1_{ij\ell m}(\mathbf{x}) + \frac{1}{2\sqrt{5}}L^2_{ij\ell m}(\mathbf{x}),\\
M^3_{ij\ell m}(\mathbf{x}) &= -\frac{1}{3}L^1_{ij\ell m}(\mathbf{x}) + \frac{1}{2}L^4_{ij\ell m}(\mathbf{x}),\\
M^4_{ij\ell m}(\mathbf{x}) &= \frac{2\sqrt{2}}{3\sqrt{7}}L^1_{ij\ell m}(\mathbf{x}) - \frac{1}{\sqrt{14}}L^2_{ij\ell m}(\mathbf{x}) + \frac{3}{2\sqrt{14}}L^3_{ij\ell m}(\mathbf{x}) - \frac{\sqrt{2}}{\sqrt{7}}L^4_{ij\ell m}(\mathbf{x}),\\
M^5_{ij\ell m}(\mathbf{x}) &= \frac{1}{2\sqrt{70}}L^1_{ij\ell m}(\mathbf{x}) + \frac{1}{2\sqrt{70}}L^2_{ij\ell m}(\mathbf{x}) - \frac{\sqrt{5}}{2\sqrt{14}}L^3_{ij\ell m}(\mathbf{x})\\
&\quad - \frac{\sqrt{5}}{2\sqrt{14}}L^4_{ij\ell m}(\mathbf{x}) + \frac{\sqrt{35}}{2\sqrt{2}}L^5_{ij\ell m}(\mathbf{x}).
\end{aligned} \tag{4}$$

and the representation

$$B_{ij\ell m}(\mathbf{x}) = \sum_{n=1}^{5} M^n_{ij\ell m}(\mathbf{x}) K_n(\|\mathbf{x}\|). \tag{5}$$

It has been proved in the aforementioned reference that the representation (5) is equivalent to (2), according to the transformation (4).

Note: On the one hand, Lomakin's functions (3) are simpler than functions (4). On the other hand, (3) lead to spectral expansions (Malyarenko and Ostoja-Starzewski, [6]) of tensor-valued homogeneous and isotropic random fields similar to those in Yaglom [16].

Note: Given that $\mathbf{T}$ has diagonal and off-diagonal components, there are five special cases of B_{ijkl} which shed light on the physical meaning of K_n's:

1. $\mathsf{E}[T_{ij}(\mathbf{0})T_{kl}(\mathbf{x})]|_{i=j=k=l}$; i.e. auto-correlations of diagonal terms:

$$\mathsf{E}[T_{11}(\mathbf{0})T_{11}(\mathbf{x})] = K_1 + 2K_2 + 2x_1^2K_3 + 4x_1^2K_4 + x_1^4K_5 \tag{6}$$

and then $\mathsf{E}[T_{22}(\mathbf{0})T_{22}(\mathbf{x})]$ and $\mathsf{E}[T_{33}(\mathbf{0})T_{33}(\mathbf{x})]$ by cyclic permutations $1 \to 2 \to 3$.

2. $\mathsf{E}[T_{ij}(\mathbf{0})T_{kl}(\mathbf{x})]|_{i=j\neq k=l}$; i.e. cross-correlations of diagonal terms:

$$\mathsf{E}[T_{11}(\mathbf{0})T_{22}(\mathbf{x})] = K_1 + \left(x_2^2 + x_1^2\right) K_3 + x_2^2 x_1^2 K_5 \tag{7}$$

and then $\mathsf{E}[T_{22}(\mathbf{0})T_{33}(\mathbf{x})]$ and $\mathsf{E}[T_{33}(\mathbf{0})T_{11}(\mathbf{x})]$ by cyclic permutations $1 \to 2 \to 3$.

3. $\mathsf{E}[T_{ij}(\mathbf{0})T_{kl}(\mathbf{x})]|_{i=k\neq j=l}$; i.e. auto-correlations of off-diagonal terms:

$$\mathsf{E}[T_{12}(\mathbf{0})T_{12}(\mathbf{x})] = K_2 + \left(x_1^2 + x_2^2\right) K_4 + x_1^2 x_2^2 K_5 \tag{8}$$

and then $\mathsf{E}[T_{23}(\mathbf{0})T_{23}(\mathbf{x})]$ and $\mathsf{E}[T_{31}(\mathbf{0})T_{31}(\mathbf{x})]$ by cyclic permutations $1 \to 2 \to 3$.

4. $\mathsf{E}[T_{ij}(\mathbf{0})T_{kl}(\mathbf{x})]|_{j\neq i=k\neq l\neq j}$; i.e. cross-correlations of off-diagonal terms:

$$\mathsf{E}[T_{12}(\mathbf{0})T_{13}(\mathbf{x})] = x_2 x_3 K_4 + x_1^2 x_2 x_3 K_5 \tag{9}$$

and then $\mathsf{E}[T_{13}(\mathbf{0})T_{32}(\mathbf{x})]$ and $\mathsf{E}[T_{32}(\mathbf{0})T_{12}(\mathbf{x})]$ by cyclic permutations $1 \to 2 \to 3$.

5. $\mathsf{E}[T_{ij}(\mathbf{0})T_{kl}(\mathbf{x})]|_{i=j=k\neq l\neq j}$; i.e. cross-correlations of diagonal with off-diagonal terms: such as

$$\mathsf{E}[T_{11}(\mathbf{0})T_{12}(\mathbf{x})] = x_1 x_2 \left(K_3 + 2K_4\right) + x_1 x_2^3 K_5 \tag{10}$$

and

$$\mathsf{E}[T_{12}(\mathbf{0})T_{13}(\mathbf{x})] = x_2 x_3 K_3 + x_1^2 x_2 x_3 K_5 \tag{11}$$

and the other ones by cyclic permutations $1 \to 2 \to 3$.

In principle, we can determine these five correlations for a specific physical situation. For example, when $\mathbf{T}$ is the anti-plane elasticity tensor for a given resolution (or mesoscale), we can use micromechanics or experiments (Ostoja-Starzewski [9]), and then determine the best fits of K_n $(n = 1, \ldots, 5)$ coefficients.

3 Spectral Expansions of Homogeneous and Isotropic TRFs

In a line of research different from that introduced above, Yaglom [16] proved that the correlation tensor (1) has the following spectral expansion:

$$R_{ij}(\boldsymbol{\xi}) = \int_0^\infty \left[\frac{j_1(\lambda\rho)}{\lambda\rho}\delta_{ij} - j_2(\lambda\rho)\frac{\xi_i\xi_j}{\rho^2} \right] \mathrm{d}\Phi_1(\lambda) + \int_0^\infty \left[\left(j_0(\lambda\rho) - \frac{j_1(\lambda\rho)}{\lambda\rho} \right)\delta_{ij} + j_2(\lambda\rho)\frac{\xi_i\xi_j}{\rho^2} \right] \mathrm{d}\Phi_2(\lambda), \qquad (12)$$

where Φ_1 and Φ_2 are two finite measures on $[0,\infty)$ with $\Phi_1(\{0\}) = \Phi_2(\{0\})$ and where $j_i(t)$ are spherical Bessel functions. In particular, Robertson's functions $A(\rho)$ and $B(\rho)$ [i.e., our K_0 and K_1 in (1)] have the form

$$A(\rho) = \tfrac{1}{\rho^2}\left(\int_0^\infty j_2(\lambda\rho)\,\mathrm{d}\Phi_2(\lambda) - \int_0^\infty j_1(\lambda\rho)\,\mathrm{d}\Phi_1(\lambda) \right),$$
$$B(\rho) = \int_0^\infty \tfrac{j_1(\lambda\rho)}{\lambda\rho}\,\mathrm{d}\Phi_1(\lambda) + \int_0^\infty \left(j_0(\lambda\rho) - \tfrac{j_1(\lambda\rho)}{\lambda\rho} \right) \mathrm{d}\Phi_2(\lambda).$$

In [6] we have established spectral expansions of homogeneous and isotropic random fields taking values in the three-dimensional Euclidean space $\mathbb{R}^3$ and in the space $\mathsf{S}^2(\mathbb{R}^3)$ of symmetric rank 2 tensors over $\mathbb{R}^3$, whereby we found a link between the theory of random fields and the theory of finite-dimensional convex compacta.

4 The Spectral Expansion of the Elasticity Random Field

Here we consider planar classical elasticity. Let $E = \mathbb{R}^2$ be a two -dimensional Euclidean space with an inner product $(\cdot,\cdot)$ (the space domain). The Hooke law in the theory of elasticity says that $\sigma(\mathbf{x}) = \mathsf{H}(\mathbf{x})\varepsilon(\mathbf{x})$, where $\sigma(\mathbf{x})$ is the stress tensor of a deformable body, $\varepsilon(\mathbf{x})$ its strain tensor, and where $\mathsf{H}(\mathbf{x})$ is a symmetric linear operator on the space $\mathsf{S}^2(E)$ of the symmetric rank 2 tensors over E called the elasticity (or stiffness) tensor. It is taken as a random field: there is a probability space $(\Omega, \mathscr{F}, \mathsf{P})$, and H is a function of two variables

$$\mathsf{H}(\mathbf{x},\omega)\colon E \times \Omega \to \mathsf{S}^2(\mathsf{S}^2(E)),$$

such that for any fixed $\mathbf{x}_0 \in E$ the function $\mathsf{H}(\mathbf{x}_0,\omega)\colon \Omega \to \mathsf{S}^2(\mathsf{S}^2(E))$ is measurable. In [5] we have reported two results:

1. The expected value of the elasticity random field $\mathsf{H}(\mathbf{x})$ is

$$E_{ij\ell m}(\mathbf{x}) = C_1\delta_{ij}\delta_{\ell m} + C_2(\delta_{i\ell}\delta_{jm} + \delta_{im}\delta_{j\ell}), \qquad C_1, C_2 \in \mathbf{R},$$

where C_1 and C_2 are recognized as the Lamé constants λ and μ, respectively. The correlation tensor of the above field has the form

$$R_{i\cdots m'}(\rho,\varphi_{\mathbf{r}}) = \sum_{t=1}^{2}\int_0^{\infty}\sum_{n=0}^{4}\mathrm{i}^{2n}J_{2n}(\lambda\rho)\sum_{q=1}^{m_{2n}}N_{2n,q,t}(\lambda)M^{2n,q}_{i\cdots m'}(\varphi_{\mathbf{r}})\,\mathrm{d}\Phi_t(\lambda),$$

where Φ_1 and Φ_2 are two finite measures on $[0,\infty)$ satisfying the condition

$$\Phi_1(\{0\}) \geq 2\Phi_2(\{0\}).$$

Here $J_{2n}(\lambda\rho)$ are the Bessel function of the first kind of order $2n$, $m_0 = 5$, $m_2 = m_4 = 3$, $m_6 = M_8 = 1$, $N_{2n,q,t}(\lambda)$ $(0 \leq n \leq 4,\ 1 \leq q \leq m_{2n},\ t = 1, 2)$ are the functions given in Table 2 in [5], and $M^{2n,q}_{i\cdots m'}(\varphi_{\mathbf{r}})$ are tensor-valued functions similar to (4).

2. The elasticity random field $\mathsf{H}(\mathbf{x})$ has the spectral expansion

$$\begin{aligned} H_{ij\ell m}(\rho,\varphi_{\mathbf{r}}) &= C_1\delta_{ij}\delta_{\ell m} + C_2(\delta_{i\ell}\delta_{jm} + \delta_{im}\delta_{j\ell}) \\ &+ \textstyle\sum_{n=0}^{4}\sum_{q=1}^{m_{2n}}\sum_{s=0}^{\infty}\sum_{t=1}^{2}\Big(\int_0^{\infty}\sqrt{N_{2n,q,t}(\lambda)}J_s(\lambda\rho)\sin(2s\varphi_{\mathbf{r}})\,\mathrm{d}Z^{nqst-}_{ij\ell m}(\lambda) \\ &+ \int_0^{\infty}\sqrt{N_{2n,q,t}(\lambda)}J_s(\lambda\rho)\cos(2s\varphi_{\mathbf{r}})\,\mathrm{d}Z^{nqst+}_{ij\ell m}(\lambda)\Big), \end{aligned} \tag{13}$$

where the centred scattered random measures $Z^{nqst\pm}_{ij\ell m}$ are defined by

$$Z^{nqst\pm}_{ij\ell m}(A) = \sum_{(i'j'\ell'm'n'q's'\pm')\leq(ij\ell mnqs\pm)}(\mathbf{L}_t)^{i'j'\ell'm'n'q's'\pm'}_{ij\ell mnqs\pm}W^{nqst\pm}_{ij\ell m}(A),$$

where $W^{nqst\pm}_{ij\ell m}$ is the sequence of *uncorrelated* scattered random measures with Φ_t as their control measures, i.e.,

$$\mathsf{E}[W^{nqst\pm}_{ij\ell m}(A)W^{nqst\pm}_{ij\ell m}(B)] = \Phi_t(A\cap B).$$

5 TRFs Dependent Fields

5.1 Fourier Conductivity

5.1.1 Correlation of Heat Flux TRF

Consider a thermal conductivity problem in 3d: $\mathbf{q} = -\mathbf{K}\cdot\nabla T$, where the temperature T is a scalar, $\mathbf{q} = q_i\mathbf{e}_i$ is the heat flux, $\mathbf{K} = K_{ij}\mathbf{e}_i\mathbf{e}_j$ is the thermal conductivity, with $i,j = 1,2,3$; $\mathbf{e}_i$ and $\mathbf{e}_j$ are the unit vectors. Denoting the random fluctuation

about the statistical mean by $q_i^0(\mathbf{r}) = q_i(\mathbf{r}) - \mathsf{E}[q_i(\mathbf{r})]$, the correlation function of heat flux field is

$$S_i^j(\mathbf{r}) := \mathsf{E}\left[q_i^0(\mathbf{r}+\mathbf{r}_1)q_j^0(\mathbf{r}_1)\right].$$

For an isotropic field, on account of the equilibrium condition in steady-state heat conduction

$$\nabla \cdot \mathbf{q} = 0 \quad (q_{i,i} = 0),$$

and the representation (1) written as $A(r)n_in_j + B(r)\delta_{ij}$ (i.e. $A = K_2/r^2$ and $B = K_1$), we find

$$\begin{aligned} 0 = \frac{\partial S_i^j(\mathbf{r})}{\partial \xi_i} &= \frac{\partial A(r)}{\partial \xi_i}\xi_i\xi_j + A(r)\frac{\partial \xi_i}{\partial \xi_i}\xi_j + A(r)\xi_i\frac{\partial \xi_j}{\partial \xi_i} + \frac{\partial B(r)}{\partial \xi_i}\delta_{ij} \\ &= A'(r)\frac{\xi_i}{r}\xi_i\xi_j + A(r)\delta_{ii}\xi_j + A(r)\xi_i\delta_{ij} + B'(r)\frac{\xi_i}{r}\delta_{ij}, \end{aligned}$$

where the prime denotes d/dr. This implies in 2d

$$A'(r)r + 3A(r) + B'/r = 0, \tag{14}$$

and in 3d

$$A'(r)r + 4A(r) + B'/r = 0. \tag{15}$$

Recalling the continuity equation $v_{i,i} = 0$ in incompressible 3d flows, (15) agrees with Eq. (3.4.2) in Batchelor [1] for the correlation of velocity field. As briefly reviewed below, analogous constraints can be determined for correlation functions in several other TRF problems [10, 12].

5.1.2 Correlation of Temperature Gradient TRF

Denoting by $T^0{}_{,i}(\mathbf{r}) = T_{,i}(\mathbf{r}) - \mathsf{E}[T_{,i}(\mathbf{r})]$ the random fluctuation of temperature gradient about its mean $\mathsf{E}[T_{,i}(\mathbf{r})]$, we have

$$E^j_{i,k}(\mathbf{r}) = \mathsf{E}\left[T^0{}_{,i}(\mathbf{r}+\mathbf{r}_1)T^0{}_{,j}(\mathbf{r}_1)\right]_{,k} = \mathsf{E}\left[T^0_{,k}(\mathbf{r}+\mathbf{r}_1)T^0{}_{,j}(\mathbf{r}_1)\right]_{,i} = E^j_{k,i}(\mathbf{r}),$$

from which we obtain the condition

$$C(r) = D'(r)r. \tag{16}$$

5.2 *Anti-plane Elasticity*

5.2.1 Correlation of Stress TRF

In the anti-plane elasticity problem, the second-rank stress and strain tensors can be mapped into vectors as

$$\sigma_i = \sigma_{i3}, \quad \varepsilon_i = \varepsilon_{i3}, \quad i = 1, 2,$$

so that the Hooke law reads

$$\begin{Bmatrix} \sigma_1 \\ \sigma_2 \end{Bmatrix} = \begin{bmatrix} \tilde{C}_{11} & \tilde{C}_{12} \\ \tilde{C}_{21} & \tilde{C}_{22} \end{bmatrix} \begin{Bmatrix} 2\varepsilon_1 \\ 2\varepsilon_2 \end{Bmatrix} \quad \text{or} \quad \sigma_i = \tilde{C}_{ij} 2\varepsilon_j,$$

with $\tilde{C}_{11} = C_{44}$, $\tilde{C}_{22} = C_{55}$, whereas the symmetry of $\tilde{C}_{ij}$ implies: $\tilde{C}_{12} = C_{54}$, $\tilde{C}_{21} = C_{45}$. Also, we use the position vector $\mathbf{r} = (x_1, x_2)$, with $r = \sqrt{\mathbf{r} \cdot \mathbf{r}}$. Incidentally, this model is mathematically equivalent to planar heat conduction.

Now, define the correlation function of a zero-mean stress field

$$S_i^j(\mathbf{r}) := \mathsf{E}\left[\sigma_i^0(\mathbf{r} + \mathbf{r}_1)\sigma_j^0(\mathbf{r}_1)\right], \quad i = 1, 2,$$

where $\sigma_i^0(\mathbf{r}) = \sigma_i(\mathbf{r}) - \mathsf{E}[\sigma_i(\mathbf{r})]$ is the random fluctuation of stress field about its mean $\mathsf{E}[\sigma_i(\mathbf{r})]$. The static equilibrium in 3d implies

$$\sigma_{i,i}(\mathbf{r}) = 0,$$

so that

$$S_{i,i}^j(\mathbf{r}) = 0. \tag{17}$$

For the isotropic second-rank tensor, again in view of (1), we can write

$$S_i^j(\mathbf{r}) = A(r) n_i n_j + B(r)\delta_{ij},$$

so that, for $j = 1, 2$, we have

$$0 = \frac{\partial S_i^j(\mathbf{r})}{\partial x_i} = A'(r) n_i n_i n_j + A(r) n_j / r + B'(r) n_i \delta_{ij},$$

where the prime denotes d/dr. That is

$$A'(r) + A(r)/r + B' = 0. \tag{18}$$

5.2.2 Correlation of Strain TRF

Turning to the strain field, define the second-rank tensor

$$E_i^j(\mathbf{r}) := \mathsf{E}\left[\epsilon_i^0(\mathbf{r}+\mathbf{r}_1)\epsilon_j^0(\mathbf{r}_1)\right],$$

where $\epsilon_i^0(\mathbf{r}) = \epsilon_i(\mathbf{r}) - \mathsf{E}\left[\epsilon_i(\mathbf{r})\right]$. For the anti-plane problem, $u_3(\mathbf{r}) \neq 0$ and $u_1(\mathbf{r}) = u_2(\mathbf{r}) = 0$ for $\forall \mathbf{r}$. From the strain-displacement compatibility $\epsilon_{ij} = u_{(i,j)}$ we observe that

$$E_i^j(\mathbf{r}) = -\frac{1}{4}\frac{\partial^2 U_{33}}{\partial x_i \partial x_j}, \tag{19}$$

where $U_{33}(\mathbf{r}) = \mathsf{E}\left[u_3^0(\mathbf{r}+\mathbf{r}_1)u_3^0(\mathbf{r}_1)\right]$ with $u_3^0(\mathbf{r}) = u_3(\mathbf{r}) - \mathsf{E}\left[u_3(\mathbf{r})\right]$. This implies

$$E_1^1(r) = -\frac{1}{4}\frac{\partial^2 U_{33}}{\partial x_1^2}\ E_1^2(r) = -\frac{1}{4}\frac{\partial^2 U_{33}}{\partial x_1 \partial x_2}\ E_2^2(r) = -\frac{1}{4}\frac{\partial^2 U_{33}}{\partial x_2^2},$$

so that

$$\frac{\partial E_1^1(r)}{\partial x_2} = \frac{\partial E_1^2(r)}{\partial x_1},\ \frac{\partial E_2^2(r)}{\partial x_1} = \frac{\partial E_1^2(r)}{\partial x_2}.$$

Taking $E_i^j(\mathbf{r})$ to be a statistically isotropic tensor, and setting $C = K_2/r^2$ and $D = K_1$, we can write its representation (1) as

$$E_i^j(\mathbf{r}) = C(r)n_i n_j + D(r)\delta_{ij}.$$

The relations between the gradients of correlations of strain field imply

$$\begin{aligned} C'n_2n_1^2 - 2Cn_{112}/r + D'n_2 &= C'n_1n_1n_2 + C(n_2 - 2n_{112})/r, \\ C'n_1n_2^2 - 2Cn_{221}/r + D'n_1 &= C'n_2n_1n_2 + C(n_1 - 2n_{212})/r, \end{aligned}$$

resulting in

$$C = D'r. \tag{20}$$

5.3 3d Classical Elasticity

First, we note that, in view of $\varepsilon_{ij} = u_{(i,j)}$, ε_{ij} is a potential tensor field, with u_i being its potential. On the other hand, the balance of linear momentum in the absence of body forces $\sigma_{ij,j} = 0$, indicates that σ_{ij} is birotational.

5.3.1 Correlation of Stress TRF

For the in-plane elasticity problem, the Hooke law reads

$$\sigma_{ij} = \tilde{C}_{ijkl}\varepsilon_{kl}, \quad i,j,k,l = 1,2.$$

Now, the correlation function of the zero-mean stress field

$$S_{ij}^{kl}(\mathbf{r}) := \mathsf{E}\left[\sigma_{ij}^0(\mathbf{r}+\mathbf{r}_1)\sigma_{kl}^0(\mathbf{r}_1)\right], \quad i,j,k,l = 1,2,3,$$

where $\sigma_{ij}^0(\mathbf{r}) = \sigma_{ij}(\mathbf{r}) - \mathsf{E}\left[\sigma_{ij}(\mathbf{r})\right]$, on account of the static equilibrium, leads to

$$S_{ij,j}^{kl}(\mathbf{r}) = 0.$$

Assuming $S_{ij}^{kl}(\mathbf{r})$ to be a statistically isotropic TRF, its representation is (2), which leads to a system of three differential equations

$$\begin{aligned} 8S_{11}^{11} &= (R+2)(R+4)S_{22}^{22} \\ 4S_{12}^{12} &= (R+2)S_{22}^{22} - 2S_{11}^{22} \\ 8S_{22}^{33} &= 8(R+1)S_{11}^{22} - R(R+2)S_{22}^{22} \end{aligned} \qquad R \equiv r\frac{d}{dr}. \tag{21}$$

This implies that S_{22}^{22} and S_{11}^{22} should be chosen first (i.e. before other S_{ij}^{kl}) in modeling such a stress TRF.

5.3.2 Correlations of Strain, Rotation, and Curvature-Torsion TRFs

Consider a correlation function of a second-rank TRF of strain

$$E_{ij}^{kl}(\mathbf{x}_1,\mathbf{x}_2) := \mathsf{E}\langle\left[\varepsilon_{ij}(\mathbf{x}_1)\varepsilon_{kl}(\mathbf{x}_2)\right],$$

and also a correlation tensor of the displacement field

$$U_i^j(\mathbf{x}_1,\mathbf{x}_2) := \mathsf{E}\left[u_i(\mathbf{x}_1)u_j(\mathbf{x}_2)\right].$$

Assuming homogeneity, we have $U_i^j(\mathbf{x}_1 - \mathbf{x}_2)$, so that, on account of the strain displacement relation and using a slightly different notation $U_{ij}(\mathbf{x}) \equiv U_i^j(\mathbf{x})$, we can write

$$E_{ij}^{kl} = -\nabla_{(i}U_{i)(k,l)}.$$

In view of the representations (1) and (2) for U_i^j and E_{ij}^{kl} when both TRFs are taken as isotropic, Shermergor [12] obtained a system of three differential equations

$$\begin{aligned} E_{22}^{22} &= (R+1)E_{11}^{11} + R(R+1)E_{22}^{33} \\ E_{12}^{12} &= (R+2)E_{11}^{11} + (R-2)E_{22}^{33} \\ E_{11}^{22} &= (R+1)E_{22}^{33} \end{aligned} \quad R \equiv r\frac{d}{dr}, \tag{22}$$

implying that E_{11}^{11} and E_{22}^{33} should be chosen first (i.e. before other E_{ij}^{kl}). Once the correlation tensors of stress and strain fields are known, one can also assess the field of rotations of grains.

Proceeding in the same manner, one can consider TRFs in micropolar linear elasticity, so as to establish similar restrictions on asymmetric force and couple stress fields as well as those on displacement, rotation, and strain fields.

6 Conclusion

This article reports progress on homogeneous isotropic TRFs for continuum mechanics. The basic thrust is on determining most general representations of correlation functions such as (1), (2) and (5), as well as their spectral expansions such as (12) and (13). The second step is finding the restrictions dictated by a particular physical application. Thus, in the case of fields of material properties (like conductivity and stiffness), the restriction resides in the positive-definiteness, whereby (6)–(11) give a connection to experiments and/or computational micromechanics. On the other hand, in the case of fields of dependent properties (e.g., stress, strain and displacement), restrictions (14)–(22) are due to the respective field equations.

References

1. Batchelor GK (1953) The theory of homogeneous turbulence. In: Cambridge monographs on mechanics and applied mathematics. Cambridge University Press, Cambridge
2. Lomakin VA (1964) Statistical description of the stressed state of a body under deformation. Dokl Akad Nauk SSSR 155:1274–1277
3. Lomakin VA (1965) Deformation of microscopically nonhomogeneous elastic bodies. Appl Math Mech 29(5):888–893
4. Malyarenko A (2013) Invariant random fields on spaces with a group action. In: Probability and its applications. Springer, Heidelberg. doi:10.1007/978-3-642-33406-1. http://dx.doi.org/10.1007/978-3-642-33406-1
5. Malyarenko A, Ostoja-Starzewski M (2014) The spectral expansion of the elasticity random field. In: Sivasundaram S (ed) 10th international conference on mathematical problems in engineering, aerospace, and sciences (ICNPAA 2014). AIP conference proceedings, vol 1637, Narvik, 15–18 July 2014, pp 647–655. doi:10.1063/1.4904635
6. Malyarenko A, Ostoja-Starzewski M (2014) Spectral expansions of homogeneous and isotropic tensor-valued random fields. http://arxiv.org/abs/1402.1648

7. Malyarenko A, Ostoja-Starzewski M (2014) Statistically isotropic tensor random fields: correlation structures. Math Mech Complex Syst 2(2):209–231
8. Monin AS, Yaglom AM (2007) Statistical fluid mechanics: mechanics of turbulence, vol II. Dover, Mineola
9. Ostoja-Starzewski M (2008) Microstructural randomness and scaling in mechanics of materials. CRC series: modern mechanics and mathematics. Chapman & Hall/CRC, Boca Raton
10. Ostoja-Starzewski M, Shen L, Malyarenko A (2015) Tensor random fields in conductivity and classical or microcontinuum theories. Math Mech Solids 20(4):418–432. doi:10.1177/1081286513498524
11. Robertson HP (1940) The invariant theory of isotropic turbulence. Proc Camb Philos Soc 36:209–223
12. Shermergor T (1971) Relations between the components of the correlation functions of an elastic field. Appl Math Mech 35(3):432–437
13. Spencer A (1971) Theory of invariants. In: Continuum physics, vol 1. Academic, New York, pp 239–353
14. Taylor G (1935) Statistical theory of turbulence. Proc R Soc A 151:421–478
15. von Kármán T, Horwath L (1938) On the statistical theory of isotropic turbulence. Proc R Soc A 164:192–215
16. Yaglom AM (1957) Certain types of random fields in n-dimensional space similar to stationary stochastic processes. Teor Veroyatnost i Primenen 2:292–338

Designing Particulate Composites: The Effect of Variability of Filler Properties and Filler Spatial Distribution

Catalin R. Picu, Stefan Sorohan, Monica A. Soare, and Dan M. Constantinescu

Abstract A new perspective on structural design of particulate composites is presented in this chapter. The central concept is that by controlling multiple parameters describing the stochastic microstructure, such as allowing the filler properties to vary from filler to filler, or constructing spatially correlated filler distributions, significantly expands the design space which, in turn, is likely to lead to the development of more performant composites. We investigate the effect of two such parameters on the elastic-plastic and damping behavior of the composite. First, we consider microstructures containing fillers of same properties but which are spatially distributed in a correlated way. It is observed that composites with spatially correlated filler distributions are stiffer, strain harden more and lead to larger damping ratios relative to microstructures with random, uncorrelated filler distributions of same volume fraction. In the second part of the study we consider composites in which filler properties vary from filler to filler. It is observed that the composite modulus and its strain hardening rate decrease as the variance of the probability distribution function of filler elastic constants increases, while the mean of the distribution is kept constant. The damping ratio of the composite is not sensitive to the higher moments of the distribution function of damping coefficients within inclusions.

C.R. Picu (✉)
Department of Mechanical, Aerospace and Nuclear Engineering, Rensselaer Polytechnic Institute, Troy, NY 12180, USA
e-mail: picuc@rpi.edu

S. Sorohan • D.M. Constantinescu
Department of Strength of Materials, University POLITEHNICA of Bucharest, Bucharest, Romania
e-mail: stefan.sorohan@upb.ro; dan.constantinescu@upb.ro

M.A. Soare (✉)
General Electric Global Research, Niskayuna, NY 12309, USA
e-mail: soare@ge.com

P. Trovalusci (ed.), *Materials with Internal Structure*, Springer Tracts in Mechanical Engineering, DOI 10.1007/978-3-319-21494-8_7

1 Introduction

Structural composites are a broad class of materials with increasing range of applications and market share. These are made from several constituents distributed spatially in pre-defined ways. Particulate composites are typically made by dispersing a filler phase in a matrix. Fiber composites are constructed either in a manner similar to particulate composites, by distributing short fibers at random in a matrix, or by weaving long fibers in pre-defined patterns and embedding the resulting plies in the matrix. Woven and non-woven composites have significantly different properties. For example, woven carbon fiber composites are highly anisotropic, while short fiber reinforced plastics, e.g., fiberglass, are isotropic on the macroscopic scale [1].

Most biological materials are composites. Bone is a hierarchically structured mixture of mineral (hydroxyapatite) and proteins [2] and, based on the classification mentioned above can be considered a particulate composite since the mineral phase is discontinuous. Most types of soft tissue are made from long fibers of collagen and elastin which form the extracellular strength-providing structure, embedded in a "matrix" made from cells, water, and large molecules [3].

The distribution of the reinforcing phase in man-made composites is either random or regular. Random distributions result by simply mixing the filler phase in the matrix, followed by matrix solidification. The actual filler distribution is not controlled in any particular way and agglomeration may occur. In woven composites the microstructure is more regular as the reinforcing fiber bundles are placed in pre-defined patterns. Furthermore, the stacking of fibrous plies is also controlled to insure unidirectional, bi-directional or isotropic in-plane stiffness and strength.

Regular microstructures are only a designer concept since variability introduced by the manufacturing methods unavoidably leads to some degree of randomness of the structure even in the most controlled cases. Specifically, in woven composites fiber bundles do not contain exactly the same number of fibers and the weaves are not identical down to the micrometer scale. Clearly, biological materials are stochastic and have some degree of regularity only in the average sense.

Design of composite materials usually does not account for variability. In fact, in composites with regular microstructure, variability is undesirable and is considered to lead to premature damage nucleation and failure. Therefore, standard composite design and manufacturing aims to minimize structural variability such to, presumably, maximize macroscopic properties. In manufacturing of composites with random distribution of reinforcements, it is usually sought to create truly random microstructures and any clustering is considered undesirable.

Likewise, poor dispersion and/or distribution of fillers is considered the key reason for poor performance of nanocomposite materials [4]. In these cases, nanoscale fillers, such as nanoparticles and nanofilaments, are dispersed in a polymer matrix. The interesting properties of these composites result from the "interphase" polymer layer, i.e., the region of the polymeric matrix located in the close vicinity of the filler surface. This volume of polymer has modified physical properties due to the

confinement constraint imposed by the presence of the filler. In nanocomposite manufacturing, a distribution of fillers that allows for these modified polymer layers to percolate through the volume of the composite is considered ideal. In such cases, the unusual properties of the interphase become measurable on the macroscale. Let us note that this, by now customary, concept does not require the fillers spatial distribution to be uniform. In fact, percolated paths of fillers may lead to the desired macroscopic effects, and this is used in automobile tires, which are nanocomposites of carbon black particles dispersed in rubber [5].

At the current stage of development of the composite technology, and particularly with the advent of additive manufacturing which makes possible the fabrication of composites with precise control of the microstructure, it is useful to inquire about the validity of the established concept that keeping variability to a minimum leads to optimal macroscopic properties of composites. These emerging technologies offer new ways to build such materials and a much broader design space over which property optimization can be performed.

1.1 Structural Stochasticity in Composite Materials and Formulation of the Problem

Stochasticity influences the material behavior in multiple ways. The most obvious source of stochasticity are thermal fluctuations which are prevalent on the nanoscale. The effect of these fluctuations is observed often on the macroscopic scale, an example being the strain rate sensitivity of engineering materials [6]. The dependence of the flow stress on the deformation strain rate is due to thermal activation of nanoscale deformation processes, which is controlled by thermal fluctuations. Creep and slow crack growth are also phenomena controlled by thermal activation which therefore inherit the effect of small-scale fluctuations.

Kinetics of a process evolving on a complex energy surface is stochastic. Kinetics is driven by thermal fluctuations, but is controlled by the shape of the energy surface of the system. Since such energy landscapes are defined in a multidimensional space and have complex geometries with many minima and many barriers of similar height, the path taken by a system may be highly degenerate. The system can take a range of phase space trajectories which correspond in physical space to diverse sets of successive configurations.

One of the main sources of stochasticity in composites is structural. To outline the central idea of this chapter, let us consider the simplest particulate composite possible: a mixture of a matrix, phase A, and inclusions, phase B. The two phases have different material properties. The problem is defined identically in 2D (films, membranes) and in 3D (bulk). In standard composite design, the central parameter in such cases is the volume fraction of phase B, f_B.

Here we propose to expand the design phase space by considering ways to introduce stochasticity in this problem. Once the problem is defined, the effect of

the various parameters describing structural stochasticity will be analyzed. In order to focus on these parameters, it is useful to keep the volume fraction constant for the reminder of the discussion.

Stochastic microstructures can be generated by considering that one (or multiple) of the material properties, say Young's modulus, is defined as $E(\mathbf{x}, \xi)$, i.e., it is a function of position, which is a deterministic variable, $\mathbf{x}$, and of a stochastic variable, ξ. The distribution function p(E) can be specified in terms of a set of parameters such as, for example, a finite number of its moments. Let us denote these moments as m_E. In the usual case, in which all inclusions are made from the same material, p(E) is composed from two delta functions located at the values of Young's modulus of phases A and B, respectively. In general, inclusions of different types can be considered and p(E) may have any functional form.

The size and shape of inclusions may be also considered stochastic variables and likewise may be defined by distribution functions described by a finite set of moments, m_S. Particles may be randomly distributed in the matrix, or distributed in a spatially correlated way. This property can be described by using the two-point autocorrelation function $ACF(\mathbf{y}) = E(\mathbf{x}+\mathbf{y})E(\mathbf{x})_{\xi}$, where the average $< >$ is taken over multiple origins and replicas, ξ. Multipoint correlation functions can also be used for this purpose. ACF includes the information about the size and shape of inclusions in an averaged way. If vectors $\mathbf{x}$ and $\mathbf{y}$ are sampled on a scale comparable with or larger than the inclusion size, ACF loses the particle size information. In this limit and for a random composite, the ACF becomes a delta function. Most real microstructures are not perfectly random and have some degree of clustering. Then, the ACF function is longer ranged. The characteristic correlation length λ associated with ACF defines the mean cluster size.

Let us collect all variables defining these distributions and correlation functions into a vector, $\mathbf{v} = \{m_E, m_S, \lambda\}$. These variables define the space of stochastic variables over which composite properties should be explored and optimized.

To render the discussion specific, let us consider the two types of 2D (plane strain) microstructures shown in Fig. 1. These have randomly distributed inclusions (Fig. 1a) and inclusions which are distributed in a spatially correlated way (Fig. 1b). The spatial correlation, ACF, is exponential in this case and does not depend on the direction, i.e., $ACF(\mathbf{y})$, is only a function of the modulus of vector $\boldsymbol{y}$. This renders the material isotropic. Figure 1c shows the autocorrelation functions for the two realizations, with the variable y sampled with resolution ε which is taken to be equal to the size of inclusions. All inclusions are of the same size in this problem. The random microstructure is delta correlated and hence no parameter is needed to describe its ACF. The correlated microstructure has a characteristic correlation length λ. Since all inclusions are of the same size, the distribution function of inclusion sizes is also a delta function and set m_S is empty. One of the material properties of inclusions is considered a stochastic variable. For example, Young's modulus of inclusions is sampled from a log-normal distribution. Figure 2 shows p(E) for this case, with the modulus of phase A (matrix) being set at $E = 1$, and the mean of the phase B modulus being set at 6. The coefficient of variance of the phase B modulus is 0.3 in this example. Set m_E includes the mean of phase B

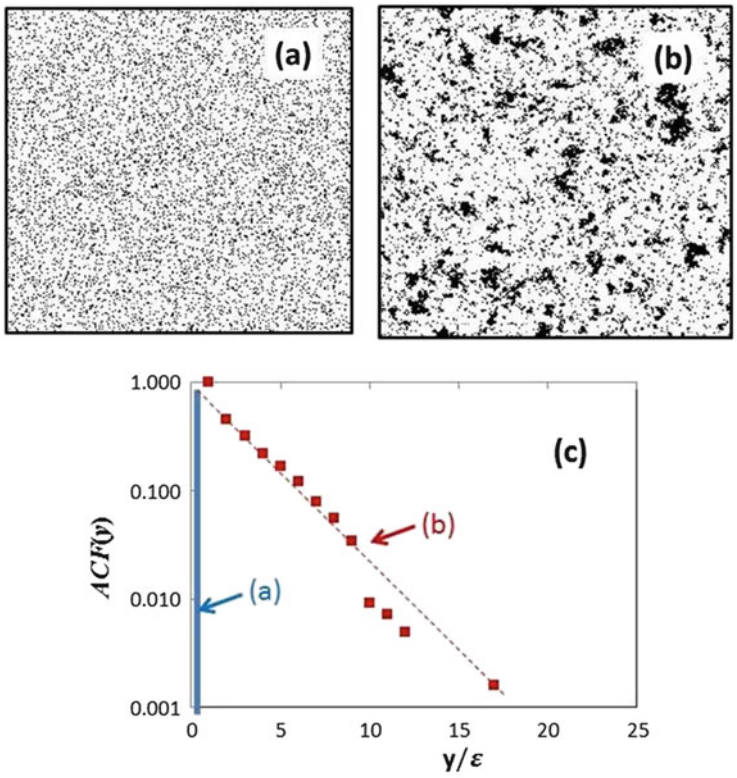

Fig. 1 Realizations of particulate composites with (**a**) random and (**b**) exponentially correlated distributions of fillers. The autocorrelation function for the microstructures in (**a**) and (**b**) are shown in (**c**)

modulus (normalized by the modulus of phase A), and the coefficient of variance of the distribution of Phase B modulus: $m_E = \{\overline{E}_B, \sigma_B/\overline{E}_B\}$. In Sects. 3 and 4 of this chapter, we explore the effect of parameters in set $\mathbf{v} = \{m_E, \lambda\}$ on the macroscopic properties of the composite, in particular on the elastic-plastic and damping responses.

1.2 Background

The problem of microstructural design of composites is usually not defined in terms of the variables describing the stochasticity of the microstructure. An exception is the effect of the distribution of inclusions, or parameter λ defined above, which has been considered in a number of works. Let us note that if the composite is made from

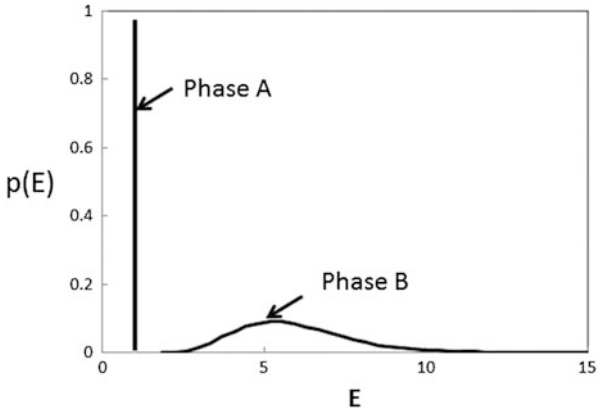

Fig. 2 Probability distribution functions for matrix (phase A) and inclusions (phase B) properties. In this design filler properties are allowed to vary from filler to filler in the same realization of the composite

two materials, A and B, and all fillers are identical, the filler distribution/dispersion is the only stochastic variable.

Reviews on the homogenization of random composites are presented in [7–9]. Remarkable results have been obtained regarding the bounds on the elastic moduli of such composites. These expressions are generally given in terms of the volume fraction of the constituents. The closest bounds for the bulk modulus which take into account only the volume fraction have been derived by Hashin and Shtrikman [10]. A family of higher order bounds, which take into account statistical measures of the microstructure geometry, have been proposed more recently with the purpose of reducing the separation between the upper and lower bounds (e.g., [11–16]). The n-point bounds are written in terms of n-point microstructural correlation functions which define the probability that n points with specified relative positions are all located in a certain phase of the composite. A review of the higher order bounds and the geometric parameters required for their evaluation is provided in [8].

A particularly interesting type of microstructure is that in which fillers form a fractal structure. This differs from the cases discussed in the publications mentioned above through the fact that ACF is a power function of y. The upper and lower scales that bound the range of self-similar scaling are the size of the composite sample and the size of individual fillers, respectively. The power law ACF lacks a characteristic length scale and hence, correlations extend throughout the entire composite domain. The rate of decay of the correlation function, or the exponent of the power function, depends on the fractal dimension. A particularly interesting aspect of such problems is the fact that size effects are inherent in the definition of the microstructure. This follows from the lack of characteristic length scale of the microstructure; its spatial correlations extend to the boundaries of the problem domain. The usual wisdom in composites is that design should be performed at scales large enough for the size effect to be absent or negligible. This is not possible when the microstructure

is fractal. However, such situations offer the possibility to take advantage of the inherent size effect to enhance the properties of interest.

The elastic moduli of deterministic fractal structures have been predicted using standard finite element models and renormalization group concepts [17]. Dyskin applied the differential self-consistent method (initiated in [18]) for media containing self-similar distributions of spherical/ellipsoidal pores or cracks [19]. Tarasov studied porous materials having pores with a broad range of sizes and in which the mass of the material within a volume of dimension R scales as $m(R) \prec R^Q$, with Q non-integer [20, 21]. This method was further developed recently in [22, 23] to represent the mechanics of heterogeneous bodies with fractal microstructure. Carpinteri et al. studied the deformation of a bar in which the strain is localized in a subset of cross-sections forming a Cantor set [24]. These authors use fractional operators to rewrite the balance equations, although in one dimension this is not immediately necessary. The deformation of a two-dimensional composite with Cantor-like inclusion distribution was studied in [25]. In [26] fractional calculus based on local fractional operators introduced by Kolwankar and Gangal [27, 28] were used to formulate the balance equations on the fractal support. The formulation was applied to modeling the deformation of two-dimensional composites containing a fractal distribution of inclusions in a matrix.

In [29], the mechanical behavior of particulate composites with fractal microstructure was compared with that of composites with random and exponentially correlated microstructures of identical volume fraction and filler size. It was concluded that strong spatial correlations (as in the fractal case) have a weak effect on the elastic-plastic response, but a strong effect on cavitation and damping behavior. Section 3 of this chapter is based in part on results presented in reference [29].

2 Models and Methods

In this section we review the methods used in this work to solve mechanics boundary value problems defined on domains with stochastic microstructure. The objective of solving such problems is to infer the fields (stress, strain) over the entire problem domain. The fields are used to evaluate a property of interest (PoI) whose optimum is sought. These methods can be used to solve other types of problems as well, including transport and electromagnetic problems.

The PoI is a generic quantity which is evaluated based on the solution. It can be expressed in the integral sense as a mean, or it can be related to the value of the fields at specified locations. For example, the PoI can be the average modulus of the composite, case in which it is defined as the ratio of the mean stress to the mean strain, which are integral quantities. In fatigue or other problems in which damage nucleation and growth are important, the PoI can be the maximum values of the stress distribution. In this case, the PoI is evaluated based on the tails of the distribution function of stress field values.

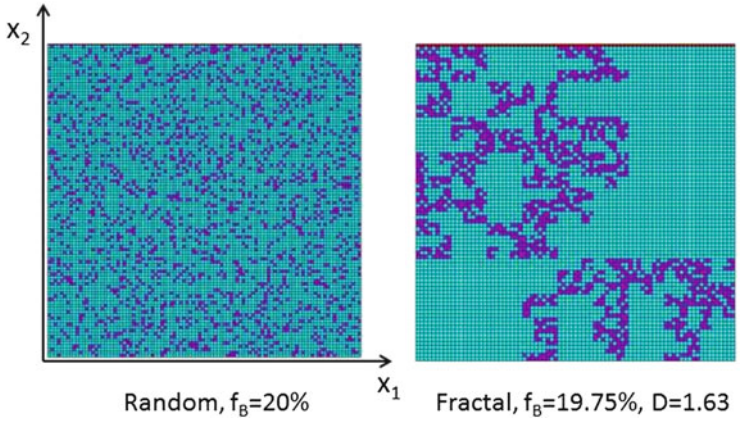

Fig. 3 Models of a composite with (**a**) uncorrelated and with (**b**) power law correlated (fractal) distribution of fillers. The meshes shown are coarser than used in the simulation to allow visualization

Two PoI, both of integral form, are used in this discussion: the stress-strain behavior of the composite, and its damping response. The stress-strain curve is obtained by loading the composite in uniaxial tension in direction x_2 (Fig. 3) under displacement control, with free boundaries in the direction perpendicular to the loading direction. To study the damping response, a similar uniaxial deformation is considered. The motion of the system in free vibrations is represented by

$$\mathbf{M\ddot{u}} + \mathbf{C\dot{u}} + \mathbf{Ku} = \mathbf{0} \tag{1}$$

where **M**, **C,** and **K** are the mass, damping, and stiffness matrices. In these models it is considered that damping takes place within inclusions, while the matrix is linear elastic without damping.

In the modal analysis, the solution of this system of equations is sought in the form $u = \varphi \exp(ht)$, where the eigenvalues h are (for the undamped modes) complex conjugates, $h_j = s_j + i\omega_j$, with j representing the index of the respective eigenvalue. s_j characterizes the damping factor on the scale of the composite, while ω_j is the damped frequency. The parameter of interest here is the damping ratio,

$$\xi_j = -\frac{s_j}{\sqrt{s_j^2 + \varpi_j^2}} \tag{2}$$

which indicates the damping of mode j relative to the critical damping. We focus on, ξ_1, the damping ratio corresponding to the axial vibration mode of the structure.

Figure 3 shows two of the models used. Figure 3a shows a model with random microstructure and filler volume fraction $f_B = 20$ %, while Fig. 3b shows a model with fractal microstructure and approximately the same filler volume fraction,

$f_B = 19.75$ %. The fractal dimension of the model in (b) is $D = 1.63$. Both models are shown with a rather coarse mesh to facilitate visualization. The real mesh used in simulations had at least four elements per filler, even for the fractal structures with finest resolution.

The fractal microstructures are generated based on the Cantor set in 2D. The microstructure is constructed hierarchically by iteratively applying a set of transformation rules. The first generation is obtained by starting with an Euclidean domain, dividing it in M equal cells and selecting randomly P of them which are to be filled with the inclusion material, B. The characteristic size of these cells is ε_1. The number of possible configurations at the first step of the generation process is $M!/\left(P!\left(M-P\right)!\right)$. The next generations are obtained by dividing again each of the B material cells in M equal parts from which M-P are transformed into matrix cells, A. At any step of the generation, the problem domain is composed from M^n cells of characteristic dimension ε_n of which P^n are occupied by the inclusion material, phase B. The remaining M^n- P^n cells are occupied by the matrix material, phase A. The dimension of the resulting fractal microstructure is evaluated as $D = 2\log(P)/\log(M)$. Obviously, many realizations of the microstructure are possible. The number of possible configurations at iteration (or scale) n is $[M!/\left(P!\left(M-P\right)!\right)]^{p^{n-1}+\cdots+p+1}$. The microstructure shown in Fig. 3b corresponds to the set with $M = 9$, $P = 6$, and fractal generation step $n = 4$.

The solution of the boundary value problems described above can be obtained in several ways. In addition to Monte Carlo (MC) methods [30], various systematic ways of approaching numerically partial differential equations defined on single-scale stochastic domains were proposed in the literature. Methods based on probabilistic finite elements (second order perturbation PFEM) [31, 32], or the spectral approach for stochastic finite elements (SSFEM) [33] are relevant examples. These methods were applied to various problems in solid and fluid mechanics such as to study transport through porous media [34] and elastic deformation [35]. The elastic deformation of composites with fractal microstructure was represented using the stochastic finite element method in [36] based on an approximation of the spectral decomposition of the representation of the fractal microstructure presented in [37].

In this work we use a Monte Carlo type method in which many replicas of the system are generated and solved independently under the same boundary conditions. In all examples shown in the next sections, between 60 and 100 replicas are considered for each case. For fractal structures we also use a method similar to that presented in [36], which is based on the stochastic finite element method [33] and the spectral decomposition of the covariance matrix of the stiffness presented in [37]. For completeness, this second method is briefly reviewed here. The Monte Carlo method does not require further discussion.

The balance equations can be cast in the variational form:

$$\left\langle \int_{\widehat{D}} u_{i,j}\left(\mathbf{x},\boldsymbol{\zeta}\right) L_{ijkl}^{-1}\left(\mathbf{x},\boldsymbol{\zeta}\right) v_{k,l}\left(\mathbf{x},\boldsymbol{\zeta}\right) dx \right\rangle = \left\langle \int_{\Gamma} t_i^0 v_i\left(s,\boldsymbol{\zeta}\right) ds \right\rangle \tag{3}$$

where $\mathbf{u}$ is the displacement field defined over the entire problem domain, $\hat{D}$, $\boldsymbol{v}$ is a probing field, $\mathbf{t}$ are tractions acting along the boundary Γ of domain $\hat{D}$, and $\mathbf{L}$ is the stiffness tensor. The stiffness depends on position, $\mathbf{x}$, and a stochastic variable, ζ. This represents the fact that the position of inclusions is stochastic. The random position of inclusions which leads to the stochastic nature of $\mathbf{L}$ also implies that the solution, $\mathbf{u}$, is stochastic. The variational form is written in the average sense with the average $< >$ being taken over the random variable ζ. The equality in Eq. (3) should hold for any probing field $\boldsymbol{v}(\mathrm{x}, \zeta)$.

Equation (3) is solved using a procedure similar to that of the usual finite elements. The deterministic part of the solution is approximated using a set of generic shape functions $\boldsymbol{N_m}(\mathbf{x})$. The stochastic component of the solution is approximated by a superposition of chaos polynomials $\psi_{\boldsymbol{q}}(\boldsymbol{\zeta})$ [38] having the orthogonality property $< \psi_{\boldsymbol{i}}(\boldsymbol{\zeta})\, \psi_{\boldsymbol{j}}(\boldsymbol{\zeta}) >= \boldsymbol{\delta_{ij}}$. In the probabilistic space, the chaos polynomials play the role Hermite polynomials have in the deterministic space [39, 40]. The decomposition in chaos polynomials is generally used as an alternative to the Karhunen–Loève decomposition in situations in which the covariance is not known a priori, which is the case here with the solution $\mathbf{u}$.

The approximation of the displacement field is written in the separable form:

$$\mathbf{u}(\mathbf{x}, \boldsymbol{\zeta}) = \sum_m \sum_q \mathbf{u}^{mq} \mathbf{N}_m(\mathbf{x})\, \psi_q(\boldsymbol{\zeta}) \tag{4}$$

such that finding the solution amounts to identifying the set of coefficients $\mathbf{u}^{\boldsymbol{mq}}$.

The stiffness tensor is written as a Karhunen–Loève decomposition [41–43]. According to this, the random field is written as:

$$\mathbf{L}(\mathbf{x}, \boldsymbol{\zeta}) = \langle \mathbf{L}(\mathbf{x}, \boldsymbol{\zeta}) \rangle_{\zeta} + \sum_k \sqrt{\boldsymbol{\alpha}^{(k)}}\, \vartheta^{(k)}(\boldsymbol{\zeta})\, \mathbf{F}^{(k)}(\mathbf{x}) \tag{5}$$

where $\boldsymbol{\alpha}^{(\boldsymbol{k})}$ and $\mathbf{F}^{(\boldsymbol{k})}$ are the eigenvalues and eigenvectors of the covariance of $\mathbf{L}$, and $\vartheta^{(\boldsymbol{k})}$ is a set of random variables of mean zero, which are uncorrelated but not necessarily independent.

The discrete solution (4) and the expansion (5) are replaced in Eq. (3) and test functions of the form $v_i(\mathrm{x}, \zeta) = N_i(\mathrm{x})\, \psi(\zeta)$ are used. The average operator is switched with the integral operator and applied directly to the integrand. The resulting average can be treated analytically for a finite number of terms in (5). The remaining terms on the left hand side of (3) produce a stiffness matrix which is independent of stochastic parameters. The right hand side of (3) represents the deterministic boundary conditions and is also independent of the stochastic variable after averaging. Therefore, problem (3) reduces to a deterministic system of equations which is solved once for the unknown coefficients $\mathbf{u}^{\boldsymbol{mq}}$ of Eq. (4). The solution of this system of equations leads to the mean and variance of the field $\mathbf{u}$. Further details are found in the publications referenced above.

3 Effect of Filler Distribution

Let us analyze first the effect of the non-uniform spatial distribution of fillers at constant filler volume fraction on the response to monotonic deformation and to vibrations of structures of the type shown in Figs. 1 and 3 [29].

3.1 The Elastic-Plastic Behavior

As discussed above, composites with an elastic-plastic matrix and linear elastic inclusions are considered. The matrix constitutive behavior is bilinear, with Young's modulus E_1 and constant tangent stiffness in the plastic range equal to $E_1/10$. Inclusions are identical, with Young's modulus six times larger than that of the matrix, $E_2/E_1 = 6$. The matrix and inclusions have the same Poisson ratio, equal to 0.3. Inclusions are distributed uncorrelated (random) or in a correlated way, with spatial correlations ACF(y) either of exponential or power law form. The exponential ACF(y) has a characteristic length scale, while the power law correlations, which characterize fractal structures, lack a characteristic length scale.

It results from the analysis that the effective behavior of the composite is also bilinear and can be characterized by two moduli, one describing the elastic range, E_e, and the other representing the tangent stiffness in the plastic range, E_p. Figure 4 shows the stress-strain curves corresponding to two composites with fractal microstructures (filled symbols) and composites with random microstructure

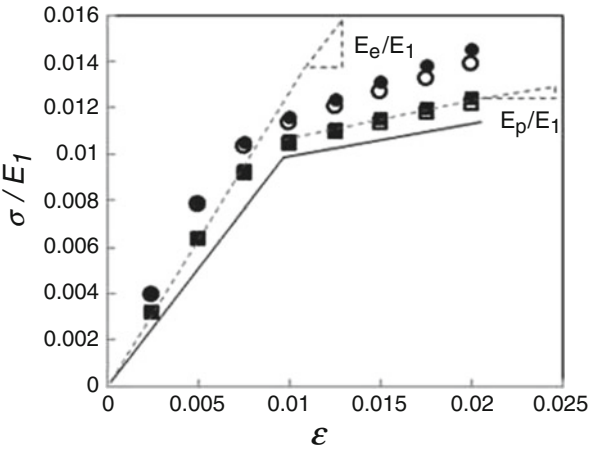

Fig. 4 Stress-strain curves for composites with fractal microstructure (*filled symbols*) and random microstructures of same volume fraction (*open symbols*), with $M = 9$, $P = 5$, $n = 2$ (*circles*) and $M = 9$, $P = 5$, $n = 3$ (*squares*). The *continuous line* represents the mechanical behavior of the matrix material. The *dashed lines* define slopes E_e/E_1 and E_p/E_1

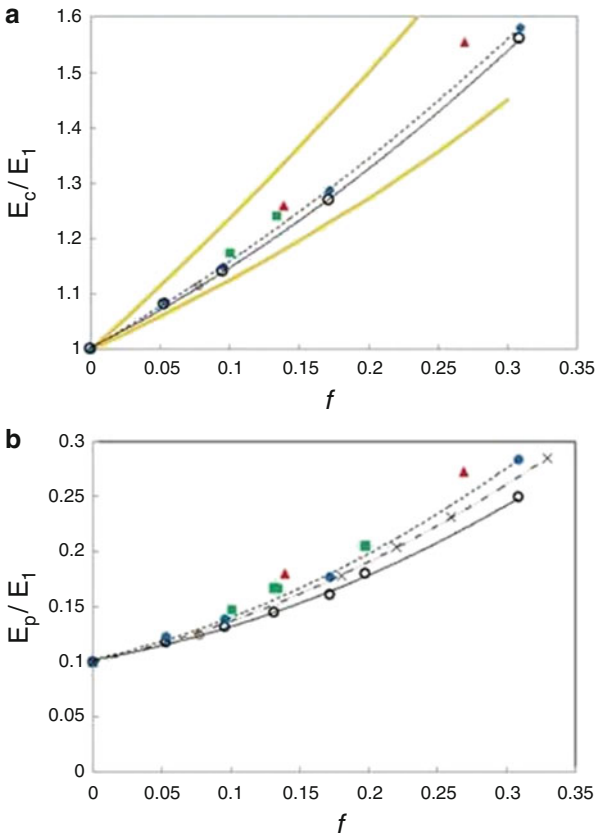

Fig. 5 Variation of (**a**) the elastic modulus (E_e/E_1), and (**b**) strain hardening rate (E_p/E_1) with the volume fraction, for microstructures with randomly distributed inclusions (*open symbols* and *continuous thin line*), and for various fractal microstructures having $M = 9$, $P = 5$, and $n = 2$, 3, 4 and 5 (*blue circles*), $M = 4$, $P = 3$, $n = 7$ and 8, $M = 9$, $P = 6$, $n = 4$ and 5 (*green squares*), $M = 81$, $P = 42$, $n = 2$ and 3 (*red triangles*). Data for microstructures with exponential correlation function (Fig. 1b) are shown in (**b**) with crosses and *dashed–dot line*. The *thick orange continuous lines* in (**a**) represent the 2D Hashin–Shtrikman bounds. The *thin continuous line* and the *dashed line* in both (**a**) and (**b**) represent the best fit to the random structures data and to the fractal structures with $M = 9$, $P = 5$, respectively

and same volume fraction (open symbols). The continuous line represents the constitutive behavior of the matrix material. To characterize the effect of correlations on the constitutive behavior of the composite, we refer next to the two parameters E_e and E_p (normalized by matrix stiffness, E_1).

Figure 5a shows the variation of the elastic modulus, E_e/E_1, with the filler volume fraction, f, for random structures (open symbols), and various fractal structures. Data are shown for $M = 9$, $P = 5$, and $n = 2$, 3, 4 and 5 (blue circles), which all have $D = 1.46$, for $M = 4$, $P = 3$, $n = 7$ and 8 (green squares), which have $D = 1.58$,

and for $M = 81$, $P = 42$, $n = 2$ and 3 (red triangles), which have $D = 1.7$. The thick continuous orange lines represent the Hashin–Shtrikman bounds for the two-dimensional case [10].

The data points for the random, uncorrelated microstructures (open circles) align on a curve shown by the continuous thin line in Fig. 5a. The four data points corresponding to fractal structures with $M = 9$, $P = 5$, $D = 1.46$ (filled circles), are well represented by a similar curve, which is shown by the dashed line in Fig. 5a. Similar trends are observed in Fig. 5b for the strain hardening rate of the composite, E_p/E_1.

It results that the volume fraction has the dominant effect, but the spatial distribution of fillers contributes to stiffening. The effect becomes more pronounced as the range of correlations increases, or, in the fractal case, as the fractal dimension, D, increases. Clearly, the effect is more pronounced in fractal microstructures compared with exponentially correlated microstructures and with random microstructures of same volume fraction. The observed stiffening is attributed to the stronger interaction of inclusions in the spatially correlated microstructures.

The influence of the internal architecture of the composite on the global behavior can be predicted using some of the recently developed homogenization techniques that take into account the higher order, multi-point correlation functions that describe the microstructure [8]. The comparison of such predictions with the numerical data shown in Fig. 5 is presented in [29].

3.2 The Damping Behavior

Let us consider now both matrix and inclusions to be linear elastic, while allowing for dissipation to take place within inclusions. The elastic constants of the matrix and inclusions are identical to those specified above for the elastic-plastic problem. All inclusions have identical elastic and damping properties. The overall damping ratio of the composite, ξ_1, Eq. (2), is evaluated numerically as described in the Methods section. Attention is focused on evaluating the effect of the correlated distribution of inclusions on ξ_1.

Figure 6 shows the damping ratio for the axial eigenmode, ζ_1, function of the volume fraction of inclusions for various systems. The open symbols and the thick line correspond to the random distribution of inclusions, while other symbols correspond to fractal microstructures with various fractal dimensions. The dashed line is fitted to the blue filled circles which correspond to fractal structures with $M = 9$, $P = 5$, and various n values. The error bars are evaluated from sets of 100 replicas for each configuration.

As the fractal dimension increases, the departure from the random case is more pronounced. For the fractal structure with the largest fractal dimension considered, $M = 81$, $P = 42$, $n = 3$, $D = 1.701$, the damping ratio is 53 % larger than that for the random microstructure of same volume fraction. This significant increase is

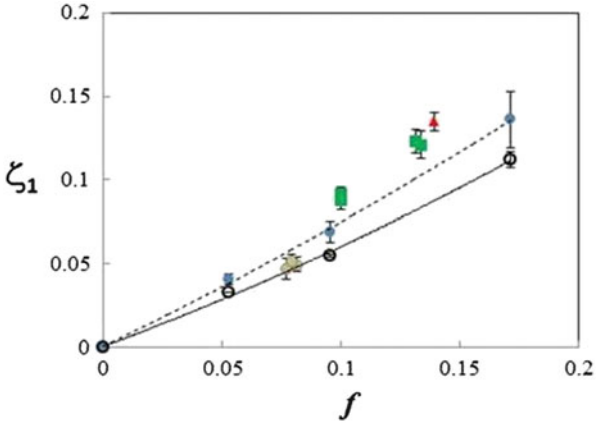

Fig. 6 Variation of the damping ratio, Eq. (2), with the volume fraction for composites with random (*open circles*) and fractal microstructures. The *continuous* and *dashed lines* are fitted to the results for random and fractal ($M = 9$, $P = 5$, *blue circles*) microstructures. The other filled symbols correspond to fractal microstructures with $M = 4$, $P = 3$, $n = 7$ and 8, $M = 9$, $P = 6$, $n = 4$ and 5 (*green squares*), $M = 81$, $P = 42$, $n = 2$ (*red triangles*), $M = 36$, $P = 10$, $n = 2$, $M = 49$, $P = 14$, $n = 2$, $M = 64$, $P = 18$, $n = 2$ (*grey circles*)

due to the interaction between inclusions which is enhanced by their hierarchical distribution.

All fractal structures considered exhibit enhancements relative to the corresponding random cases, the increase being function of D. Gains close to 100 % can be obtained for fractal dimensions close to 1.9 [29].

4 Effect of Fluctuations of Filler Properties

We consider now composites in which the properties of inclusions are allowed to vary from inclusion to inclusion. We consider the elastic-plastic deformation and damping behavior of composites similar to those shown in Figs. 1 and 3.

4.1 The Elastic-Plastic Behavior

In these models, the composite matrix has a bilinear constitutive equation with Young's modulus E_1 and constant tangent stiffness in the plastic range equal to $E_1/10$. Inclusions are linear elastic. Their modulus is sampled from a log-normal distribution with mean $\overline{E}_2 = 7E_1$ and coefficient of variance, $c_E = \sigma_{E_2}/\overline{E}_2$, which is kept as variable. Both matrix and inclusions have Poisson ratio 0.3.

The spatial distribution of inclusions is either random, or power law correlated (fractal), as considered in Sect. 3. In the spatially correlated case, the effect of the non-uniform spatial distribution is superimposed to the effect of fluctuations of inclusion properties. The random variables defining the spatial distribution of inclusions and the values of the respective elastic constants are not cross-correlated.

Standard homogenization theory suggests that for a random distribution of inclusions, the composite modulus should depend on the mean of the stiffness of inclusions and on the filler volume fraction. In this section we investigate to what extent variability in the elastic constants of inclusions matters.

Figure 7 shows the probability distribution functions of the elastic moduli of the composite for several values of the coefficient of variance of the distribution of elastic moduli of inclusions, $c_E = 0,\ 1,\ 3$. The mean of the distribution of elastic moduli of inclusions, $\bar{E}_2$, is the same in all these models. The case $c_E = 0$ corresponds to the situation in which all inclusions are identical and have $E_2 = 7E_1$. The spatial distribution of inclusions in this example is fractal, with $M = 9$, $P = 5$, and $n = 5$, the volume fraction of fillers being $f = 5.29$ %. The probability distributions for the case of uncorrelated, random spatial distribution of fillers overlap those presented in Fig. 7.

Interestingly, the composite softens as c_E increases, even though the mean of the distribution of inclusion elastic constants is kept invariant. The variance of the overall composite modulus increases with c_E as well.

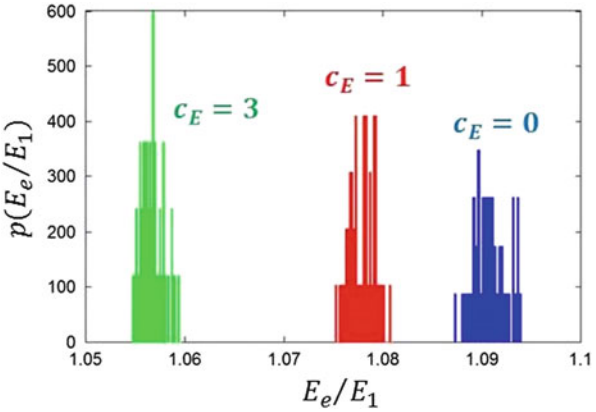

Fig. 7 Probability distribution functions of Young's modulus of composites with fractal distribution of fillers and filler elastic moduli that vary from inclusion to inclusion. The *blue* distribution ($c_E = 0$) corresponds to the case in which all fillers are identical. The other distributions (*green* and *red*) correspond to composites with distributions of filler elastic constants of increasing coefficient of variance, c_E, and same mean. The mean of the composite modulus decreases as c_E increases. The composite modulus is normalized by the matrix elastic modulus E_1

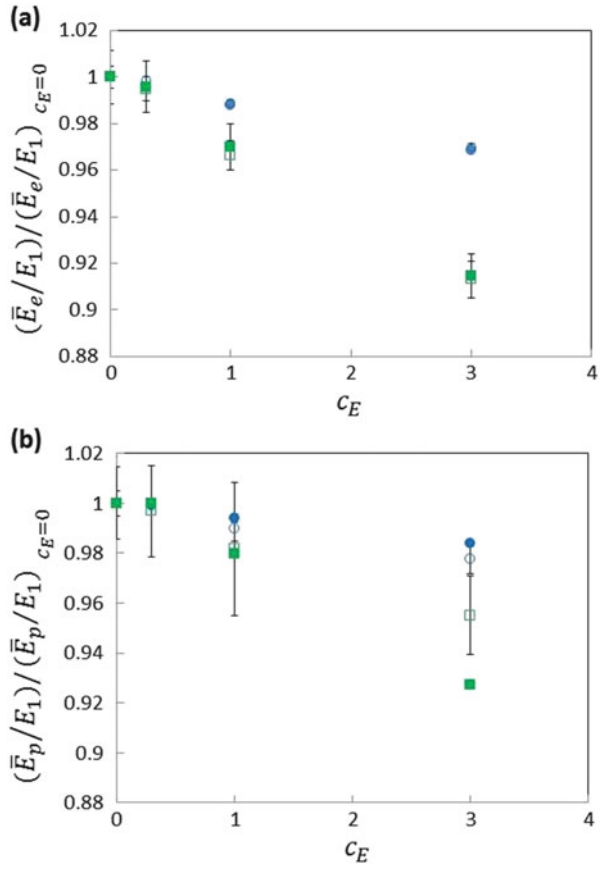

Fig. 8 Variation of the mean of the distribution function of the (**a**) composite modulus and (**b**) strain hardening rate with the coefficient of variance of the distribution function of filler Young's modulus. The distribution functions of filler moduli for all cases shown have the same mean and different c_E. The *open symbols* corresponds to spatially uncorrelated filler distributions (random), while the *filled symbols* correspond to fractal microstructures with $M = 9$, $P = 5$, $n = 5$. *Circles* and *squares* correspond to filler volume fraction of 5.29 % and 17.15 %, respectively. The vertical axes are normalized by the value of the respective variables corresponding to the case in which all inclusions are identical, $c_E = 0$

Figure 8 quantifies the softening effect. Figure 8a shows the variation of the normalized mean composite modulus, $\bar{E}_e/E_1$, with the coefficient of variance c_E. The vertical axis is normalized with the value of $\bar{E}_e/E_1$ corresponding to the case in which all inclusions are identical, i.e., $c_E = 0$. The variation is linear in the range of parameters considered. The difference between the random structures and structures with fractal distribution of inclusions is small. The effect is more pronounced as the volume fraction of inclusions, f, increases due to the enhanced filler–filler

interaction. The maximum effect obtained is a decrease of the composite modulus of 10 % relative to the reference case of a composite with identical inclusions.

Figure 8b shows data for the mean strain hardening rate, $\bar{E}_p/E_1$. This parameter decreases with increasing c_E, but the rate of decrease is slightly smaller compared with that in Fig. 8a. Overall, the composite becomes softer both elastically and plastically due to the fluctuation of the elastic constants of inclusions.

It is interesting to note that a similar effect has been obtained in random fiber networks. These are systems of fibers which are bonded to each other to form a three-dimensional network with non-zero global stiffness. Fibers are athermal and have both bending and axial stiffness. In the study reported in [44], fibers are not identical, rather their axial and bending stiffness are sampled from log-normal distribution functions. A comparison is performed between networks characterized by distributions of fiber properties that have the same mean and various coefficients of variance. It is observed that the overall network stiffness decreases as the coefficient of variance increases. The magnitude of the softening effect is similar to that reported in Fig. 8a for the same range of c_E. An analytic argument justifying the numerical results is presented in reference [44].

4.2 The Damping Behavior

A similar analysis is performed for the damping behavior of the composite. As in Sect. 3, composites with linear elastic matrix and inclusion materials are considered, with damping being allowed within fillers. The Young's modulus has the same value in all fillers and the ratio of filler modulus to matrix modulus is 6. The damping matrix of the filler material, $\mathbf{C}$ [Eq. (1)], is multiplied by a stochastic variable C' which is sampled from a log-normal distribution of mean $\overline{C}$' and coefficient of variance $c_{C'} = \sigma_{C'}/\overline{C}$'. The overall energy dissipation rate on the scale of the composite, characterized by the damping ratio for the axial vibration mode, ξ_1 [Eq. (2)], is evaluated for systems with same $\overline{C}$' and increasing $c_{C'}$. As above, we investigate whether or not the overall behavior depends exclusively on the mean damping coefficient, $\overline{C}'$.

Figure 9 shows the results of this study. It is seen that increasing the value of $c_{C'}$ does not change the mean damping ratio measured on the composite scale, $\overline{\xi}_1$. Therefore, higher moments of the distribution function of C' are inconsequential for the composite level behavior. This conclusion is opposite to that described above for the elastic-plastic behavior. This indicates that each of these effects should be studied individually and extrapolation of one type of behavior to other physical parameters is not warranted.

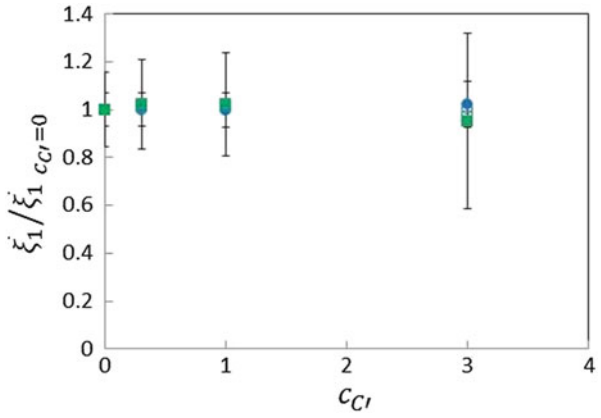

Fig. 9 Variation of the mean of the distribution function of damping ratio of the composite with the coefficient of variance of the distribution function of damping coefficients within inclusions, $c_{C'}$. The vertical axis is normalized by the value of the variable corresponding to the case in which all inclusions are identical, $c_{C'} = 0$. *Open* and *filled symbols* correspond to uncorrelated and fractal microstructures, respectively. *Circles* and *squares* correspond to filler volume fractions of 5.29 % and 17.15 %, respectively

5 Conclusions

The results presented in this chapter indicate that composite design can benefit significantly from the enlargement of the design space associated with controlling the stochasticity of the microstructure. This is made possible by the advent of 3D printing technologies which offer unprecedented control of the material composition and spatial distribution of inclusions in composites. This numerical work shows that spatially correlated distributions of inclusions lead to stiffer composites that strain harden more than the equivalent composites of same volume fraction and with random distribution of inclusions. If energy dissipation takes place within inclusions, the global damping on the composite scale increases as the distribution of inclusions becomes spatially correlated over larger distances. Additional effects can be obtained if filler properties are allowed to be stochastic. Composites in which the elastic constants of inclusions are sampled from distributions of given mean and with increasing variance exhibit an interesting decrease of stiffness and strain hardening rate as the respective variance increases. However, when energy dissipation is allowed within inclusions and the damping coefficient varies from filler to filler, the damping on the scale of the composite is insensitive to the higher moments of the distribution function of filler damping coefficients.

Additional effects of this type are expected when other parameters describing the stochastic microstructure are controlled and varied. This opens new directions of study in composite design and should lead to materials with unprecedented combinations of properties.

Acknowledgments This work has been supported in part by the Romanian National Authority for Scientific Research, CNCS–UEFISCDI, project number PN-II-ID-PCE-2011-3-0120, under contract 293/2011.

References

1. Agarwal BD (1990) Analysis and performance of fiber composites. Wiley, New York
2. Reilly DT, Burstein AH (1975) The elastic and ultimate properties of compact bone tissue. J Biomech 8:393–405
3. Barnes SJ, Harris LP (2008) Tissue engineering: roles, materials, applications. Nova, New York
4. Breneman CM, Brinson LC et al (2013) Stalking the materials genome: a data-driven approach to the virtual design of nanostructured polymers. Adv Funct Mater 23:5746–5752
5. Erman B, Mark JE (1997) Structure and properties of rubber-like networks. Oxford University Press, New York
6. Courtney TH (1990) Mechanical behavior of materials. McGraw-Hill, New York
7. Nemat-Nasser S, Hori M (1999) Micromechanics: overall properties of heterogeneous materials. North-Holland, Amsterdam
8. Torquato S (2002) Random heterogeneous materials: microstructure and macroscopic properties. Springer, New York
9. Dvorak GJ (2013) Mechanics of composite materials. Springer, New York
10. Hashin Z, Shtrikman S (1962) On some variational principles in anisotropic and nonhomogeneous elasticity. J Mech Phys Solids 10:335–342
11. Beran MJ, Molyeux J (1966) Continuum theories. Wiley, New York
12. Silnutzer NR (1972) Effective constants of statistically homogeneous materials. PhD thesis, University of Pennsylvania, Philadelphia
13. Milton GW (1981) Bounds on the electromagnetic, elastic, and other properties of two-component composites. Phys Rev Lett 46:542–545
14. Milton GW (1982) Bound on the elastic and transport properties of two component composites. J Mech Phys Solids 30:177–191
15. Phan-Tien N, Milton GW (1982) New bounds on the effective thermal conductivity of n-phase materials. Proc R Soc Lond A 380:333–348
16. Quinatanilla J, Torquato S (1995) New bounds on the elastic moduli of suspensions of spheres. Appl Phys 77:4361–4372
17. Oshmyan VG, Patlashan SA, Timan SA (2001) Elastic properties of Sierpinski-like carpets: finite-element-based simulation. Phys Rev E 64(056108):1–10
18. Salganik RL (1973) Mechanics of bodies with many cracks. Mech Solids 8:135–143
19. Dyskin AV (2005) Effective characteristics and stress concentrations in materials with self-similar microstructure. Int J Solids Struct 42:477–502
20. Tarasov VE (2005) Fractional hydrodynamics equations for fractal media. Ann Phys 318:286–307
21. Tarasov VE (2005) Continuous medium model for fractal media. Phys Lett A 336:167–174
22. Ostoja-Starzewski M (2007) Towards thermoelasticity of fractal media. J Therm Stresses 30:889–896
23. Ostoja-Starzewski M (2009) Extremum and variational principles for elastic and inelastic media with fractal geometries. Acta Mech 205:161–170
24. Carpinteri A, Chiaia B, Cornetti P (2004) A fractal theory for the mechanics of elastic materials. Mater Sci Eng A 365:235–240
25. Soare MA, Picu RC (2007) An approach to solving mechanics problems for materials with multiscale self-similar microstructure. Int J Solids Struct 44:7877–7890

26. Picu RC, Soare MA (2009) Mechanics of materials with self-similar hierarchical microstructure. In: Galvanetto U, Aliabadi MF (eds) Multiscale modeling in solid mechanics—computational approaches. Imperial College Press, London, pp 295–332
27. Kolwankar KM, Gangal AD (1996) Fractional differentiability of nowhere differentiable functions and dimensions. Chaos 6:505–524
28. Kolwankar KM (1998) Studies of fractal structures and processes using methods of fractional calculus. PhD thesis, University of Pune, India
29. Picu RC, Li Z et al (2014) Composites with fractal microstructure: the effect of long range correlations on the elastic-plastic and damping behavior. Mech Mater 69:251–261
30. Papadrakakis M, Papadopoulos V (1996) Robust and efficient methods for stochastic finite element analysis using Monte Carlo simulations. Comput Methods Appl Mech Eng 134:325–340
31. Liu WK, Belytschko T, Mani A (1986) Probabilistic finite elements for nonlinear structural dynamics. Comput Methods Appl Mech Eng 56:61–81
32. Liu WK, Mani A, Belytschko T (1987) Finite element methods in probabilistic mechanics. Probab Eng Mech 2:201–213
33. Ghanem G, Spanos PD (1991) Stochastic finite elements: a spectral approach. Springer, New York
34. Ghanem R, Dham S (1998) Stochastic finite element analysis for multiphase flow in heterogeneous porous media. Transp Porous Media 32:239–262
35. Matthies HG, Brenner CE, Bucher CG, Soares CG (1997) Uncertainties in probabilistic numerical analysis of structures and solids—stochastic finite elements. Struct Saf 19:283–336
36. Soare MA, Picu RC (2008) Boundary value problems defined on stochastic self-similar multiscale geometries. Int J Numer Methods Eng 74:668–696
37. Soare MA, Picu RC (2008) Spectral decomposition of random fields defined over the generalized Cantor set. Chaos Solitons Fractals 37:566–573
38. Matthies HG, Keese A (2005) Galerkin methods for linear and nonlinear elliptic stochastic partial differential equations. Comput Methods Appl Mech Eng 194:1295–1331
39. Cameron RH, Martin WT (1947) The orthogonal development of nonlinear functionals in series of Fourier–Hermite functionals. Ann Math 48:385–392
40. Wiener N (1958) Nonlinear problems in random theory. Technology Press of the Massachusetts Institute of Technology and Wiley, New York
41. Karhunen K (1947) Uber lineare methoden in der wahrscheinlicheitsrechtung. American Academy of Science Fennicade, Ser.A.I 37:3–79 (Translation: RAND Corporation, Santa Monica, CA, Report T-131, 1960)
42. Loeve M (1948) Fonctions aleatoires du second ordre. Suplement to P. Levy, Processus Stochastic et Mouvement Brownien. Gauthier-Villars, Paris
43. Gel'fand IM, Vilnekin NY (1964) Generalized functions, vol 4. Academic, New York
44. Ban E, Picu RC, Barocas V, Shephard MS (2015) Effect of variability of fiber properties on mechanical behavior of composite fiber networks. Phys Rev B (Submitted to JMPS)

Discrete to Scale-Dependent Continua for Complex Materials: A Generalized Voigt Approach Using the Virtual Power Equivalence

Patrizia Trovalusci

Abstract The mechanical behaviour of complex materials, characterized at finer scales by the presence of heterogeneities of significant size and texture, strongly depends on their microstructural features. By lacking in material internal scale parameters, the classical continuum does not always seem appropriate for describing the macroscopic behaviour of such materials, taking into account the size, the orientation and the disposition of the heterogeneities. This often calls for the need of non-classical continuum descriptions, which can be obtained through multiscale approaches aimed at deducing properties and relations by bridging information at different levels of material descriptions.

Current researches in solid state physics as well as in mechanics of materials show that energy-equivalent continua obtained by defining direct links with lattice systems, as widely investigated by the corpuscular-continuous approaches of nineteenth century, are still among the most promising approaches in material science. The aim is here to point out the suitability of adopting discrete to scale-dependent continuous models, based on a generalization of the so-called Cauchy–Born (Voigt) rule used in crystal elasticity and in classical molecular theory of elasticity, in order to identify continua with additional degrees of freedom (micromorphic, multifield, etc.) which are essentially non-local models with internal length and dispersive properties. It is shown that, within the general framework of the principle of virtual powers, the correspondence map relating the finite number of degrees of freedom of discrete models to the continuum kinematical fields provides a guidance on the choice of the most appropriate continuum approximation for heterogeneous media. Some applications of the mentioned approach to ceramic matrix composites and masonry-like materials are discussed.

P. Trovalusci (✉)
Department of Structural and Geotechnical Engineering, Sapienza University of Roma, Roma, Italy
e-mail: patrizia.trovalusci@uniroma1.it

P. Trovalusci (ed.), *Materials with Internal Structure*, Springer Tracts in Mechanical Engineering, DOI 10.1007/978-3-319-21494-8_8

1 Introduction

This contribution focuses on constitutive theories for continuous models originated from refined discontinuous descriptions of materials. The classical molecular theory of elasticity, as developed by Navier [25], Cauchy [7] and Poisson [30] in the nineteenth century, represents the first attempt to derive the field equations of an elastic body basing on the definition of microscopic laws for systems of point-like particles ("molecules") close together and interacting through attractive forces. In these mechanistic descriptions, inspired to Newton's idea of coherence of elastic bodies [26], the molecules, are perceived as ultimate particles without extension, inside which no forces are accounted for, that interact in pairs through forces depending on their mutual distance and directed along the line connecting their centres ("central-force" scheme). A kinematic corresponding map between the discrete degrees of freedom and the continuous fields guarantees the transition from the fine to the gross description. Macroscopic stress measures are then derived as averages of molecular material quantities over a convenient volume element, called "molecular sphere of action", outside which intermolecular forces are negligible.

The central-force description led to experimental discrepancies concerning the number of elastic constants, that were less than those needed to represent the behaviour of materials belonging to various symmetry classes. Successively, Voigt and Poincaré introduced mixed energetic/mechanistic approaches providing refined molecular models that circumvented the problem of the underestimation of the number of the material constants related to the central-force scheme [2, 3, 31, 33]. In particular, Voigt introduced a potential of force and moment interactions exerted between pairs of rigid bodies, while Poincaré proposed a multibody potential description [29, 35, 36]. Both Voigt and Poincaré removed the local character of the Cauchy description by modifying the central-force scheme thus obtaining continua which could be classifiable as "implicitly" or "weakly" non-local [10, 18, 20], because of the presence of internal lengths and dispersion properties that can be there recognized [31]; although they finally led back to classical continua by introducing internal constraints: Voigt by imposing the same uniform rotation to the particles and Poincaré by considering only pair-interaction terms. However, even if both Voigt and Poincaré, on using the refinement of non-local descriptions, offered a good solution to the controversy about the elastic constants, the mechanistic-molecular approach was abandoned in favour of the energetic-continuum approach by Green, and their works have been neglected for long time [3].

Now these ideas found a renewed interest with particular reference to the problem of constitutive modelling of composite materials. The mechanical behaviour of materials characterized at finer scales by the presence of heterogeneities of significant size and texture strongly depends on their internal structure that is intrinsically heterogeneous and discrete because interfaces (grain boundaries, thin layers, etc.) dominate the gross behaviour. By lacking in material internal scale parameters, moreover, the classical continuum does not always seem appropriate to describe the macroscopic behaviour of such materials taking into account the size, the

orientation and the disposition of the heterogeneities. This calls for the need of non-local continuum descriptions which can still be obtained through homogenization approaches aimed at deducing properties and relations by bridging information at proper underlying discrete micro-levels via energy equivalence criteria. Thus, providing that the original lattice models were refined by extending the concept of molecule in order to describe different internal phases (rigid inclusions, voids, etc.) and taking into account of non-central inter-molecular actions, or by enriching the potential descriptions introducing multibody interaction terms, discrete-to-scale-dependent non-local continua could be naturally derived. As sample models nonlocal continua with additional degrees of freedom are reported. These continua are non-classical continua, of the kind described in [1, 5, 10, 14, 22], derived from lattice systems made of rigid particles and distributed voids (pores, microcracks, etc.) and adopted for the description of ceramic matrix composites or masonry-like materials.

2 Corpuscular Micro-Model

The discrete model adopted for the fine description of the reference composite material is made of kind of structured molecules broadly representing the internal phases of the material: the fibres, described as rigid particles of polygonal shape, and the flaws, perceived as slits of arbitrary shape and a predominant dimension. The slits are considered opened, stationary and with blunt edges (no tip effects accounted for). The particles interact in pairs through forces and couples, while the slits interact through forces directed along the line connecting their centres. Particles and slits also interact each other by forces. The slits must be considered as devices for transmitting to the matrix additional forces due to the presence of defects. In this sense they represent the microcracks/pores. Their stiffness depends on the surrounding elastic field. In this paragraph the analysis is conducted within the linearised framework, where the velocity fields stand for infinitesimal displacement fields and the power stands for work.

Let $\mathscr{A}$ and $\mathscr{B}$ be two rigid particles, respectively centred at the positions $\mathbf{a}$ and $\mathbf{b}$, and $\mathscr{H}$ and $\mathscr{K}$ two slits located at the positions $\mathbf{h}$ and $\mathbf{k}$. The vectors $\mathbf{w}^a$ and $\mathbf{w}^b$ respectively denote the velocity of $\mathbf{a}$ and $\mathbf{b}$ and the skew-symmetric tensors $\mathbf{W}^a$ and $\mathbf{W}^b$ the angular velocities of the two particles. For each pair of adjacent particles the strain measures of the lattice are defined as:

$$\begin{aligned} \mathbf{w}_i &= \mathbf{w}_i^a - \mathbf{w}_i^b = [\mathbf{w}^a + \mathbf{W}^a(\mathbf{p}^a - \mathbf{a})] - [\mathbf{w}^b + \mathbf{W}^b(\mathbf{p}^b - \mathbf{b})]\,, \\ \mathbf{W}_i &= \mathbf{W}^a - \mathbf{W}^b\,, \end{aligned} \tag{1}$$

where $\mathbf{p}^a$ and $\mathbf{p}^b$ are two test points, on $\mathscr{A}$ and $\mathscr{B}$, through which the particles interact, and $\mathbf{w}_i^a$ and $\mathbf{w}_i^b$ their velocities. Further lattice strain measures for each slit $\mathscr{H}$, each pair of interacting slits ($\mathscr{H}$, $\mathscr{K}$) and each pair of interacting particle-slit

$(\mathscr{A}, \mathscr{H})$ are:

$$\mathbf{d}^h\,, \qquad \mathbf{d}_j = \mathbf{d}^h - \mathbf{d}^k\,, \qquad \mathbf{w}_l = \mathbf{w}_i^a - (\mathbf{w}^h + \mathbf{d}^h)\,, \tag{2}$$

where: the vector $\mathbf{d}^h$ ($\mathbf{d}^k$) represents the half-crack opening displacement on $\mathscr{H}$ ($\mathscr{K}$) and $\mathbf{w}^h$ ($\mathbf{w}^k$) is the velocity vector of $\mathbf{h}$ ($\mathbf{k}$) on the external boundary of $\mathscr{H}$ ($\mathscr{K}$).

The forces and the couples that $\mathscr{B}$ ($\mathscr{A}$) exerts on $\mathscr{A}$ ($\mathscr{B}$) are respectively represented by the vector $\mathbf{t}^a$ ($\mathbf{t}^b$) and the skew-symmetric tensor $\mathbf{C}^a(\mathbf{C}^b)$. The force due to $\mathbf{d}^h$ on $\mathscr{H}$ is represented by the vector $\mathbf{z}_o^h$. Due to $\mathbf{d}^h$, the slit interacts with the adjacent particles and the neighbouring slits. The vector $\mathbf{z}^h$ ($\mathbf{z}^k$) is the force that $\mathscr{K}$ ($\mathscr{H}$) exerts on $\mathscr{H}$ ($\mathscr{K}$), while the vector $\mathbf{r}^h$ ($\mathbf{r}^a$) represents the force transmitted by $\mathscr{H}$ ($\mathscr{A}$) to $\mathscr{A}$ ($\mathscr{H}$).

If the material can be considered periodic, or at least statistically homogeneous, a representative volume element, $\mathscr{M}_\mu$, referred as the module, can be individuated. Taking into account the balance equations of the internal actions of the module the mean power of the internal actions over the volume of the module, $V(\mathscr{M}_\mu)$, can be written:

$$\begin{aligned}\bar{\Pi}_\mu = \tfrac{1}{V(\mathscr{M}_\mu)}\,\{&\sum_i \{\mathbf{t}_i \cdot [\mathbf{w}_i - \mathbf{W}^a(\mathbf{p}^a - \mathbf{p}^b)] + \frac{1}{2}\mathbf{C}_i \cdot \mathbf{W}_i\} \\ &+ \sum_h \mathbf{z}_o^h \cdot \mathbf{d}^h + \sum_j \mathbf{z}_j \cdot \mathbf{d}_j + \sum_l \{\mathbf{r}_l \cdot [\mathbf{w}_l - \mathbf{W}^a(\mathbf{p}^a - \mathbf{h})]\}\}\,,\end{aligned} \tag{3}$$

where it has been put: $\mathbf{t}^a = -\mathbf{t}^b = \mathbf{t}_i\,,\ \mathbf{z}^h = -\mathbf{z}^k = \mathbf{z}_j\,,\ \mathbf{r}^h = -\mathbf{r}^a = \mathbf{r}_l\,,$

$$\mathbf{C}^a = -\mathbf{C}^b + [(\mathbf{p}^a - \mathbf{p}^b) \otimes \mathbf{t}^a - \mathbf{t}^a \otimes (\mathbf{p}^a - \mathbf{p}^b)] + [(\mathbf{p}^a - \mathbf{h}) \otimes \mathbf{r}^h - \mathbf{r}^h \otimes (\mathbf{p}^a - \mathbf{h})] = \mathbf{C}_i,$$

and where the summations are respectively extended to each pair $(\mathscr{A}, \mathscr{B})$, $(\mathscr{H}, \mathscr{K})$, $(\mathscr{A}, \mathscr{H})$ in $\mathscr{M}_\mu$.

The selection of linear elastic response functions for the interactions between particles and for the forces due to the crack opening displacements; non-linear elastic functions for the interactions between slits, described as continuous distributions of dislocations with Burgers' vector parallel to the opening directions; other non-linear phenomenological functions for the interactions between slits and particles:

$$\begin{aligned}&\mathbf{t}_i = \mathbf{K}_i[\mathbf{w}_i - \mathbf{W}^a(\mathbf{p}^a - \mathbf{p}^b)]\,, \qquad \mathbf{C}_i = \mathsf{K}_i\mathbf{W}_i\,, \qquad \mathbf{z}_o^h = \mathbf{D}^h\mathbf{d}^h\,, \\ &\mathbf{z}_j = D_j \frac{\| \mathbf{d}^h \| \| \mathbf{d}^k \|}{\| \mathbf{h} - \mathbf{k} \|^2}\,(\mathbf{h} - \mathbf{k})\,, \qquad \mathbf{r}_l = \frac{f_1(\mathbf{a}) f_2(\mathbf{h})}{\| \mathbf{a} - \mathbf{h} \|^2}\,(\mathbf{a} - \mathbf{h})\,,\end{aligned} \tag{4}$$

here assumes a purely paradigmatic meaning for the procedure reported in Sect. 3 and it can at any time be modified in order to meet the needs of finer constitutive descriptions. In Eqs. (4) the components of the second order $\mathbf{K}_i$, $\mathbf{D}^h$ and fourth order K_i tensors; the constant D_j and the scalar functions f_1 and f_2 (two approximately

Gaussian functions describing respectively the local force field around a particle ($\mathscr{A}$) and a slit ($\mathscr{H}$) [19]) depend on the elastic constants of the matrix and the geometry of the two kinds of inclusions.

3 Micro–Macro Transition via Virtual Power Equivalence

In order to identify the equivalent continuum model, hypotheses of regularity of the kinematical descriptors introduced in Sect. 2 are given. According to discrete-continuum coarse-graining approaches described in [31], kinematical maps relating discrete-to-continuous kinematical fields are introduced. These maps are given by Taylor expansions up to the second order of the macro velocity vector $\mathbf{w}(\mathbf{x})$, the skew-symmetric micro angular velocity tensor $\mathbf{W}(\mathbf{x})$, and the independent micro velocity vector $\mathbf{d}(\mathbf{x})$:

$$\begin{aligned}
\mathbf{w}^a &= \mathbf{w}(\mathbf{x}) + \nabla\mathbf{w}(\mathbf{x})(\mathbf{a}-\mathbf{x}) + \frac{1}{2}[\nabla^2\,\mathbf{w}(\mathbf{x})(\mathbf{a}-\mathbf{x})](\mathbf{a}-\mathbf{x}) + o\,(\mathbf{a}-\mathbf{x}) \\
\mathbf{W}^a &= \mathbf{W}(\mathbf{x}) + \nabla\mathbf{W}(\mathbf{x})(\mathbf{a}-\mathbf{x}) + \frac{1}{2}[\nabla^2\mathbf{W}(\mathbf{x})(\mathbf{a}-\mathbf{x})](\mathbf{a}-\mathbf{x}) + o\,(\mathbf{a}-\mathbf{x}) \\
\mathbf{d}^h &= \mathbf{d}(\mathbf{x}) + \nabla\mathbf{d}(\mathbf{x})(\mathbf{h}-\mathbf{x}) + \frac{1}{2}[\nabla^2\,\mathbf{d}(\mathbf{x})(\mathbf{h}-\mathbf{x})](\mathbf{a}-\mathbf{x}) + o\,(\mathbf{h}-\mathbf{x})\,, \qquad (5)
\end{aligned}$$

for any $\mathscr{A}$, $\mathscr{H} \in \mathscr{M}_\mu$, where $\mathbf{x}$ is the centre of the module and where, from now on, the term "macro" stands for standard and "micro" for non-standard fields. Assuming that a continuous neighbourhood $\mathscr{M}$ of $\mathbf{x}$, occupying the same Euclidean region of $\mathscr{M}_\mu$, is well defined, these maps impose that the continuum locally undergoes the same deformations as the lattice system. Eqs. (5) provide a generalization of Cauchy, Voigt or Poincaré's homogenization rules reported in [31]. From now on, the explicit dependence of any field on $\mathbf{x}$ will be undertaken.

Basing on the maps (5) various kinds of continua can be identified that are in general non-classical, as described in [31]. By expanding the series up to higher orders refined descriptions allowing to take into account long-range interactions can be obtained. Specific continuous models can also be derived by imposing proper internal constraints to the lattice model, as in the cases studied by Voigt and Poincaré, obtaining continua that can be defined continua with latent microstructure [4].

3.1 First Order Continuum Approximation: Continuum with Rigid and Affine Local Structure

Using Eqs. (5) with $\nabla\mathbf{w}$, $\nabla\mathbf{W}$ and $\nabla\mathbf{d}$ constant the strain measures of the lattice system (1), (2) can be expressed in terms of the smooth fields $\nabla\mathbf{w} - \mathbf{W}$, $\nabla\mathbf{W}$, $\mathbf{d}$ and

$\nabla\mathbf{d}$ as:

$$\begin{aligned}\mathbf{w}_i &= (\nabla\mathbf{w}-\mathbf{W})(\mathbf{a}-\mathbf{b})+\nabla\mathbf{W}\left[(\mathbf{p}^a-\mathbf{a})\otimes(\mathbf{a}-\mathbf{x})-(\mathbf{p}^b-\mathbf{b})\otimes(\mathbf{a}-\mathbf{x})\right],\\ \mathbf{W}_i &= \nabla\mathbf{W}(\mathbf{a}-\mathbf{b}),\\ \mathbf{d}_j &= \nabla\mathbf{d}(\mathbf{h}-\mathbf{k}),\end{aligned} \tag{6}$$

where the explicit dependence of any field on $\mathbf{x}$ has been undertaken.

After some algebra, the mean power of the contact actions (3) can be also expressed as function of these strain fields:

$$\begin{aligned}\bar{\Pi}_\mu =& \frac{1}{V(\mathscr{M}_\mu)}\{\{\sum_i \mathbf{t}_i\otimes(\mathbf{a}-\mathbf{b})+\sum_i \mathbf{r}_l\otimes(\mathbf{a}-\mathbf{h})\}\cdot(\nabla\mathbf{w}-\mathbf{W})\\ &+\{\sum_i \mathbf{t}_i\otimes[(\mathbf{p}^a-\mathbf{a})\otimes(\mathbf{a}-\mathbf{x})-(\mathbf{p}^b-\mathbf{b})\otimes(\mathbf{b}-\mathbf{x})]+\frac{1}{2}\mathbf{C}_i\otimes(\mathbf{a}-\mathbf{b})\}\cdot\nabla\mathbf{W}\\ &+\{\sum_h \mathbf{z}_o^h+\sum_l \mathbf{r}_l\}\cdot\mathbf{d}\\ &+\{\sum_h \mathbf{z}_o^h\otimes(\mathbf{h}-\mathbf{x})+\sum_j \mathbf{z}_j\otimes(\mathbf{h}-\mathbf{k})+\sum_l \mathbf{r}_l\otimes(\mathbf{h}-\mathbf{x})\}\cdot\nabla\mathbf{d}\}.\end{aligned} \tag{7}$$

It can be now assumed that a continuum scalar field representing the internal power density of a multifield continuum, in a neighbourhood of $\mathbf{x}$ occupying the same region of the module $\mathscr{M}\equiv\mathscr{M}_\mu$, exists as a function of the primal strain fields $\nabla\mathbf{w}-\mathbf{W}$, $\nabla\mathbf{W}$, $\mathbf{d}$, $\nabla\mathbf{d}$:

$$\pi(\nabla\mathbf{w}-\mathbf{W},\mathbf{d},\nabla\mathbf{d}) = \mathbf{S}\cdot(\nabla\mathbf{w}-\mathbf{W})+\frac{1}{2}\mathsf{S}\cdot\nabla\mathbf{W}+\mathbf{z}\cdot\mathbf{d}+\mathbf{Z}\cdot\nabla\mathbf{d}, \tag{8}$$

where the second order tensor $\mathbf{S}$, the third order tensor S, the vector $\mathbf{z}$ and the second order tensor $\mathbf{Z}$ are the dual stress fields power-conjugate to the strain measures $\nabla\mathbf{w}-\mathbf{W}$, $\nabla\mathbf{W}$, $\mathbf{d}$, $\nabla\mathbf{d}$, respectively.

The requirement that the internal power is preserved in the transition from the fine to the gross description for any $\nabla\mathbf{w}-\mathbf{W}$, $\nabla\mathbf{W}$, $\mathbf{d}$ and $\nabla\mathbf{d}$, through the localization theorem, gives:

$$\bar{\Pi}_\mu(\nabla\mathbf{w}-\mathbf{W},\mathbf{d},\nabla\mathbf{d}) = \pi(\nabla\mathbf{w}-\mathbf{W},\mathbf{d},\nabla\mathbf{d}). \tag{9}$$

Then the continuum stress measures are identified as functions of the internal actions and of the fabric vector and tensors of the module (i.e. size, shape and disposition

of inclusions):

$$\begin{aligned}
\mathbf{S} &= \tfrac{1}{V(\mathscr{M}_\mu)} \{\sum_i \mathbf{t}_i \otimes (\mathbf{a}-\mathbf{b}) + \sum_l \mathbf{r}_l \otimes (\mathbf{a}-\mathbf{h})\}\,,\\
\mathsf{S} &= \tfrac{1}{V(\mathscr{M}_\mu)} \{\sum_i 2\mathbf{t}_i \otimes [(\mathbf{p}^a-\mathbf{a}) \otimes (\mathbf{a}-\mathbf{x}) - (\mathbf{p}^b-\mathbf{b}) \otimes (\mathbf{b}-\mathbf{x})] + \mathbf{C}_i \otimes (\mathbf{a}-\mathbf{b})\}\,,\\
\mathbf{z} &= \tfrac{1}{V(\mathscr{M}_\mu)} \{\sum_h \mathbf{z}_o^h + \sum_l \mathbf{r}_l\}\,,\\
\mathbf{Z} &= \tfrac{1}{V(\mathscr{M}_\mu)} \{\sum_h \mathbf{z}_o^h \otimes (\mathbf{h}-\mathbf{x}) + \sum_j \mathbf{z}_j \otimes (\mathbf{h}-\mathbf{k}) + \sum_l \mathbf{r}_l \otimes (\mathbf{h}-\mathbf{x})\}\,. \qquad (10)
\end{aligned}$$

In the virtual power setting delineated, non variational, the results apply regardless of the material response. Once the constitutive equations for the lattice system are defined, for instance those of Eqs. (4), by identifying the actual strain rates of the discrete model using again the maps (5), always under the hypothesis of homogeneous deformations, the continuum constitutive relations for all the stress measures introduced are derived in the following form:

$$\begin{aligned}
\mathbf{S} &= \mathsf{A}(\nabla\mathbf{w}-\mathbf{W}) + \mathsf{B}\nabla\mathbf{W} + \mathsf{C}\mathbf{d} + \mathsf{D}\nabla\mathbf{d} + \Psi_{\mathbf{S}}(\mathbf{d}^2, \nabla\mathbf{d}^2, \| \mathbf{d} \| \| \nabla\mathbf{d} \|)\,,\\
\mathsf{S} &= \mathsf{E}(\nabla\mathbf{w}-\mathbf{W}) + \mathsf{F}\nabla\mathbf{W}\,,\\
\mathbf{z} &= \mathsf{I}(\nabla\mathbf{w}-\mathbf{W}) + \mathbf{M}\mathbf{d} + \mathsf{N}\nabla\mathbf{d} + \Psi_{\mathbf{z}}(\mathbf{d}^2, \nabla\mathbf{d}^2, \| \mathbf{d} \| \| \nabla\mathbf{d} \|)\,,\\
\mathbf{Z} &= \mathsf{O}(\nabla\mathbf{w}-\mathbf{W}) + \mathsf{Q}\mathbf{d} + \mathsf{R}\nabla\mathbf{d} + \Psi_{\mathbf{Z}}(\mathbf{d}^2, \nabla\mathbf{d}^2, \| \mathbf{d} \| \| \nabla\mathbf{d} \|)\,. \qquad (11)
\end{aligned}$$

In Eqs. (11) the constitutive tensors of the second ($\mathbf{M}$), third (C, I, N, Q), fourth (A, D, O, R), fifth (B, E) and sixth (F) order have components depending on the elastic constants and the geometrical parameters of the material phases, as well as the non-linear vector ($\Psi_{\mathbf{z}}$) and second order tensor ($\Psi_{\mathbf{S}}\,, \Psi_{\mathbf{Z}}$) functions. If the discrete system is hyperelastic, also the equivalent continuum is hyperelastic and the following symmetry relations between constitutive tensors hold: $\mathsf{B}\mathsf{T}\cdot\mathbf{T} = \mathsf{T}\cdot\mathsf{E}\mathbf{T}$, for any third order tensor T and second order tensor $\mathbf{T}$; $\mathsf{C}\mathbf{v}\cdot\mathbf{T} = \mathbf{v}\cdot\mathsf{I}\mathbf{T}$, for any vector $\mathbf{v}$ and second order tensor $\mathbf{T}$; $\mathsf{D}\mathbf{T}\cdot\mathbf{V} = \mathbf{T}\cdot\mathsf{O}\mathbf{V}$, for any second order tensor $\mathbf{T}$ and $\mathbf{V}$; $\mathsf{N}\mathbf{T}\cdot\mathbf{v} = \mathbf{T}\cdot\mathsf{Q}\mathbf{v}$, for any second order tensor $\mathbf{T}$ and vector $\mathbf{v}$. If the material microstructure is arranged respecting the central symmetry the odd order tensors B, C, N, and the corresponding transposed tensors defined by the above relations, are null. Moreover, the tensors B, C, F, M, N, as well as the corresponding transposed tensors, contain internal length parameters and then, even in this case of homogeneous deformations, the non-local character of the description is guaranteed.

The lattice system described in Sect. 2 can be then replaced by an equivalent multifield continuum with additional degrees of freedom endowed with a rigid local structure (Cosserat, e.g. [10]) plus a deformable (affine) structure, of the kind described in [5] or also in [14], encoded in the power formula (8). This continuum undergo microdeformations independent of the local macroscopic deformation and

a detailed description of the basics can be found in [31, 34]. This description can be contextualized within the more general frameworks delineated in [8, 11, 16, 27].

In the case in which $\mathbf{d} = \mathbf{0}$, using Eqs. (11) where no-interaction between particle and slits are accounted for ($\mathsf{C} = 0\,, \mathsf{I} = 0$ and $\mathsf{D} = 0\,, \mathsf{O} = 0$), the internal power density (8) can be written:

$$\pi = [\mathsf{A}(\nabla\mathbf{w} - \mathbf{W}) + \mathsf{B}\nabla\mathbf{W}] \cdot (\nabla\mathbf{w} - \mathbf{W}) + \frac{1}{2}\,[\mathsf{E}(\nabla\mathbf{w} - \mathbf{W}) + \mathsf{F}\nabla\mathbf{W}] \cdot \nabla\mathbf{W}\,, \quad (12)$$

that is the power density formula of a micropolar continuum equivalent to an assembly of rigid particles, without slits, undergoing independent rotations one each other, $\mathbf{W}^a$, and interacting through forces and couples, $\mathbf{t}^a$, $\mathbf{C}^a$ ($\forall\, \mathscr{A}$ in $\mathscr{M}_\mu$).

In order to make comparisons with other continuous models, it is useful to distinguish in the expression (12) the contributions of the symmetric and the skew-symmetric part of the strain and stress tensors. By decomposing the displacement gradient $\nabla\mathbf{w} = \mathbf{E} + \mathbf{R}$, with $\mathbf{E} = \mathrm{sym}[\nabla\mathbf{w}]$ and $\mathbf{R} = \mathrm{skw}[\nabla\mathbf{w}]$, where the operators sym and skw, respectively, extract the symmetric and the skew-symmetric part of a tensor, it is:

$$\begin{aligned}\pi \;=\; & \mathrm{sym}[\mathsf{A}(\mathbf{E} + \mathbf{R} - \mathbf{W}) + \mathsf{B}\nabla\mathbf{W}] \cdot \mathbf{E} + \mathrm{skw}[\mathsf{A}(\mathbf{E} + \mathbf{R} - \mathbf{W}) + \mathsf{B}\nabla\mathbf{W}] \cdot (\mathbf{R} - \mathbf{W}) \\ & + \frac{1}{2}\,[\mathsf{E}(\mathbf{E} + \mathbf{R} - \mathbf{W}) + \mathsf{F}\nabla\mathbf{W}] \cdot \nabla\mathbf{W}\,. \end{aligned} \quad (13)$$

By putting:

$$\begin{aligned}\pi^{YY} &= \mathrm{sym}[\mathsf{A}\mathbf{E}] \cdot \mathbf{E} \\ \pi^{YK} &= \mathrm{sym}[\mathsf{A}(\mathbf{R} - \mathbf{W})] \cdot \mathbf{E} = \mathrm{skw}[\mathsf{A}\mathbf{E}] \cdot (\mathbf{R} - \mathbf{W}) = \pi^{KY} \\ \pi^{KK} &= \mathrm{skw}[\mathsf{A}(\mathbf{R} - \mathbf{W})] \cdot (\mathbf{R} - \mathbf{W}) \\ \pi^{YC} &= \mathrm{sym}[\mathsf{B}\nabla\mathbf{W}] \cdot \mathbf{E} = \frac{1}{2}\,\mathsf{E}\mathbf{E} \cdot \nabla\mathbf{W} = \pi^{CY} \\ \pi^{KC} &= \mathrm{skw}[\mathsf{B}\nabla\mathbf{W}] \cdot (\mathbf{R} - \mathbf{W}) = \frac{1}{2}\,\mathsf{E}(\mathbf{R} - \mathbf{W}) \cdot \nabla\mathbf{W} = \pi^{CK} \\ \pi^{CC} &= \frac{1}{2}\,\mathsf{F}\nabla\mathbf{W} \cdot \nabla\mathbf{W}\,. \end{aligned} \quad (14)$$

Equation (13) can be written:

$$\pi = \pi^{YY} + \pi^{KK} + \pi^{CC} + 2(\pi^{YK} + \pi^{YC} + \pi^{KC})\,. \quad (15)$$

It can be noticed that the term π^{YY} corresponds to the classical term. The terms π^{KK} and π^{CC} are characteristic to the Cosserat continuum. The mixed terms $\pi^{CY} = \pi^{YC}$ and $\pi^{CK} = \pi^{KC}$ are null in the case of materials belonging to the class of

centrosymmetric materials or more restricted symmetry classes, while the mixed term $\pi^{YK} = \pi^{KY}$ is null in the case of orthotetragonal materials or more restricted material symmetry classes.

3.2 Second Order Continuum Approximation

Let us now consider the case in which, in the maps (5), $\mathbf{d} = \mathbf{0}$ and $\mathbf{W} = \mathrm{skw}[\nabla\mathbf{w}] = \mathbf{R}$, with $\nabla^2\,\mathbf{w} \neq \mathbf{0}$. Referring to the original lattice system, these constraints connote a system without slits and with particles constrained to undergo the same local rigid rotation of the continuum ($\mathbf{W}^a = \mathbf{R}$, $\forall(\mathscr{A}) \in \mathscr{M}_\mu$), as in the Voigt model described in [31]. This implies that: $\nabla\mathbf{w} - \mathbf{W} = \mathbf{E}$ ($\mathbf{E} = \mathrm{sym}[\nabla\mathbf{w}]$) and, for negligible distances $\mathbf{p}^a - \mathbf{p}^b$, the strain measures of the lattice reduce to:

$$\mathbf{w}_i = \mathbf{E}(\mathbf{a}-\mathbf{b}) + \frac{1}{2}\nabla^2\mathbf{w}[(\mathbf{a}-\mathbf{x})\otimes(\mathbf{a}-\mathbf{x}) - (\mathbf{b}-\mathbf{x})\otimes(\mathbf{b}-\mathbf{x})]\,, \tag{16}$$

where the explicit dependence of any field on $\mathbf{x}$ is undertaken. Hence, the mean power of the contact actions over $\mathscr{M}_\mu$ (3) can be written as:

$$\begin{aligned}\bar{\Pi}_\mu = \tfrac{1}{V(\mathscr{M}_\mu)}\{&\sum_i \mathbf{t}_i \otimes (\mathbf{a}-\mathbf{b})\cdot\mathbf{E} \\ &+ \frac{1}{2}\sum_i \mathbf{t}_i \otimes [(\mathbf{a}-\mathbf{x})\otimes(\mathbf{a}-\mathbf{x}) - (\mathbf{b}-\mathbf{x})\otimes(\mathbf{b}-\mathbf{x})]\cdot\nabla^2\mathbf{w}\}\,.\end{aligned} \tag{17}$$

This formula corresponds to the mean power of the internal action of the module of a lattice system whose particles, as mentioned above, are locally constrained to have the same rotation and to (non-locally) interact through forces and moments of forces, but no couples. It can be shown in fact that, for $\mathbf{p}^a - \mathbf{p}^b$ approaching to zero, constitutive and balance considerations imply that the interaction couple $\mathbf{C}_i$ is null (as assumed by Voigt [36], p. 599).

Considering a continuous neighbourhood, $\mathscr{M} \equiv \mathscr{M}_\mu$, of a second-gradient continuum of the kind described in [23, 24], which has the fields $\mathbf{E}$ and $\nabla^2\mathbf{w}$ as primal strain fields, the equivalence between the mean internal power of the module (Eq. 17) and the internal power density formula of the continuum

$$\pi = \mathbf{T}\cdot\mathbf{E} + \mathsf{T}\cdot\nabla^2\mathbf{w}\,, \tag{18}$$

for any $\mathbf{E}$ and $\nabla^2\mathbf{w}$, through the localization theorem, gives the dual stress measures as functions of the contact actions and of the fabric quantities of the module:

$$\begin{aligned}\mathbf{T} &= \tfrac{1}{V(\mathscr{M}_\mu)} \sum_i \mathrm{sym}[\mathbf{t}_i \otimes (\mathbf{a}-\mathbf{b})] \\ \mathsf{T} &= \tfrac{1}{2V(\mathscr{M}_\mu)} \sum_i \mathbf{t}_i \otimes [(\mathbf{a}-\mathbf{x})\otimes(\mathbf{a}-\mathbf{x}) - (\mathbf{b}-\mathbf{x})\otimes(\mathbf{b}-\mathbf{x})]\,. \end{aligned} \tag{19}$$

Assuming that the interactions between the pairs of particles $(\mathscr{A}, \mathscr{B})$ are linear elastic forces: $\mathbf{t}_i = \mathbf{K}_i\mathbf{w}_i$, with $\mathbf{K}_i$ the second order stiffness tensor for the ith pair, and assuming that the discrete-continuum maps (5), under the mentioned kinematical constraints, also hold for the actual kinematical descriptors, the constitutive relationships of the equivalent second-gradient continuum can be obtained in the form:

$$\begin{aligned}\mathbf{T} &= \mathsf{A}\mathbf{E} + \mathsf{B}\nabla^2\mathbf{w} \\ \mathsf{T} &= \mathsf{E}\mathbf{E} + \mathsf{F}\nabla^2\mathbf{w}\,, \end{aligned} \tag{20}$$

where the elastic tensors of order four (A), five (B, E) and six (F) have components depending on the elastic constants of the matrix and on the geometry of the inclusions. For these tensors the same symbols as those used for the first order continuum are used in order to underline the similarities in the identification process, although their components in general differ. Their explicit expressions are reported in [32]. In the case of hyperelastic materials the transposition relation holds: $\mathsf{B}\mathbf{A}\cdot\mathbf{B} = \mathbf{A}\cdot\mathsf{E}\mathbf{B}$, for any pair of second order tensors $\mathbf{A}$ and $\mathbf{B}$. In the case of central symmetry the odd order tensors B and E are null. These tensors and the tensor F contain material internal lengths.

Then, the power density of the internal actions of the equivalent second gradient continuum can be written:

$$\pi = [\mathsf{A}\mathbf{E} + \mathsf{B}\nabla^2\mathbf{w}]\cdot\mathbf{E} + [\mathsf{E}\mathbf{E} + \mathsf{F}\nabla^2\mathbf{w}]\cdot\nabla^2\mathbf{w}\,. \tag{21}$$

It is useful to separate the different terms:

$$\begin{aligned}\pi^{YY} &= \mathsf{A}\mathbf{E}\cdot\mathbf{E} \\ \pi^{\nabla\nabla} &= \mathsf{F}\nabla^2\mathbf{w}\cdot\nabla^2\mathbf{w} \\ \pi^{\nabla Y} &= \mathsf{B}\nabla^2\mathbf{w}\cdot\mathbf{E} = \mathsf{E}\mathbf{E}\cdot\nabla^2\mathbf{w} = \pi^{Y\nabla}\,, \end{aligned} \tag{22}$$

in such a way that:

$$\pi = \pi^{YY} + \pi^{\nabla\nabla} + 2\pi^{Y\nabla}\,. \tag{23}$$

The term π^{YY} corresponds to the classical term. The term $\pi^{\nabla\nabla}$ is characteristic to the second gradient continuum. The mixed term $\pi^{Y\nabla}$ is null in the case of centrosymmetric materials.

3.3 Classical Continum Approximation

Under both the constraints $\mathbf{d} = \mathbf{0}$ and $\mathbf{W} = \mathbf{R}$, assuming homogeneous discrete-continuum maps, that is, Eqs. (5) with $\nabla^2 \mathbf{w} = \mathbf{0}$, it is:

$$\mathbf{w}_i = \mathbf{E}(\mathbf{a} - \mathbf{b}) \,. \tag{24}$$

and the mean internal power (Eq. (17)) reads:

$$\bar{\Pi}_\mu = \tfrac{1}{V(\mathscr{M}_\mu)} \sum_i \mathbf{t}_i \otimes (\mathbf{a} - \mathbf{b}) \cdot \mathbf{E} \,. \tag{25}$$

The kinematic map (24) corresponds to the so-called Cauchy–Born rule used in crystal elasticity.

Superimposing the continuous neighbourhood of $\mathbf{x}$, $\mathscr{M}$, to the module, $\mathscr{M}_\mu$, the tensor $\mathbf{E}$ can be interpreted as the smooth field representing the symmetric strain measure of a Cauchy continuum. By requiring the equivalence between $\bar{\Pi}_\mu$ and the internal power density of the classical continuum

$$\pi = \mathbf{T} \cdot \mathbf{E} \,, \tag{26}$$

for any $\mathbf{E}$, always basing on the localization theorem, the classical dual stress tensor $\mathbf{T}$ is identified as:

$$\mathbf{T} = \tfrac{1}{V(\mathscr{M}_\mu)} \operatorname{sym}[\mathbf{t}_i \otimes (\mathbf{a} - \mathbf{b})] \,. \tag{27}$$

Assuming the linear elastic response functions for the contact actions as in Sect. 3.2 and assuming that the discrete-continuum maps (5), under the given kinematical constraints, also hold for the actual kinematical descriptors, the constitutive relationships of the equivalent classical continuum can be expressed in the form:

$$\mathbf{T} = \mathsf{A}\mathbf{E} \,, \tag{28}$$

where A is the fourth order classical elastic tensor, which does not contain any material length, and:

$$\pi = \pi^{YY} \,. \tag{29}$$

The Cauchy model is equivalent in terms of power to a discrete system of rigid particles locally constrained to have the same rotation which locally interact through forces.

4 Structure of External Power and Balance Equations for Bulk and Contact Actions of the Equivalent Non-Classical Continua

The structure of a non-local, scale-dependent, non-classical continuum is encoded in its internal power formula. In Sect. 3 it has been shown that the power equivalence between complex lattice systems and non-classical continua with additional degrees of freedom, together with the selection of response functions for the discrete model, leads to the identification of the constitutive functions for all the, standard and non-standard, internal actions. This is a key critical point for such kind of continua.

Other critical points are the derivation of the whole set of balance equations and the identification of the external actions [5, 6, 15]. In this Section it is shown how starting from the power density formula of continua as those identified in Sect. 3, using the divergence theorem and applying the virtual power principle the structure of the corresponding external power can be defined, as well as the kinds of bulk and contact actions (macro and micro tractions). Moreover, in agreement with the axiomatic framework delineated in [9, 13], the local balance equations for the standard and non-standard actions are derived.

4.1 Continuum with Rigid and Affine Microstructure

Let us now consider the internal power of the continuum identified in Sect. 3.1 over a control region $\mathscr{P} \subseteq \mathscr{C}$, $\mathscr{C}$ being the Euclidean region occupied by a body, with smooth boundary $\partial\mathscr{P}$ and outward normal $\mathbf{n}$:

$$\Pi = \int_{\mathscr{P}} [\mathbf{S} \cdot (\nabla \mathbf{w} - \mathbf{W}) + \frac{1}{2}\mathsf{S} \cdot \nabla \mathbf{W} + \mathbf{z} \cdot \mathbf{d} + \mathbf{Z} \cdot \nabla \mathbf{d}]\, dV\,. \tag{30}$$

The divergence theorem gives:

$$\begin{aligned} \Pi = & \int_{\mathscr{P}} [\text{div}\ \mathbf{S} \cdot \mathbf{w} + (\frac{1}{2}\text{div}\ \mathsf{S} + \ \text{skw}\, \mathbf{S}) \cdot \mathbf{W} + (\text{div}\ \mathbf{Z} - \mathbf{z}) \cdot \mathbf{d}]\, dV \\ & + \int_{\partial\mathscr{P}} (\mathbf{S}\,\mathbf{n} \cdot \mathbf{w} + \frac{1}{2}\,\mathsf{S}\,\mathbf{n} \cdot \mathbf{W} + \mathbf{Z}\,\mathbf{n} \cdot \mathbf{d})\, dA\,. \end{aligned} \tag{31}$$

Then the power equivalence between the internal and external power required for any $\mathbf{w}$, $\mathbf{W}$, and $\mathbf{d}$, provides the structure of the external power as:

$$\Pi^e = \int_{\mathscr{P}} \mathbf{b} \cdot \mathbf{w}\, dV + \int_{\partial\mathscr{P}} (\mathbf{t} \cdot \mathbf{w} + \frac{1}{2}\,\mathbf{C} \cdot \mathbf{W} + \mathbf{p} \cdot \mathbf{d})\, dA\,, \tag{32}$$

for any $\mathscr{P} \subseteq \mathscr{C}$, where, for the sake of simplicity, neither volume terms dual to $\mathbf{W}$ nor volume terms dual to $\mathbf{d}$ (external volume microforces) are considered. By

localization, the balance equations for the bulk:

$$\begin{aligned} &\operatorname{div}\mathbf{S}+\mathbf{b}=\mathbf{0}\,,\\ &\operatorname{div}\mathsf{S}+2\operatorname{skw}\mathbf{S}=\mathbf{0}\,, \qquad\qquad \text{in } \mathscr{P}\\ &\operatorname{div}\mathbf{Z}-\mathbf{z}=\mathbf{0}\,, \end{aligned} \tag{33}$$

and the contact actions (macrotractions, surface microcouples, microtractions):

$$\mathbf{S}\mathbf{n}=\mathbf{t}\,, \qquad \mathsf{S}\mathbf{n}=\mathbf{C}\,, \qquad \mathbf{Z}\mathbf{n}=\mathbf{p}\,, \qquad \text{on } \partial\mathscr{P} \tag{34}$$

are then derived. In Eqs. (33) and (34): $\mathbf{b}$ is the vector of the external volume forces; $\mathbf{t}$ and $\mathbf{C} \in \mathrm{Skw}$ are the vector and tensor (Skw being the set of second order skew-symmetric tensors) of surface forces and couples on ∂P, respectively; $\mathbf{p}$ is the vector of surface microforces exerted through $\partial\mathscr{P}$.

Equation (33a) expresses the classical linear momentum balance, (33b) the angular momentum balance and (33c) the micro linear momentum balance. It is worth noting that this last balance equation, obtained via the virtual power equivalence, is not obtainable via the standard invariance under Galilean changes of observers [15]. In Eqs. (33) and (34), $\mathbf{S}$ represents the second order macrostress tensor, S the third order couple-stress tensor, while $\mathbf{z}$ and $\mathbf{Z}$ are respectively the vector of the internal volume microstructural actions and the second order microstress tensor. These last terms account for the additional state of stress on the body due to the presence of defects and to their interactions. In particular, the internal force $\mathbf{z}$ can be interpreted as an auto-force accounting for the internal changes of the material configurations due to the presence of defects, while it can be shown that the stress tensor $\mathbf{Z}$, due to the relative deformation between defects, is related to the so-called configurational, or material, tensor [14, 21].

It can be shown that the microstrain measures $\mathbf{d}$ and $\nabla\mathbf{d}$ are non-null under a rigid micromotion. According to the axiomatic description in [9], it must be then required that the internal power under rigid macro and micro motions:

$$\Pi^* = \int_{\mathscr{P}} [\mathbf{S}\cdot(\nabla\mathbf{w}-\mathbf{W})^* + \frac{1}{2}\,\mathsf{S}\cdot\nabla\mathbf{W}^* + \mathbf{z}\cdot\mathbf{d}^* + \mathbf{Z}\cdot\nabla\mathbf{d}^*]\,dV \tag{35}$$

is null for any strain field defined as in [31]: $(\nabla\mathbf{w}-\mathbf{W})^* = \mathbf{0}$, $\nabla\mathbf{W}^* = \mathbf{0}$, $\mathbf{d}^* = \mathbf{R}\mathbf{d}$, $\nabla\mathbf{d}^* = \mathbf{R}\nabla\mathbf{d}$, where the symbol "$*$" stands for the attribute "rigid". Then applying the divergence theorem it is:

$$\begin{aligned} \Pi^* &= \int_{\mathscr{P}} (\mathbf{z}\cdot\mathbf{R}\mathbf{d}\cdot + \mathbf{Z}\cdot\mathbf{R}\nabla\mathbf{d})\,dV\\ &= -\int_{\mathscr{P}} \mathbf{R}\mathbf{z}\cdot\mathbf{d}\,dV + \int_{\mathscr{P}} \operatorname{div}(\mathbf{R}\,\mathbf{Z})\cdot\mathbf{d}\,dV - \int_{\mathscr{P}} \mathbf{R}\,\mathbf{Z}\,\mathbf{n}\cdot\mathbf{d}\,dV\\ &= \int_{\mathscr{P}} \mathbf{R}\cdot(\operatorname{div}\mathbf{Z}-\mathbf{z})\otimes\mathbf{d}\,dV + \int_{\partial P} \mathbf{R}\cdot\mathbf{Z}\mathbf{n}\otimes\mathbf{d}\,dA = 0\,, \end{aligned} \tag{36}$$

and, accounting for the microforce balance, Eq. (33c), it is:

$$\text{skw}(\mathbf{Z}\,\mathbf{n}\otimes\mathbf{d})=\mathbf{0}\,,\qquad\text{on }\partial\mathscr{P}\,. \tag{37}$$

Equation (37) is a micromoment balance equation, playing the role of a constitutive prescription [9], which implies that the microtraction $\mathbf{p}$ is parallel to $\mathbf{d}$.

If only the rigid microstructure is present ($\mathbf{d}=\mathbf{0}$), the internal power is zero for any rigid velocity field, and no equation must be added to Eqs. (33). In this case the bulk balance equations obtained using the principle of virtual power correspond to those of a micropolar continuum (33a, b), with the surface balance (34a, b).

4.2 Second Gradient Continuum

The internal power of a second-gradient continuum (Sect. 3.2) writes:

$$\Pi=\int_{\mathscr{P}}\mathbf{T}\cdot\nabla\mathbf{w}\,dV+\int_{\mathscr{P}}\mathsf{T}\cdot\nabla^2\mathbf{w}\,dV\,, \tag{38}$$

where $\mathscr{P}\subseteq\mathscr{C}$ is the control volume with boundary ∂P and outward normal $\mathbf{n}$, $\mathscr{C}$ being the Euclidean region occupied by a body.

Applying the divergence theorem to the term related to the microtraction T it is:

$$\int_{\mathscr{P}}\mathsf{T}\cdot\nabla^2\mathbf{w}\,dV=-\int_{\mathscr{P}}\text{div}\mathsf{T}\cdot\nabla\mathbf{w}\,dV+\int_{\partial\mathscr{P}}\mathsf{T}\mathbf{n}\cdot\nabla\mathbf{w}\,dA\,, \tag{39}$$

and, by putting $\tilde{\mathbf{T}}=\mathbf{T}-\text{div}\mathsf{T}$, Eq. (38) can be rewritten as follows:

$$\Pi=\int_{\mathscr{P}}\tilde{\mathbf{T}}\cdot\nabla\mathbf{w}\,dV+\int_{\partial\mathscr{P}}\mathsf{T}\mathbf{n}\cdot\nabla\mathbf{w}\,dA. \tag{40}$$

Then, applying the divergence theorem to the first term of Eq. (40), it is:

$$\int_{\mathscr{P}}\tilde{\mathbf{T}}\cdot\nabla\mathbf{w}\,dV=-\int_{\mathscr{P}}\text{div}\tilde{\mathbf{T}}\cdot\mathbf{w}\,dV+\int_{\partial\mathscr{P}}\tilde{\mathbf{T}}\mathbf{n}\cdot\mathbf{w}\,dA. \tag{41}$$

By decomposing $\nabla\mathbf{w}$ as: $\nabla\mathbf{w}=\nabla_s\mathbf{w}+\partial_n\mathbf{w}\otimes\mathbf{n}$, with $\nabla_s\mathbf{w}=\nabla\mathbf{w}\,(\mathbf{I}-\mathbf{n}\otimes\mathbf{n})$ and $\partial_n\mathbf{w}=\nabla\mathbf{w}\,\mathbf{n}$, $\mathbf{I}$ being the identity tensor, the expression of the internal power (40) becomes:

$$\Pi=-\int_{\mathscr{P}}\text{div}\tilde{\mathbf{T}}\cdot\mathbf{w}\,dV+\int_{\partial\mathscr{P}}\tilde{\mathbf{T}}\mathbf{n}\cdot\mathbf{w}\,dA+\int_{\partial\mathscr{P}}\mathsf{T}\mathbf{n}\cdot\nabla_s\mathbf{w}\,dA+\int_{\partial\mathscr{P}}(\mathsf{T}\mathbf{n})\,\mathbf{n}\cdot\partial_{\mathbf{n}}\mathbf{w}\,dA\,. \tag{42}$$

The theorem of divergence can also be applied to the term of Eq. (42) related to the surface velocity gradient in several ways [12, 23, 28]. One way consists in exploiting the surface divergence theorem [12]:

$$\int_{\partial\mathscr{P}} \mathsf{T}\mathbf{n}\cdot\nabla_s\mathbf{w}\,dA = -\int_{\partial\mathscr{P}} [\mathrm{div}_s(\mathsf{T}\mathbf{n}) + 2k(\mathsf{T}\mathbf{n})\mathbf{n}]\cdot\mathbf{w}\,dA\,, \tag{43}$$

and then:

$$\begin{aligned}\Pi = &-\int_{\partial\mathscr{P}} \mathrm{div}\tilde{\mathbf{T}}\cdot\mathbf{w} + \int_{\partial\mathscr{P}} [\tilde{\mathbf{T}}\mathbf{n} - \mathrm{div}_s(\mathsf{T}\mathbf{n}) - 2k(\mathsf{T}\mathbf{n})\mathbf{n}]\cdot\mathbf{w}\,dA \\ &+\int_{\partial\mathscr{P}} (\mathsf{T}\mathbf{n})\mathbf{n}\cdot\partial_{\mathbf{n}}\mathbf{w}\,dA\,,\end{aligned} \tag{44}$$

where $k = -\frac{1}{2}\mathrm{tr}\nabla_s\mathbf{n}$ is the mean curvature of $\partial\mathscr{P}$. In this case the power equivalence between internal and external power required for any $\mathbf{w}$, $\mathbf{W}$ and $\mathbf{d}$, and any $\mathscr{P}\subseteq\mathscr{C}$, provides the structure of the external power as:

$$\Pi^e = \int_{\mathscr{P}} \mathbf{b}\cdot\mathbf{w}\,dV + \int_{\partial\mathscr{P}} (\mathbf{f}\cdot\mathbf{w} + \mathbf{h}\cdot\partial_{\mathbf{n}}\mathbf{w})\;dA\,, \tag{45}$$

where $\mathbf{b}$ is the body force, $\mathbf{f}$ and $\mathbf{h}$ are the diffused traction and microtractions on $\partial\mathscr{P}$, respectively. By localization the balance equations for the bulk and contact actions become:

$$\mathrm{div}\tilde{\mathbf{T}} + \mathbf{b} = \mathbf{0} \quad \text{in} \quad \mathscr{P}\,, \tag{46}$$

with:

$$\begin{aligned}\tilde{\mathbf{T}}\,\mathbf{n} - \mathrm{div}_s\mathsf{T}\mathbf{n} - 2k(\mathsf{T}\mathbf{n})\mathbf{n} &= \mathbf{f}\,,\\ (\mathsf{T}\mathbf{n})\mathbf{n} &= \mathbf{h} \quad \text{on} \quad \partial\mathscr{P}\,.\end{aligned} \tag{47}$$

Another way of applying the divergence theorem [28] accounts for the presence of contact actions distributed along lines $\partial(\partial\mathscr{P})$ in such a way that:

$$\int_{\partial\mathscr{P}} \mathsf{T}\mathbf{n}\cdot\nabla_s\mathbf{w}\,dA = -\int_{\partial\mathscr{P}} \mathrm{div}_s(\mathsf{T}\mathbf{n})\cdot\mathbf{w}\,dA + \int_{\partial(\partial\mathscr{P})} (\mathsf{T}\mathbf{n})\,\mathbf{m}\cdot\mathbf{w}\,dl\,, \tag{48}$$

where $\mathbf{m}$ is a unit vector, orthogonal to both $\mathbf{n}$ and to the tangent direction of $\partial(\partial P)$, pointing outward from the interior of ∂P. Considering and edge $\widehat{\partial\mathscr{P}}$ with outwards normals $\mathbf{n}$ and $\mathbf{m}$ are not univocally defined it is assumed that:

$$\int_{\partial(\partial\mathscr{P})} (\mathsf{T}\mathbf{n})\,\mathbf{m}\cdot\mathbf{w}\,dl = \int_{\widehat{\partial\mathscr{P}}} <(\mathsf{T}\mathbf{n})\,\mathbf{m}>\cdot\mathbf{w}\,dl\,, \tag{49}$$

where $< (\mathsf{T}\mathbf{n})\,\mathbf{m} >$ denotes the edge average of $(\mathsf{T}\,\mathbf{n})\mathbf{m}$ over the tangent and the normal vectors of the two surfaces connecting at $\widehat{\partial\mathscr{P}}$. Then the internal power can be rewritten as:

$$\Pi = -\int_{\mathscr{P}} \mathrm{div}\tilde{\mathbf{T}} \cdot \mathbf{w}\, dV + \int_{\partial\mathscr{P}} \left[\tilde{\mathbf{T}}\mathbf{n} - \mathrm{div}_s(\mathsf{T}\mathbf{n})\right] \cdot \mathbf{w}\, dA$$
$$+ \int_{\partial\mathscr{P}} (\mathsf{T}\mathbf{n})\mathbf{n} \cdot \partial_{\mathbf{n}}\mathbf{w}\, dA + \int_{\widehat{\partial\mathscr{P}}} < (\mathsf{T}\mathbf{n})\mathbf{m} > \, dl \tag{50}$$

Applying the virtual power principle the external power can be written as:

$$\Pi^{ext} = \int_{\mathscr{P}} \mathbf{b} \cdot \mathbf{w}\, dV + \int_{\partial\mathscr{P}} (\mathbf{f} \cdot \mathbf{w} + \mathbf{h} \cdot \partial_{\mathbf{n}}\mathbf{w})\, dA + \int_{\widehat{\partial\mathscr{P}}} \mathbf{h}_l \cdot \mathbf{w}\, dl\,. \tag{51}$$

where $\mathbf{b}$ is the body force, $\mathbf{f}$ and $\mathbf{h}$ are the diffused traction and microtraction on $\partial\mathscr{P}$, respectively, and $\mathbf{h}_l$ is the traction concentrated at the edge $\widehat{\partial\mathscr{P}}$. By localizing, the local balance equations derived are:

$$\mathrm{div}\tilde{\mathbf{T}} + \mathbf{b} = \mathbf{0} \quad \text{in} \quad \mathscr{P}\,, \tag{52}$$

with:

$$\begin{aligned} \tilde{\mathbf{T}}\mathbf{n} - \mathrm{div}_s(\mathsf{T}\,\mathbf{n}) &= \mathbf{f}\,, \\ (\mathsf{T}\mathbf{n})\mathbf{n} &= \mathbf{h} \quad \text{on} \quad \partial\mathscr{P}\,, \\ < (\mathsf{T}\mathbf{n})\,\mathbf{m} > &= \mathbf{h}_l \quad \text{on} \quad \widehat{\partial\mathscr{P}}\,. \end{aligned} \tag{53}$$

In the case of the internal power of the continuum of Sect. 3.3, the virtual power principle gives the balance equations of the Cauchy continuum:

$$\mathrm{div}\,\mathbf{T} + \mathbf{b} = \mathbf{0} \quad \text{in} \quad \mathscr{P}\,. \tag{54}$$

$$\mathbf{T}\mathbf{n} = \mathbf{f} \quad \text{on} \quad \partial\mathscr{P}. \tag{55}$$

5 Numerical Simulations

In this paragraph some results of numerical simulations, obtained using COMSOL Multiphysics© finite element code, are mentioned for highlighting the potentiality of the non-classical continua described in Sects. 3 and 4.

5.1 Porous Fibre Reinforced Composites

The main features of the non-classical continua described above, here also called multifield continua because of the presence of additional degrees of freedom, are the presence of internal lengths in the material description and spatial dispersion in wave propagation. For these reasons such continua can be classified as "implicitly" non-local models [10, 18].

In the continuum with rigid and affine microstructure of Sects. 3.1 and 4.1 dispersion properties are related to the presence of the microvelocity term **d** in the equations of motion, that is not a derivative nor in space neither in time. In the works [31, 34] a one-dimensional problem, a bar with continuous distribution of microcracks, has been analysed under the effect of free and forced oscillations. In both cases, the variation of the phase velocity of propagating waves with the frequency, or the wave number, showed that the additional descriptor **d** reveals the presence of the microcrack as a disturbance spread along the bar which alters the shape and the velocity of the waves, and the that the kind of this disturbance strongly depends on the microcrack density per unit lengths.

Here the results of a two dimensional panel made of an orthotetragonal porous ceramic material in tension has been reported in order to show another peculiarity of the multifield continuum of Sects. 3.1 and 4.1 that is the reduction in stiffness obtained as an effect of the additional stress/strain state introduced in the multifield model.

The panel, of length $L = 100\,\mu$m, is simply supported and has different levels of porosity, evaluated with a pore density factor p (pores area/panel area). In the multifield model this factor enters into the constitutive tensors M and R of Eqs. (11) (Fig. 1). It is made of Al_2O_3 hexagonal grains, of side $22.5\,\mu$m, and Co interfaces, of thickness 1–2 μm, with Youngs' modulus and Poisson's coefficients: $E_g = 410{,}000$ MPa, $\nu_g = 0.25$ and $E_i = 210{,}000$ MPa, $\nu_i = 0.235$, respectively. The grains are not rigid and their deformability has be taken into account in terms of energy equivalent stiffness at the interfaces: $A_i E_i E_g/(E_i A_i + E_g A_g)$, A_g and A_i being the grain and interface areas, respectively. The multifield solution has been obtained and compared with a finite element solution for: $p = 0.039$ (1), $p = 0.11$ (2),

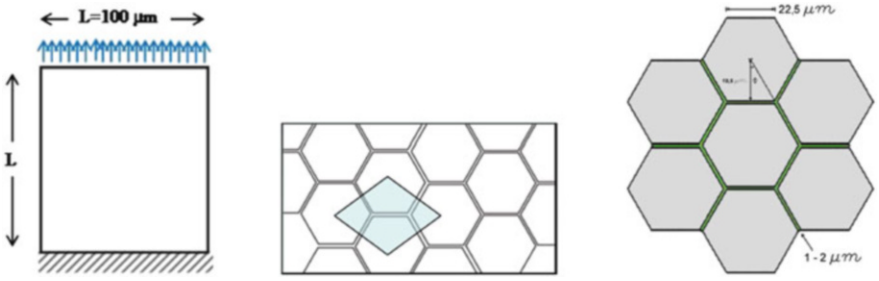

Fig. 1 Sketch of the ceramic panel

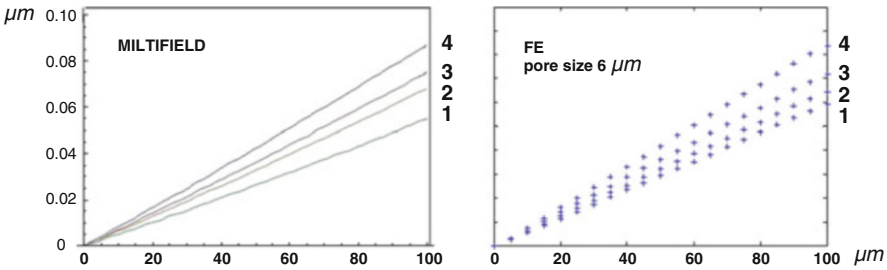

Fig. 2 Vertical component of displacement along the vertical direction of the panel for different pore density: (**1**) $p = 0.039$, (**2**) $p = 0.11$, (**3**) $p = 0.192$, (**4**) $p = 0.254$

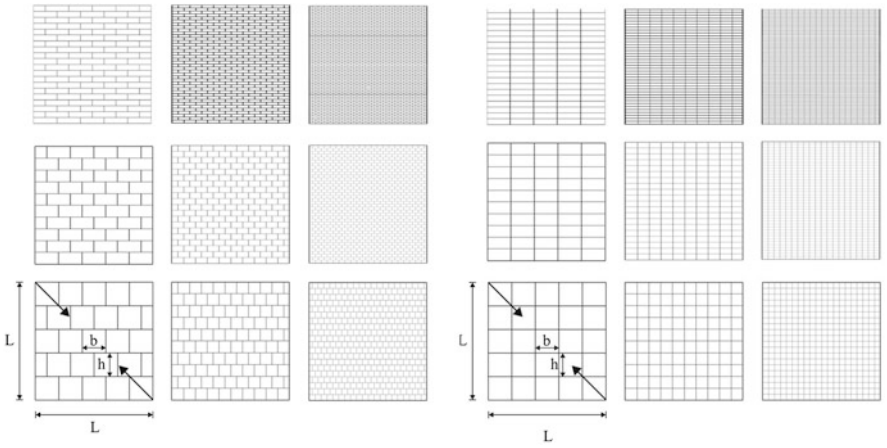

Fig. 3 Orthotropic block assemblies with different scale and aspect ratios. *Left*, systems with interlocking (from *top to bottom* and *left to right*: schemes a1–a9). *Right*, systems without interlocking (from *top to bottom* and *left to right*: schemes b1–b9)

$p = 0.192$ (3), $p = 0.254$ (1). The two solutions show that the vertical component of the displacement increases with the increase of the porosity (Fig. 2), confirming that in such a multifield model the presence of damage can be accounted for as an additional state of stress and strain rather than a reduction in stiffness, like in internal variables models with which these results have been compared [17].

5.2 Masonry-Like Materials

Here some results of a parametric study conducted for various schemes of orthotropic block assemblies is reported. A square panel of side L, made of blocks of length b and height h, simply supported and subjected to shear load has been analysed by varying the scale ($\epsilon_1 = b/L$, $\epsilon_2 = h/L$) and aspect ($\rho = h/b$) ratios (Fig. 3). The panel has been described as a discrete model made of rigid bodies

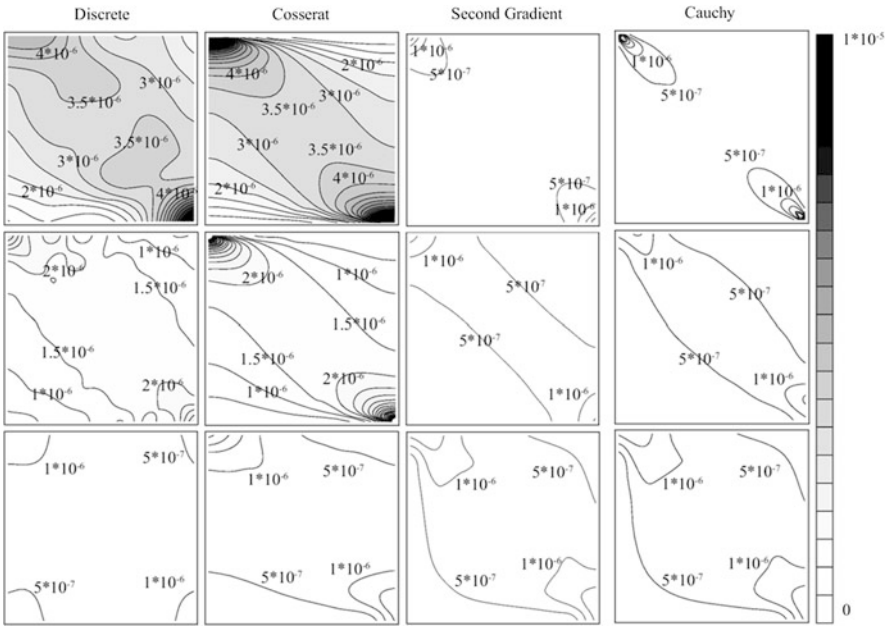

Fig. 4 Contour lines of the angular strain component in the discrete, Cosserat ($[\nabla \mathbf{w} - \mathbf{W}]_{12}$), second gradient and Cauchy ($[\mathbf{E}]_{12}$) model. Cases: $a1$, $a4$, $b7$ [32]

interacting by linear elastic springs and as a Cosserat, a second gradient and a Cauchy model, as identified in Sects. 3 and 4.

Figure 4 shows the contours lines of the angular component of the strain tensors, in the discrete, Cosserat, ($[\nabla \mathbf{w} - \mathbf{W}]_{12} = \nabla \mathbf{w} - \mathbf{W} \cdot \mathbf{e}_1 \otimes \mathbf{e}_2$), second gradient and Cauchy ($[\mathbf{E}]_{12} = \mathbf{E} \cdot \mathbf{e}_1 \otimes \mathbf{e}_2$), $\mathbf{e}_1$, $\mathbf{e}_2$ being the unit vectors defining the horizontal and vertical direction, respectively, obtained for the cases: $a1$ ($\epsilon_1 = 0.2$, $\epsilon_2 = 0.05$, $\rho = 0.25$); $a4$ ($\epsilon_1 = 0.2$, $\epsilon_2 = 0.1$, $\rho = 0.5$); $b7$ ($\epsilon_1 = 0.2$, $\epsilon_2 = 0.2$, $\rho = 1$). It can be noted that the Cosserat continuum solution is always in good agreement with the discrete solution. Differently, the second gradient and Cauchy continua fit well the response of the discrete model only in the orthotetragonal case (square blocks with no-interlocking: case $b7$).

The cases of Fig. 5: $a3$ ($\epsilon_1 = 0.025$, $\epsilon_2 = 0.0125$, $\rho = 0.25$); $a6$ ($\epsilon_1 = 0.025$, $\epsilon_2 = 0.025$, $\rho = 0.5$); $b9$ ($\epsilon_1 = 0.025$, $\epsilon_2 = 0.025$, $\rho = 1$) show that the same occurs at finer scales: the differences between the Cauchy/second gradient and discrete/Cosserat solutions are reduced, but still remain. The correspondence of all the solutions is obtained only in the orthotetragonal case.

The reason for which second gradient and Cauchy models fail in representing the behaviour of the discrete systems for orthotropic materials relies in the strong non-symmetries of the strain and stress tensors. In the discrete as in the Cosserat models in fact the power term π^{KK} due to relative rotation, which corresponds to the skew-symmetric part of the strain, plays an important role. Note that in the orthotetragonal

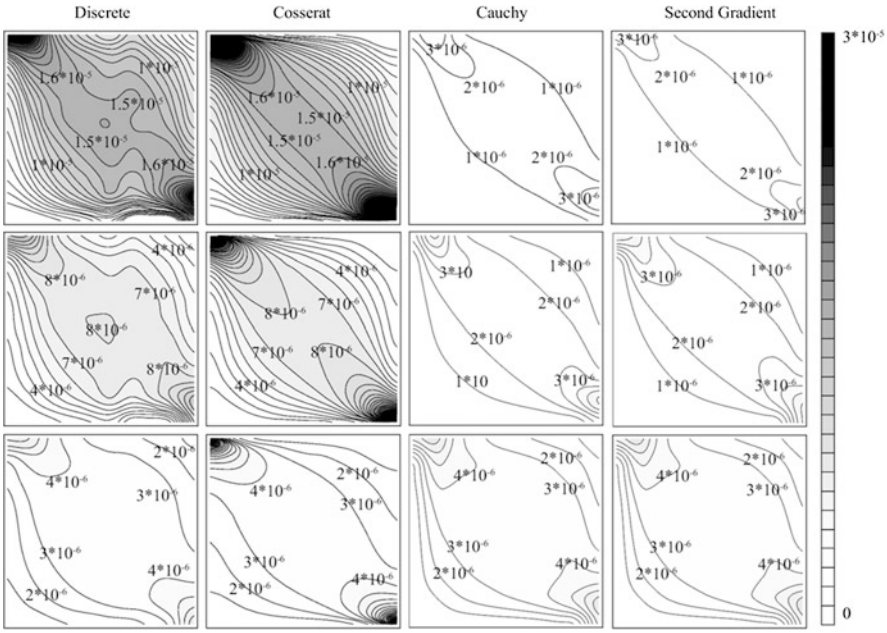

Fig. 5 Contour lines of the angular strain component in the discrete, Cosserat ($[\nabla \mathbf{w} - \mathbf{W}]_{12}$), second gradient and Cauchy ($[\mathbf{E}]_{12}$) model. Cases: *a*3, *a*6, *b*9 [32]

case it is always $\pi^{YK} = \pi^{KY} = 0$ (see Eqs. (14)). In the second gradient and Cauchy continua instead the strain, as well as the stress, is symmetric and the relative rotation term is not present (Eqs. (22)). This can be also confirmed by the results of Fig. 6 showing the contour lines of the sole non-null component of the relative rotation in the Cosserat model ($[\mathbf{R} - \mathbf{W}]_{12} = (\mathbf{R} - \mathbf{W}) \cdot \mathbf{e}_1 \otimes \mathbf{e}_2 = -[\mathbf{R} - \mathbf{W}]_{12} = (\mathbf{R} - \mathbf{W}) \cdot \mathbf{e}_2 \otimes \mathbf{e}_1$). Here the cases shown are: *a*1 ($\epsilon_1 = 0.2, \epsilon_2 = 0.05, \rho = 0.25$); *a*7 ($\epsilon_1 = 0.2, \epsilon_2 = 0.2, \rho = 1$); *b*7 ($\epsilon_1 = 0.2, \epsilon_2 = 0.2, \rho = 1$); *a*3 ($\epsilon_1 = 0.025, \epsilon_2 = 0.0125, \rho = 0.25$); *a*9 ($\epsilon_1 = 0.025, \epsilon_2 = 0.025, \rho = 1$); *b*9 ($\epsilon_1 = 0.025, \epsilon_2 = 0.025, \rho = 1$). This component reduces with the loss of interlocking becoming null in the orthotetragonal case (*b*7, *b*9).

Overall, this parametric study shows that the Cosserat continuum works well both in case of particles of significant size and when it is necessary to account for strong non-symmetries in strain and stress, like in orthotetragonal assemblies. The second gradient continuum, differently from the classical continuum, can represent the scale effects but, as the Cauchy continuum, lacks of the descriptor for the relative rotation (i.e. strain non-symmetry) that can be predominant in orthotropic assemblies.

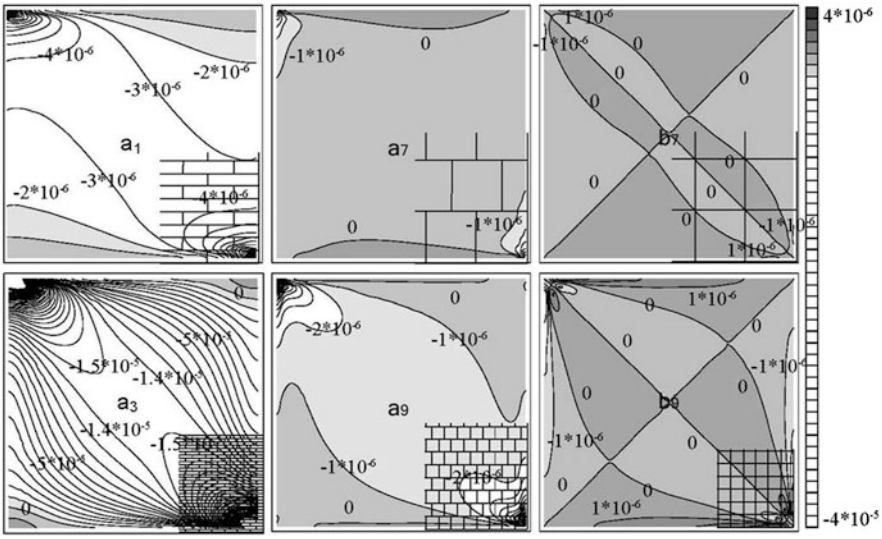

Fig. 6 Contour lines of the relative rotation in the Cosserat model. Cases: $a1$, $a7$, $b7$, $a3$, $a9$, $b9$ (courtesy of A. Pau)

6 Final Remarks

The discrete modelling of materials, crucial in the past for building constitutive theories for solids, can still be of help in determining physically plausible constitutive models for complex materials. The most significant suggestion, in a sense derived by Voigt and Poincaré, is the idea to build-up a refined non-local intermolecular potential based on appropriate, physically based, complex discrete systems to define case by case. Where refined here means to extend the concept of "molecule" for representing the various internal phases and to use generalized correspondence maps between discrete and continuum descriptors.

Scale-dependent continuous macro models have been unambiguously identified from complex discrete micro-models using the power equivalence procedure described in Sect. 3 using generalized correspondence laws between the large set of degrees of freedom of the discrete and the continuum field descriptors. In this way the macroscopic stress measures have been identified in terms of the constitutive constants and the geometry of the micro-model. In order to provide physical consistency to multifield continua, the constitutive relations have been finally derived assuming physically-based response functions for the lattice interactions.

These continua retains memory of the fine organization of the material by means of additional field descriptors and satisfy the basic requirements for the mechanical modelling of complex materials, that is: the presence of internal lengths and spatial dispersion in wave propagation, which in turn define the non-local character of the material description.

Acknowledgement This research has been partially supported by the Italian "Ministero dell'Università e della Ricerca Scientifica" (Research fund: MIUR Prin 2010-11(/12)).

References

1. Altenbach H, Eremeyev VA (eds) (2013) Generalized continua from the theory to engineering application. CISM Courses and Lectures, vol 541. Springer, Berlin
2. Capecchi D, Ruta G, Trovalusci P (2010) From classical to Voigt's molecular models in elasticity. Arch Hist Exact Sci 64:525–559
3. Capecchi D, Ruta G, Trovalusci P (2011) Voigt and Poincaré's mechanistic–energetic approaches to linear elasticity and suggestions for multiscale modelling. Arch Appl Mech 81(11):1573–1584
4. Capriz G (1985) Continua with latent microstructure. Arch Ration Mech Anal 90:43–56
5. Capriz G (1989) Continua with Microstructure. Springer, Berlin
6. Capriz G, Podio-Guidugli P (2004) Whence the boundary conditions in modern continuum physics. In: Atti dei Convegni Lincei, vol 210, Accademia Nazionale dei Lincei, Roma, pp 19–42
7. Cauchy A-L (1828) Sur l'équilibre et le mouvement d'un système de points matériels sollicités par des forces d'attraction ou de répulsion mutuelle. Exercices de Mathématiques 3:188–213, 1822, 1827. In. Œuvres 2(8):227–252
8. Cowin S, Nunziato JW (1983) Linear elastic materials with voids. J Elast 13:15–147
9. Di Carlo A (1996) A non-standard format for continuum mechanics. In: Batra RC, Beatty MF (eds) Contemporary research in the mechanics and mathematics of materials. International Center for Numerical Methods in Engineering, Barcelona, pp 92–104
10. Eringen AC (1999) Microcontinuum Field Theories. Springer, New York
11. Frémond M, Nedjar B (1996) Damage, gradient of damage and principle of virtual power. Int J Solids Struct 33(8):1083–1103
12. Fried E, Gurtin ME (2006) Tractions, balances and boundary conditions for non simple materials with application to liquid flow at small-length scales. Arch Ration Mech Anal 182:513–554
13. Germain P (1973) The method of virtual power in continuum mechanics. Part 2: Microstructure. SIAM J App Math 25(3):556–575
14. Gurtin ME (2000) Configurational Forces as Basis Concept of Continuum Physics. Springer, Berlin
15. Gurtin ME, Podio-Guidugli P (1992) On the formulation of mechanical balance laws for structured continua. Z Angew Math Phys 43:181–190
16. Gurtin ME, Podio-Guidugli P (1996) Configurational forces and the basic laws for crack propagation. J Mech Phys Solids 44:905–927
17. Kachanov M (1993) On the effective moduli of solids with cavities and cracks. Int J Fract 9:R17–R21
18. Kunin I (1982) Elastic Media with Microstructure-I. One-dimensional Models. Springer, Berlin (Russian edition 1975)
19. Mattoni A, Colombo L, Cleri F (2004) Atomistic study of the interaction between a microcrack and a hard inclusion. Phys Rev B 70(9):094108
20. Maugin GA (1979) Nonlocal theories or gradient–type theories: a matter of convenience? Arch Mech 31(1):15–26
21. Maugin GA (2011) Configurational Forces. Thermomechanics, Physics, Mathematics, and Numerics. CRC Series: Modern Mechanics and Mathematics. Chapman and Hall, Boca Raton
22. Mindlin RD (1964) Micro–structure in linear elasticity. Arch Rat Mech Anal 16:51–78
23. Mindlin RD (1965) Second gradient of strain and surface-tension in linear elasticity. Int J Solids Struct 1:417–438

24. Mindlin RD, Eshel NN (1968) On first strain-gradient theories in linear elasticity. Int J Solids Struct 4:109–124
25. Navier CLMH (1827) Mémoire sur le lois de l'équilibre et du mouvement des corps solides élastiques (1821). In: Mémoires de l'Academie des Sciences de l'Institut de France, II, vol 7, pp 375–393
26. Newton I (1730 (1717, 1704)) Opticks or a treatise of the reflections, refractions, inflections and colours of light. Queries, XXXI, 4th edn. W. Innis (Royal Society), London
27. Nunziato JW, Cowin S (1979) A nonlinear theory of elastic materials with voids. Arch Ration Mech Anal 72(2):175–201
28. Podio-Guidugli P, Vianello M (2010) Hypertractions and hyperstresses convey the same mechanical information. Contin Mech Thermodyn 22(3):163–176
29. Poincaré H (1892) Leçons sur la Théorie de l'Élasticité. Georges Carré, Paris
30. Poisson SD (1829) Mémoire sur l'équilibre et le mouvement des corps élastiques. In: Mémoires de l'Académie des Sciences de l'Institut de France, vol 8. Lu à l'Académien 1828, pp 357–405
31. Trovalusci P (2014) Molecular approaches for multifield continua: origins and current developments. In: Sadowsky T, Trovalusci P (eds) Multiscale Modeling of Complex Materials: Phenomenological, Theoretical and Computational Aspects. CISM Courses and Lectures, vol 556. Springer, Berlin, pp 211–278
32. Trovalusci P, Pau A (2014) Derivation of microstructured continua from lattice systems via principle of virtual works. The case of masonry-like materials as micropolar, second gradient and classical continua. Acta Mech 225(1):157–177
33. Trovalusci P, Capecchi D, Ruta G (2009) Genesis of the multiscale approach for materials with microstructure. Arch Appl Mech 79:981–997
34. Trovalusci P, Varano V, Rega G (2010) A generalized continuum formulation for composite materials and wave propagation in a microcracked bar. J Appl Mech 77(6):061002-1/061002-11
35. Voigt W (1887) Theoretische Studien über die Elasticitätsverhältnisse der Kristalle. In: Abhandlungen der Gesellschaft der Wissenschaften zu Göttingen, XXXIV
36. Voigt W (1910) Lehrbuch der Kristallphysik. B.G. Teubner, Leipzig